SISSA - SCUOLA
INTERNAZIONALE
SUPERIORE
STUDI AVANZATI
TRIESTE
Strada Costiera 11

ISAS - INTERNATIONAL SCHOOL FOR ADVANCED STUDIES

Thesis for the title of

"Doctor Philosophiae"

A MOLECULAR DYNAMICS STUDY OF THE DISPLACIVE SURFACE RECONSTRUCTION PHASE TRANSITIONS

Candidate

Wang Cai-zhuang

Supervisors

Prof. Erio Tosatti

Prof. Michele Parrinello

November 1986

TRIESTE

A Molecular Dynamics Study of The Displacive Surface Reconstruction Phase Transitions

Wang Cai-zhuang

International School for Advanced Studies (SISSA)

Trieste, Italy

This thesis is submitted for the degree of "Doctor Philosophiae" of the International School for Advanced Studies in Trieste, Italy.

Novenber 1986

Summary

The surface reconstruction phase transitions of the W(001) and Mo(001) surfaces have attracted wide interest due to their two-dimensional and displacive nature. Although a variety of studies /1-57/ has been carried out concerning these phenomena, the detailed lattice distortion and the nature as well as the mechanism of these phase transitions are still far from completely understood. The motivation of this thesis is to give a detailed quantitative description of the temperature-dependence of the reconstruction phase transition both in static and in dynamical aspects, and hence to clarify the nature of these surface phase transitions through a numerical statistical mechanics study.

Based on the effective lattice hamiltonian developed previously by Fasolino, Santoro and Tosatti /39/, we have treated the surface reconstruction as an effective lattice phenomenon and carried out an extensive slab molecular dynamics simulation for the clean W(001) and Mo(001) surfaces. The optimized effective interatomic potentials for the bulk and surface atoms of W (and Mo) have been constructed, by fitting them to many known experimental properties of the bulk and surface of W and Mo. The detailed MD results on the W(001) surface show that the transition from the low-temperature reconstructed c(2x2) phase to the high

temperature disordered phase is driven by phase fluctuations and occurs through a sequence of narrow but well-defined intermediate phases. The nature of these intermediate phases, so far undetected experimentally, is studied in detail and found to be incommensurate (floating). The developement of domains and the persistance of short-range order are also observed near the transition temperature. In the meanwhile, the temperature- dependence of the surface phonons of the reconstructed W(001) surface, shows however that the driving 'soft mode' does not go all the way to zero at the transition temperature. Instead a dramatic broadening occurs in its spectrum as the transition is approached, suggesting a displacive- order-disorder crossover at about T=0.5Tc. Hence the critical region is strongly characterized by order-disorder behaviour.

For the Mo(001) surface, MD results show that the incommensurate phase consists of antiphase M5 type domains (in-plane distortion) separated by the M1 domains (vertical distortion) by very sharp domain boundaries, a picture consistent with the soft phonon coupling mechanism proposed by Fasolino, Santoro and Tosatti /41/ and with the more general interacting components mechanism proposed by Heine and McConnel/102,103/.

This thesis basically consists of two parts. Part one

contains chapter 1 which gives a brief review of the present status of the experimental and theoretical studies of the W(001) and Mo(001) reconstructions. Part two is devoted to present our molecular dynamics studies of these phenomena and is arranged as follows. An introduction to the present work is given in chapter 2; then the molecular dynamics(MD) method is described in chapter 3; chapter 4 shows the procedure of how he potentials for the study of the W(001) surface reconstructon were determined and the detailed MD results on the W(001) surface reconstruction phase transitions are given in chapter 5. In chapter 6 some effects on the different choices of surface potential parameters and MD samples are discussed and in chapter 7 the temperature-dependence of the surface phonons of the reconstructed W(001) surface is given. Finally, the MD study of the incommensurate structure of the Mo(001) surface is presented in chapter 8.

Acknowledgement

I would like to express my gratitude to my supervisors professor E.Tosatti and professor M.Parrinello for their earnest and patient instructions and for their constant encouragement throughout the course of this study.

I am grateful to Dr. Annalisa Fasolino for her helpful discussions and collaborations, as well as for her kind help and critical reading of this manscript.

I also wish to express my appreciation for Anna Franchini for her generous help at the early stages of this work.

I thank Dr. A.Nobile and Dr. R.Innocente of the computer centre of SISSA and Dr. C.Breda and Dr. N.Russo of the computer centre of the University of Trieste for their instructions on computer programming and technical help. I also thank Dr. C.Bocchetta for his help in correcting part of the text.

All my gratitude also to professor P.Budinich and Professor L.Fonda for the fellowship grant and for their hospitality at SISSA.

Contents

Summary i

Acknowledgement iv

Part One

Chapter 1. Reconstruction of the clean W(001) and Mo(001) surfaces - a review

1.1 Introduction 1

1.2 The atomic structure 4

A. W(001) surface at low temperature

B. W(001) surface at high temperature

C. Mo(001) surface

1.3 The electronic structure 12

1.4 Driving force for the surface reconstruction 18

1.5 Lattice distortion versus frozen-in surface phonon 21

1.6 Landau description of the W(001) and Mo(001) surface phase transition 23

1.7 Effective lattice hamiltonian description of W(001) and Mo(001) surface reconstruction 30

Part Two

Chapter 2. Introduction to Part two 35

Chapter 3 Molecular Dynamics 38

3.1 Introduction 38

3.2 Conventional molecular dynamics 39

3.3 Extended molecular dynamics 42

A. MD simulation at constant pressure

Andersen Parrinello Rahman method

B. MD simulation at constant temperature

3.4 The algorithm 48

3.5 Periodic boundary condition 50

Chapter 4 Choice of potentials for W 53

4.1 Introduction 53

4.2 The bulk potential 54

4.3 The surface potential 65

Chapter 5 MD results of W(001) surface reconstruction phase transition 68

5.1 Introduction 68

5.2 MD simulation procedure 69

5.3 Temperature behaviour of the order parameters 70

5.4 Floating nature of the intermediate phases 74

5.5 Surface atomic structure 78

5.6 Energy and specific heat 91

5.7 Summary and discussions 95

Chapter 6 MD simulation by various choice of surface potentials and sizes 103

6.1 Introduction 103

6.2 On the dependence of surface potential parameters 104

6.3 On the dependence of MD 'box' 114

A. Choice of slab thickness

B. Surface size effects

C. Box orientation effects

Chapter 7 Anharmonic surface modes and W(001) surface reconstruction phase transition: soft modes or not? 132

7.1 Introdution 132

7.2 The method 134

7.3 Results and discussion 137

Chapter 8 Incommensurate phase of Mo(001) surface reconstruction preliminary MD results 147

8.1 Introdution 147

8.2 Choice of the potentials 150

8.3 Choice of MD box 157

8.4 MD results for the Mo(001) surface reconstruction 158

References 169

PART ONE

Chapter 1

Reconstruction of the clean W(001) and Mo(001) surfaces

----- a review

1.1 Introduction

The clean W(001) and Mo(001) surfaces have been reported to reconstruct below room temperature /1,2/. Using LEED it is found that above room temperature both the W(001) and Mo(001) surfaces show the (1x1) diffraction patterns (Fig.1.1a) expected from a simple termination of the bulk structure. However, as the crystal is cooled in vacuum the pattern changes. Extra spots appear in the half-integral positions in the case of W(001) (Fig.1.1c), while a quarted of spots around the half-integral position appear in the

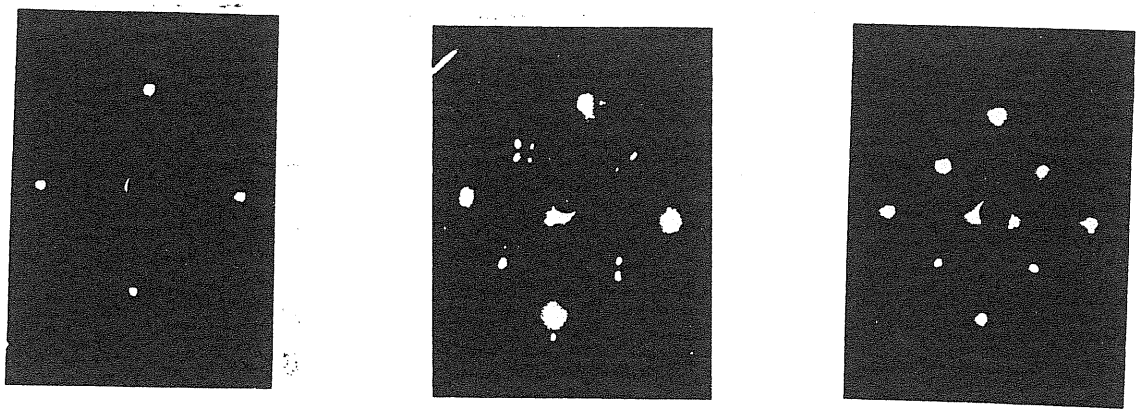

FIG. 1.1 (a) LEED pattern from clean W(100) above room temperature. Beam voltage 42 V. The pattern contains only the expected "normal" diffraction spots. Mo(100) gives an identical spot pattern. (b) LEED pattern from clean Mo(100) cooled to ~160 K. "Extra" beams are present, consisting of a quartet of spots surrounding the $(\frac{1}{2}\frac{1}{2})$ positions. The separation between the spots does not vary with temperature and is $\frac{1}{8}-\frac{1}{9}$ of the separation between the normal spots. (c) LEED pattern from clean W(100) cooled to ~160 K. The extra beams appear in the $(\frac{1}{2}\frac{1}{2})$ positions. (Ref. 1)

case of Mo(001) (Fig.1.1b) /1,2/. The variation of the half order beam intensities with temperature is found to be continuous and reversible as shown in Fig.1.2. In fact, the reconstruction on clean W(001) surface was first observed by Yonehara and Schmidt /3/, but they attributed this structure to reversible diffusion of residual hydrogen from the bulk to the surface. Felter, Barker and Estrup /1/ and Debe and King /2/ showed that the low temperature structure was a clean surface phenomenon, attributable to a continuous reversible surface phase transition. In the case of W(001) the transition is from (1x1) to reconstructed c(2x2), while

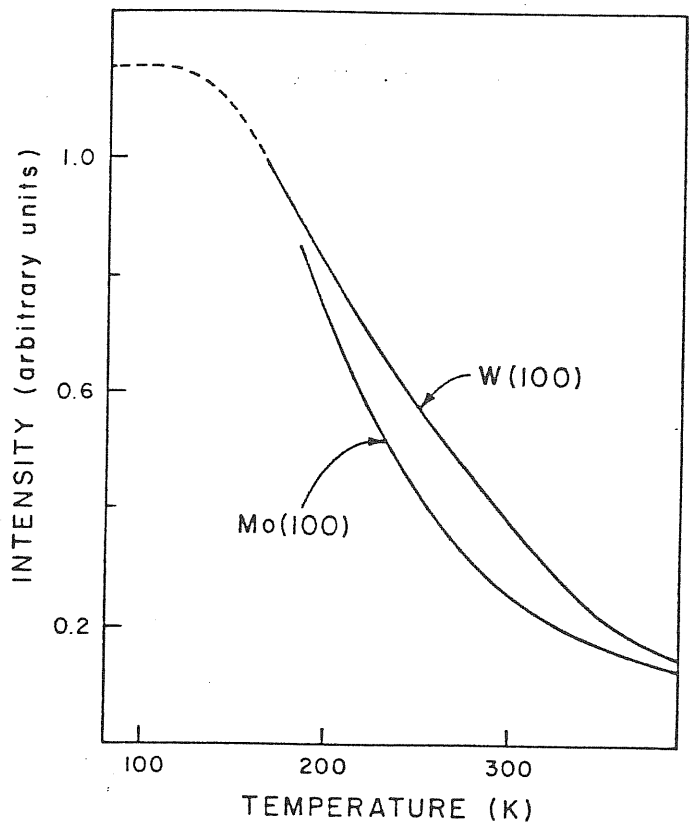

Fig. 1.2 Temperature dependence of the intensity of the "extra" diffraction spots shown in Figs.1.1(b) and 1.1(c). In the case of W(100) the intensity has been normalized to the value at 160 K. (*Ref. 1*)

the transition on the Mo(001) surface seems to be commensurate-incommensurate. Due to the continuity and gradual nature of the phase changes, it has been difficult for experiment to determine accurately the transition temperatures /1,2,5/. Thus the transition has been stated to occur between 300-400K (see Fig.1.2). Recently, Wendelken and Wang /4/ have studied the finite size effects on the phase transition in detail. Their result as shown in Fig.1.3 clarified that the phase transition takes place on W(001) surface at about Tc=210K.

These clean surface phenomena bear in many ways a resemblance to the structural phase transitions observed in ferroelectric perovskites and dichalcogenide layer compounds /60,98 /. The two-dimensional and displacive nature of these phase transitions has attracted many experimental and theoretical investigations /4-57/. The attention has been particularly focused on the atomic distortion as well as the electronic structure, the nature of the phase transition and its mechanism. In this part of the thesis we will briefly summarize the present status of these issues.

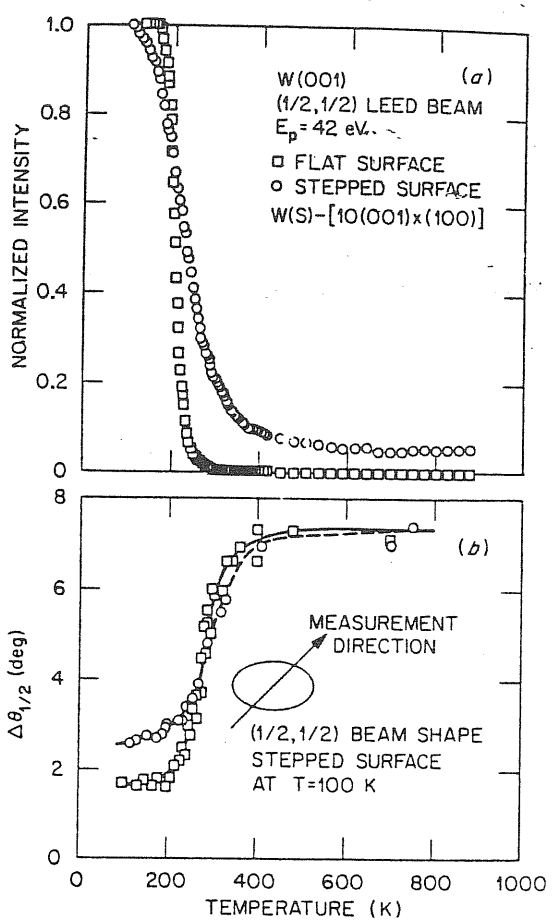

Fig. 1.3 (a) Normalized $(\frac{1}{2},\frac{1}{2})$ LEED beam intensities for flat and stepped surfaces as a function of temperature. The intensities were normalized to the Debye-Waller slope of the flat surface $(\frac{1}{2},\frac{1}{2})$ beam intensity below T_c. (b) Measured FWHM of the $(\frac{1}{2},\frac{1}{2})$ beams for both flat and stepped surfaces as a function of temperature. (Ref. 4)

1.2. The atomic structure

(A). W(001) surface at low temperature

The first structure determination of the low temperature phase of W(001) relied on a symmetry analysis of LEED I-V spectra. Debe and King /5,6/ found that only two fold symmetry was produced in the intensities at exactly normal incidence rather than the four-fold symmetry previously reported /1,2/. The I-V spetra showed 2mm point group symmetry, while the intensity differences in the half order beams showed the presence of glide lines. The space group symmetry of the domains was thus determined to be P2mg. There is only one structural model which exactly satisfies this symmetry, namely the one where the top layer atoms are periodically shifted from their bulk positions along the diagonals of the substrate mesh to form zig-zag rows paral-

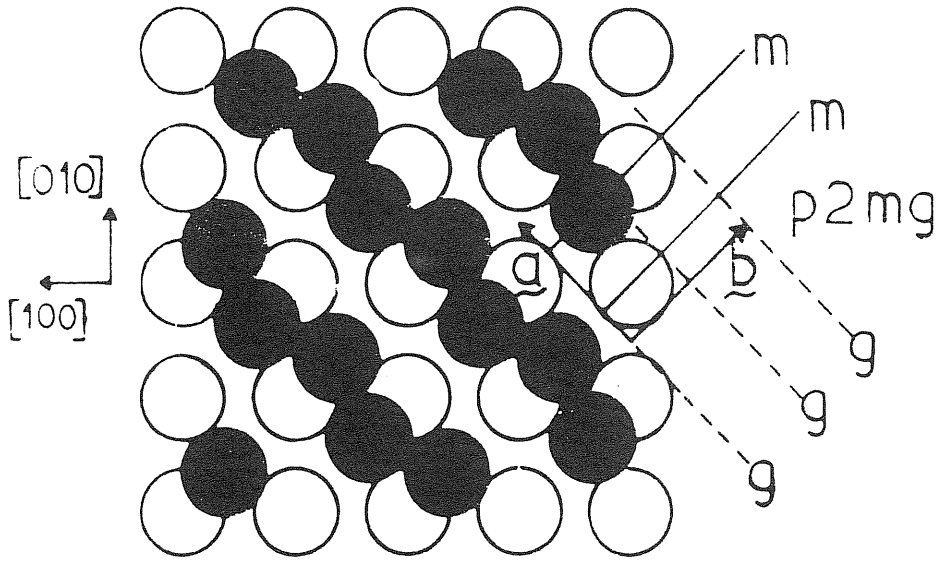

Reconstructed W (001) surface, with glide planes shown by dashed lines. (from Debe and King, ref. 5)

lel to the <110> direction, as illustrated in Fig.1.4. This model has been confirmed by the subsequent detailed LEED intensity analysis of Barker et al /7/ and Walker et al /8/. It turns out that the four fold symmetry of LEED pattern previously reported (see Fig.1.1) was due to the superposition of intensities from the other rotationally equivalent domain of the type of Fig.1.4, one related to the other by a 90° rotation. If for any reason one of the two possible orientations is preferred over the other, the rotational degeneracy is lifted. In fact the lifting of the domain degeneracy has also been observed subsequently by Barker and Estrup /18/ and by Wang and Lu /10/. Wang and Lu have shown that a stepped W(001) surface, with 28 Å average terrace width, produces a strong preferential orientation of domains in the low temperature structure with the zig-zag displacement perpendicular to the step edge. Their result of the I-V profiles for the (-1/2,1/2) and (1/2,1/2) beam is shown in Fig.1.5. The intensity of the (-1/2,1/2) beam is approximately 4.5 times greater than that of the (1/2,1/2) beam, clearly indicating a strongly preferred orientation of domains. Thus, the P2mg symmetry and hence the zig-zag structure of Fig. 1.4 for the low temperature phase of clean W(001) surface was well-established. The lateral displacement was estimated to be between 0.16 and 0.30 Å/1,8,14,18/.

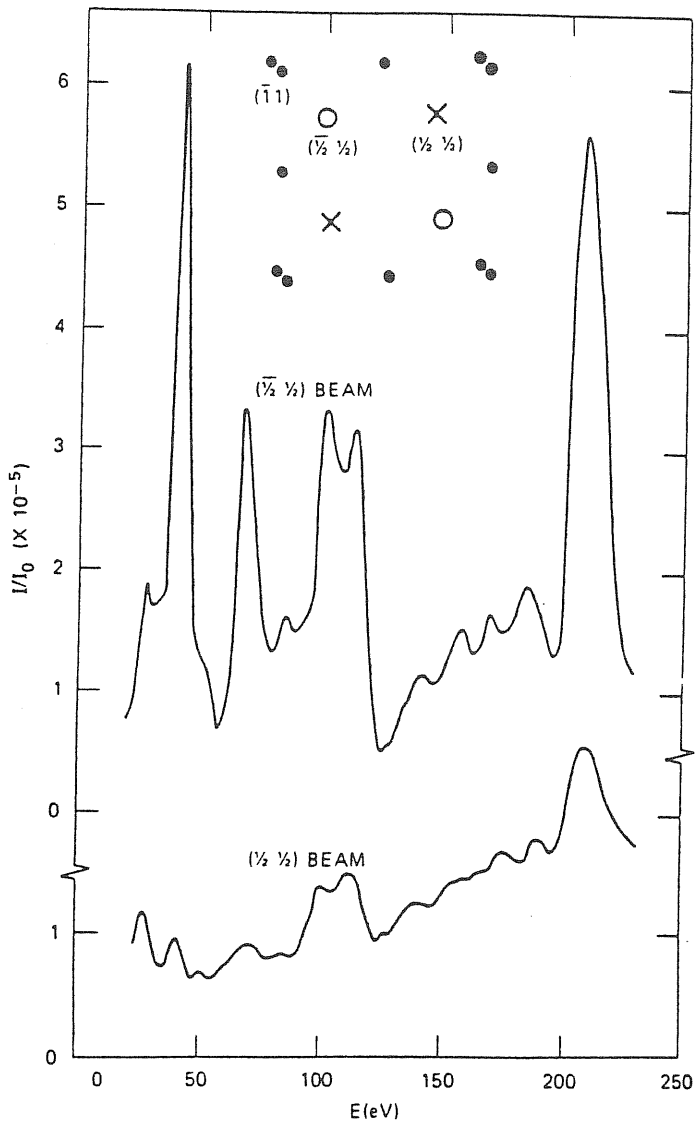

Fig. 1.5 Intensity versus energy profiles for the $(\bar{\frac{1}{2}}\ \frac{1}{2})$ and $(\frac{1}{2}\ \frac{1}{2})$ beams from the reconstructed surface with step edge parallel to the [110] direction. Insert is a schematic of the front view LEED pattern obtained at $E = 114$ eV. (Ref. 10)

It should be noted, however, that there have been also other suggestions for the W(001) surface reconstruction, although none of them seems to be as plausible as the zig-zag model of Fig.1.4. Based on the field ion microscopy (FIM) experiment, Tsong and Sweeney /12/ reported that no lateral displacements had been detected on cold W(001) and Melmed, Tung, Graham and Smith /11/ concluded that W(001) is indeed reconstructed over the temperature range 15-580K, but that the reconstructed surface contains an alternating vertical displacement of the surface atoms. In the meanwhile Rutherford backscattering experiments of 1 Mev He ions on W(001) at room temperature prove that lateral displacements of the order of 0.2 Å occur, but suggest that only 1/2 to 2/3 of the atoms are displaced /13/. On this basis Stensgaard and coworkers concluded that the zig-zag structure of W(001) is incorrect /13/. However, the theoretical first principle electronic energy calculation results, especially the recent one by Fu et al /32/, clearly show that the lateral distortion of the Debe-King type is energetically favorable, while the periodic vertical distortion structure has higher energy than that of the (1x1) surface. This results confirm that the c(2x2) reconstruction of W(001) consists of in-plane distortions rather than of vertical distortions. The results of the field ion microscopy

/11,12/ may be attributable to the possibility that the high imaging fields employed may stabilize the vertical ionic superstructure through a coupling to the external fields /32/. For the ion scattering results /13/, a more plausible explanation due to King /14/ is that the surface being investigated is not wholly reconstructed, but as we saw from the LEED results, consists of domains of c(2x2) reconstruction coexisting with (1x1) structure.

(B). W(001) surface at high temperature

The existence of the c(2x2) reconstructed structure at low temperatures suggests two alternative possibilities for the high temperature structure. The first is that the high temperature phase is a disordered version of the low temperature phase, with random lateral displacements of the surface atoms from the bulk site positions. The second possibility would be the ordered (1x1) structure, with no lateral displacement from the bulk site positions.

Debe and King strongly suggested the second possibility and argued that the reconstruction of W(001) is a displacive order-order transition/6,14,22/. On the other hand, Barker and Estrup /1/ apparently favour a disordered high temperature phase. Recently, detailed LEED study by Wendelken and Wang /4/, clarify that a short-range order persists just above the transition temperature. In fact, the ion scatter-

ing experiment results /13/, as we just mentioned, also clearly indicate the presence of a short range order structure on W(001) surface at room temperature. It seems that the true situation of the W(001) surface falls somewhere between the pure displacive and pure order-disorder limits. In this case, the fluctuations will develop domains or clusters as the transition temperature is approached /65-72,101/. Hence the system will exhibit short-range order near the transition temperature as observed /4,13/.

(C). Mo(001) surface

The half-order spot splitting in the LEED pattern from the reconstructed Mo(001) (Fig.1.1b) shows that the wavevector of reconstruction is about $2\pi/a$ (0.44,0.44) rather than $2\pi/a$ (1/2,1/2) as on W(001) /1/; the appearance of four superlattice spots rather than two at each half-order position is due to the coexistence on the surface of domains with wavevector $2\pi/a$ (+4/9,+4/9) and $2\pi/a$ (+4/9,-4/9) /15/. The similarity in the behaviour of the W and Mo(001) surface reconstructions described by Felter et al /1/ together with the similar electronic structure of these elements, suggests that the Mo(001) reconstruction resembles that of W(001), with a long wavelength modulation like $\cos(\vec{q}_0.\vec{R}_0+\varphi)$, with $\vec{q}_0 = 2\pi/a$(1/9,1/9) or $2\pi/a$ (1/9,-1/9) ($\vec{R}_0$ is a lattice vector). If the Mo(001) reconstruction is similar to that of

W(001), we would expect the atomic displacements to be either in the <11> or in the <1$\bar{1}$> direction, and this guess is confirmed by the symmetry of the LEED pattern which shows mirror planes in the <11> and <1$\bar{1}$> directions /15/. The displacements could either be parallel or perpendicular to the modulation wavevector $\vec{q}_0$ (see Fig.1.6). Barker et al. /15/ concluded that a longitudinal reconstruction occurs on Mo(001), with displacements parallel to the modulation

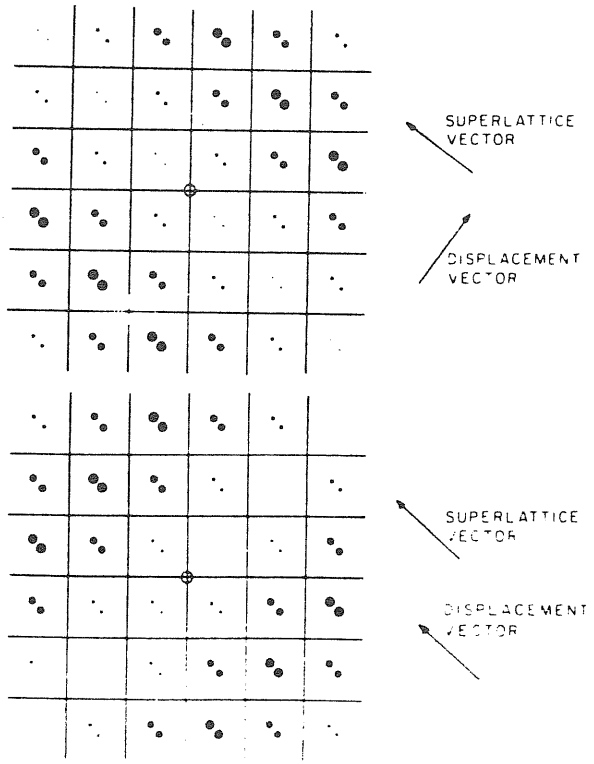

Fig.1.6 Schematic intensity of LEED spots from reconstructed Mo (001) if the displacements and modulation vectors are perpendicular (top figure) and parallel (lower figure). (from Barker, Semancik and Estrup, ref. 15)

wavevector. No detailed experimental result on the atomic distortion for both low temperature and high temperature phases are available at present.

1.3 The electronic structure

The electronic structure is very important in understanding the microscopic driving mechanism of the W(001) and Mo(001) surface reconstruction phase transitions. There have been many theoretical and experimental papers published concerning this aspect /17, 24-36/. In particular, the existence of a large surface density of states at the Fermi energy and of half—filled surface states on W(001) and Mo(001) have been reported and they are supposed to be responsible for the reconstruction phase transitions /17,37/. Fig.1.7 shows the density of states on W(001) (1x1) surface and on successive layers towards the centre of a 7-layer slab, obtained by fully self-consistent surface electronic structure calculations /24/. It is clear that the central peak at the Fermi surface is an intrinsic character of the (1x1) W(001) surface; this feature has also been confirmed by the several different theoretical calculations /25,26,27/ and photoemission experiment /17/ (see Fig.1.8). Similar features were also found for Mo(001) (1x1) surface /28,29/ as shown in Fig. 1.9. The central peak is made up of surface states,i.e., states localized at the surface which

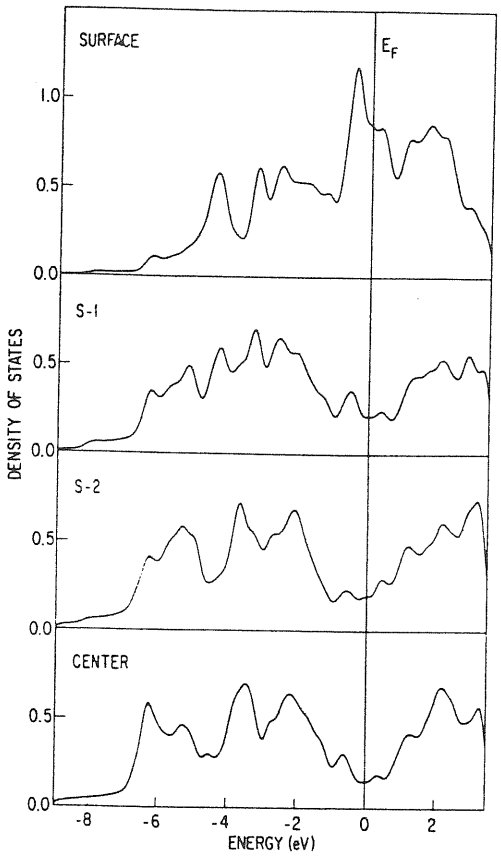

Fig. 1.7 W (001) (1 x 1) surface density of states, and on successive layers towards the centre of a 7-layer slab. (from Posternak, Krakauer, Freeman and Koelling, ref. 24)

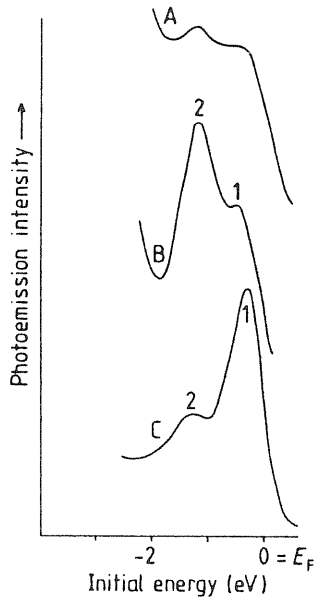

Fig. 1.8 Photoemission energy distribution for electrons emitted with $K \approx (\pi/a, \pi/a)$ from W (001) (1×1) (curve A) and $(\sqrt{2}\times\sqrt{2})$ R45° structure (curve B). Features 1 and 2 occur at same energies as features in normal emission (curve C) (Campuzano *et al* 1981). Ref. 17

decay exponentially into the bulk as well as in the vacuum, and surface resonances which have a large amplitude at the surface and decay slowly into the bulk. These surface states and resonances occur over a large part of the surface Brillouin zone as one can see from the LAPW slab calculation /31/ (Fig.1.10) and photoemission experiment /17/ (Fig.1.11). It is clear that the half filled surface states (labelled as 2 in Fig.1.11) are well defined; they are very close to the Fermi surface and have upwards dispersion across the Fermi surface halfway along Σ (Fig.1.11 and Fig.1.12). These half filled surface states are believed to play an important role in driving the surface reconstructions of W(001) (as well as Mo(001)). In fact the c(2x2) reconstruction of W(001) produces new surface Brillouin zone boundaries halfway along Σ as shown in Fig.1.13. Surface states at $k=2\pi/a$ (1/2,1/2) are then coupled by the change in surface potential to equivalent states at $k=2\pi/a$ (-1/2,-1/2), opening up a band gap over the Zone boundary along Σ parallel to the direction of atomic displacements. Several theoretical calculations /26,27,32/ have shown the splitting of surface density of states at Fermi level upon the reconstruction, particularly the most recent 'ab initio' results of Fu et al /32/ shown in Fig.1.14.

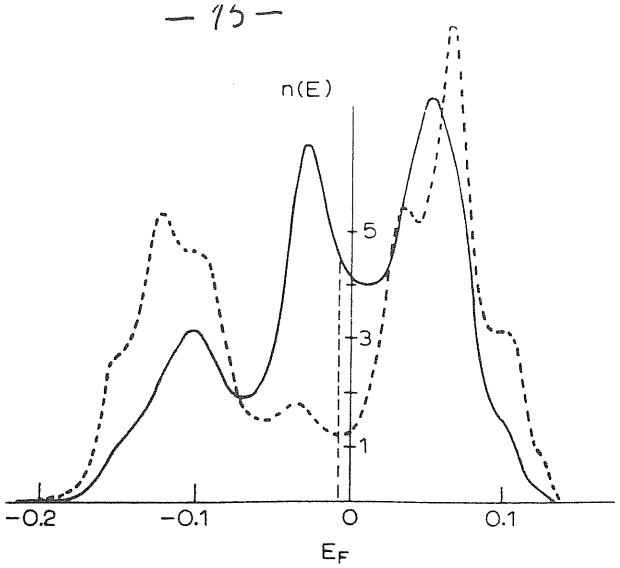

Fig. 1.9 Mo (001) surface density of states (solid line), and density of states on second layer (close to bulk) (dashed line), from tight-binding calculation.
(from Desjonquères and Cyrot-Lackman, ref. 28)

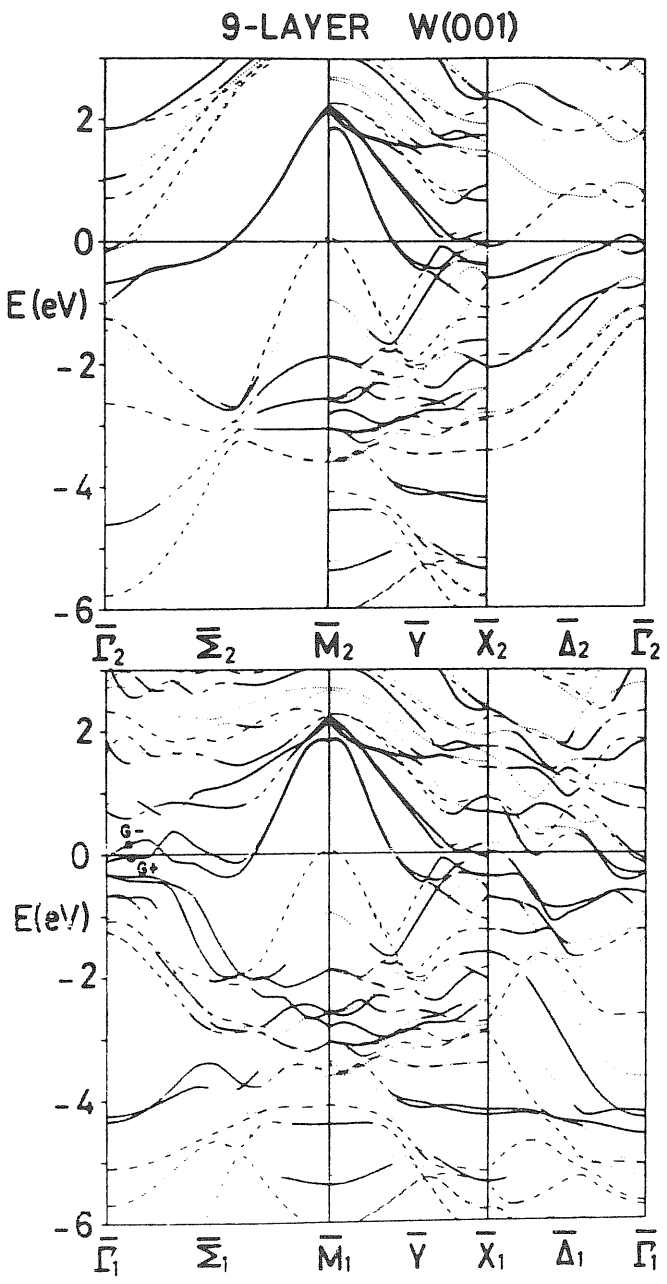

Fig. 1.10 Dispersion of surface states and surface resonances on W (001) (1 x 1); solid lines indicate highly localized states. The lower curves show states which are even with respect to reflection in the plane containing $\bar{K}$, and the

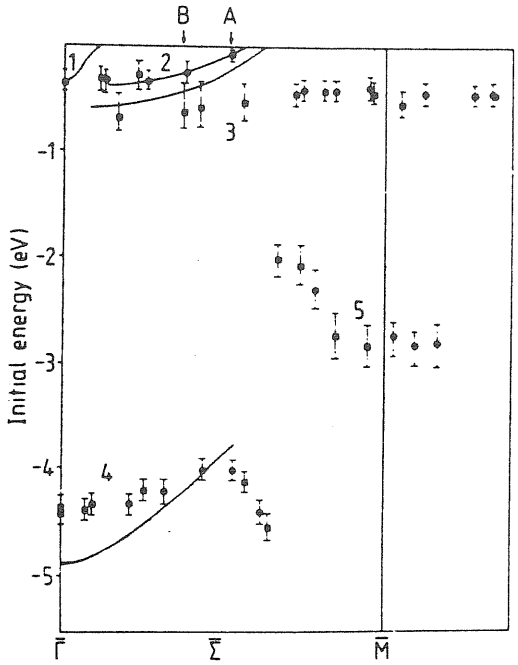

Fig. 1.11 Experimental dispersion of surface states and resonances on W (001) (1 x 1). Solid lines show early theoretical predictions (ref. 24).
(from Campuzano, Inglesfield, King and Somerton, ref. 17)

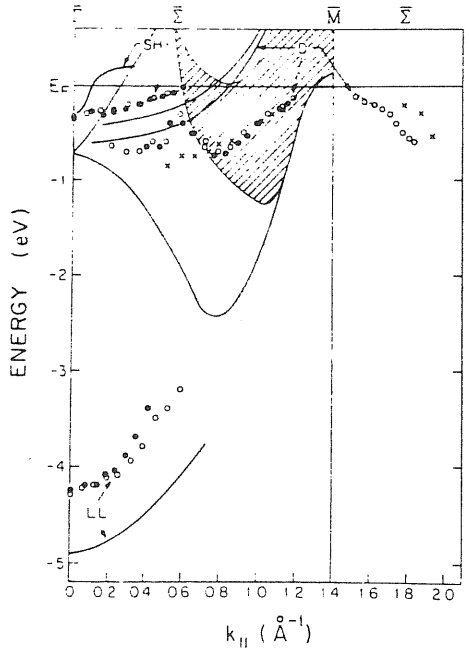

Fig. 1.12 Experimental dispersion of surface states and resonances on W (001) (1 x 1). Circles mark even states and crosses odd states, with respect to reflection in the mirror plane containing $\underset{\sim}{K}$. (from Holmes and Gustafsson, ref. 33)

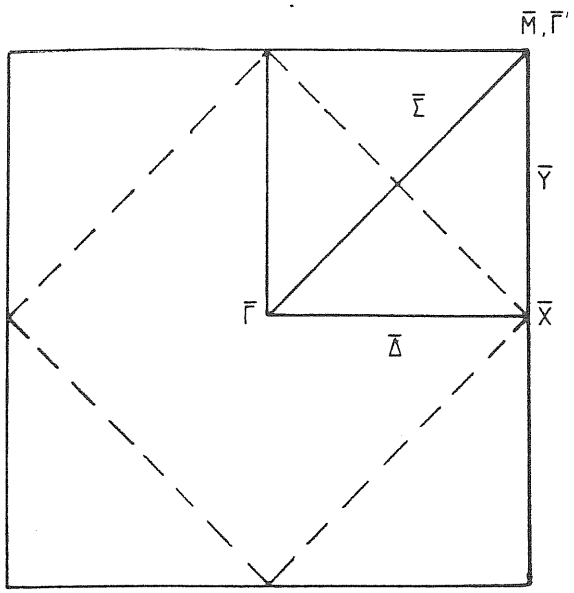

Fig. 1.13 Brillouin zone boundaries for W (001) (1 x 1) (outer solid line) and ($\sqrt{2}$ x$\sqrt{2}$)R45° reconstruction (dashed line).

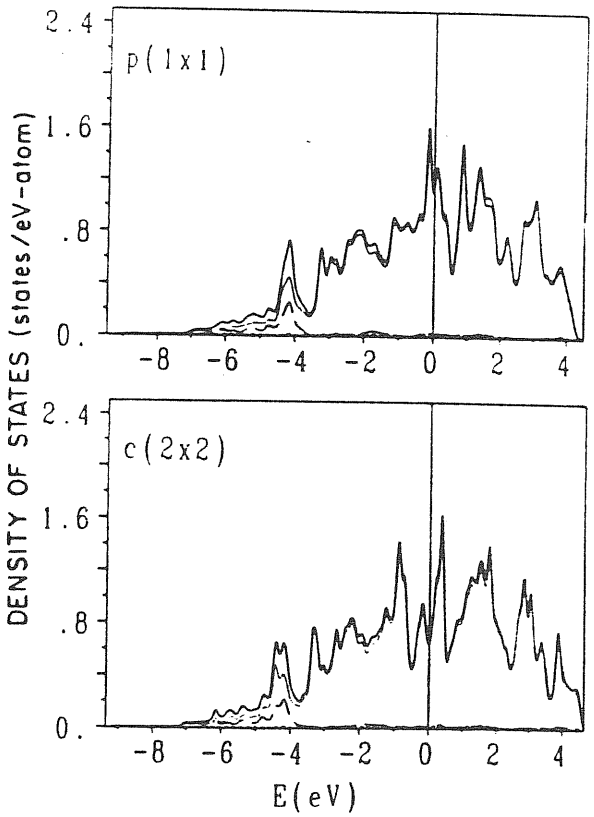

Fig. 1.14 Surface density of states for W (001) (1 x 1) (top figure) and ($\sqrt{2}$ x$\sqrt{2}$)R45° reconstruction (lower figure). (from Fu, Freeman, Wimmer and Weinert, ref. 32)

1.4 Driving force for the surface reconstruction

The occurrence of a displacive reconstruction at low temperature on W(001) and Mo(001) surfaces obviously indicates that somehow a periodic surface lattice distortion act to lower the total energy, but the detailed mechanism is not completely understood.

In general, for such a complicated electron-phonon coupling system, we may phenomenologically write the energy change upon the reconstruction as

$$\Delta E = E_{dist.} - E_{undist.} = \Delta E_{latt.} + \Delta E_{elec.} \qquad (1.1)$$

where $\Delta E_{elec.}$ is the change of electronic energy which is in favour of distortion and act to drive it. $\Delta E_{latt.}$ is an elastic or lattice energy which is against the distortion. Thus $\Delta E_{latt.} > 0$, $\Delta E_{elec.} < 0$, and at T=0 $\Delta E < 0$.

As the temperature is raised, entropy comes into play

$$\Delta F = \Delta E_{latt.} + \Delta E_{elec.} - T(\Delta S_{latt.} + \Delta S_{elec.}) \qquad (1.2)$$

The electronic entropy is usually reduced by the distortion $\Delta S_{elec.} < 0$, since on average the energy gain is realized by splitting apart filled and empty electronic states. The lattice entropy change is also negative $\Delta S_{latt.} < 0$ because the distortion generally stablizes the systems, making the lattice stiffer, with higher vibration frequences than the undistorted state at same temperature. Thus, the entropy

piece has opposite sign to ΔE and the distortion decreases with temperature until the phase transition is reached at $\Delta F\ (T=Tc) = 0$.

Estrup /1,18/ and Tosatti /37/ conjectured that half-filled surface state band (see previous section) and ensuing surface charge- density-wave (SCDW) could be the driving force of the transitions, as in an early model proposed for Si and Ge(111) by Tosatti and Anderson /38/. In this model the energy gain in the low temperature phase is produced by displacement-induced rearrangement of the surface electrons just below E_f. If the Fermi surface has flat parallel regions, it will become energetically favourable for a reconstruction to occur with the wavevector which spans the Fermi surface, so that an energy gap opens up over the flattened regions. Several earlyer calculations /27,29/ for the W(001) surface predicted a flat line of surface states at E_f in the surface Brillouin zone, and it was thus suggested that surface phase transitions were due to an analogous CDW instability. However, the angle-resolved photoemission experiments show a very curved surface state Fermi line (Fig.1.15) /17/ and the weak coupling charge density wave mechanism /33/ becomes untenable.

Rather than half-filled surface states at a particular point in the surface Brillouin zone drivin the transition, more general features of the surface electronic density of

states are probably responsible for the reconstruction. Indeed, on general grounds, we would expect some sort of instability because E_f is close to the central peak in the surface density of states, and hence any atomic displacements which broaden or split the peak would lower the energy thus providing the driving force for the reconstruction. It turns out that for a large distortion the details of the reconstruction periodicity are not dictated by the shape of the 2D Fermi surface. Tosatti has referred to this state of affairs as a 'strong coupling CDW' /39/ while Ying et al. /20,40/ prefer to call it a 'short-range John-Teller effect'. The important issue is that the effective driving force for the W(001) and Mo(001) surface reconstruction is short-ranged in nature. The interatomic forces are better described by a chemical bond picture rather than that of original CDW /37/.

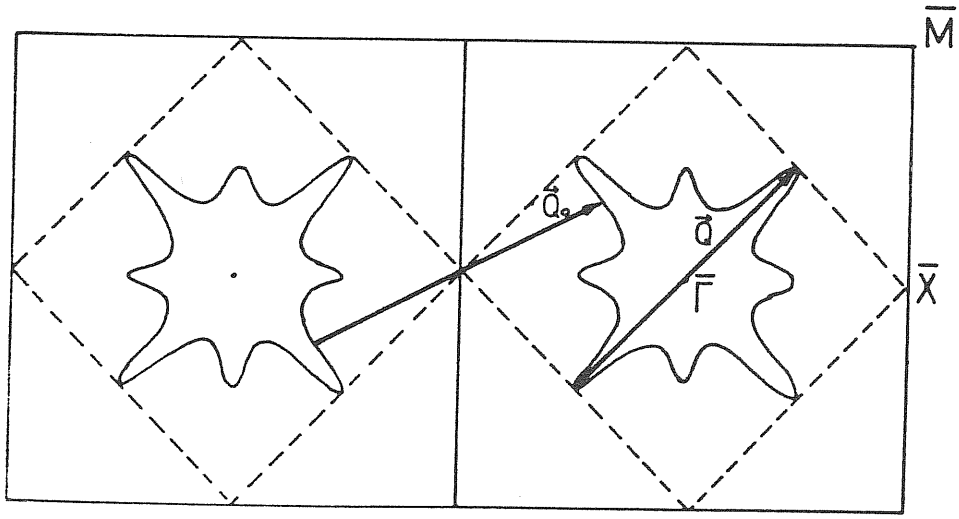

Fig. 1.15 The Fermi surface of surface states found on W{100} (1 X 1), replotted from Campuzano et al. [17] in the extended zone scheme. Q and Q_0 are possible CDW nesting vectors. Dashed lines represent the zone boundaries of the L phase.

1.5 Lattice distortion versus frozen-in surface phonon

Like in other structural phase transitions /60,98 /, the reconstruction of the W(001) and Mo(001) surface may be considered to be associated with the softening of surface vibration modes /39,41/. When a structural phase transition proceeds via a 'soft-mode' instability, it is possible to present the static distortions characterizing the structural rearrangements by a set of 'frozen-in' phonon-like displacements.

For a (1x1) W(001) surface the symmetry of the k-point $M = 2\pi/a(1/2,1/2)$ is the full point group C_{4v}; there can thus be two types of surface phonons at M, those with up and down Z motion of the first layer atoms (symmetry M1, nondegenerate) and those with in-plane (x+y) motion (symmetry M5, twofold degenerate). It is easy to convince oneself that the distortion of the Debe King type (Fig.1.4) corresponds exactly to the first layer piece of eigenvector expected for the latter M5 mode /37/. The twofold degeneracy results in the possibility of two equivalent distortion at 90° from one another, which should give rise to domains, with wall type defects between them.

The reconstruction of Mo(001) surface is characterized by the star $K = \Sigma = 2\pi/a(0.44,0.44)$/1/. The point group at Σ is Cs, with two representations Σ_1, even under a mir-

ror plane containing the <11> direction, and Σ_2, odd. Since Σ is not very far from the M point, it is most likely that the distortion should correspond to one of the two modes that connect with M5. Of these, one is Σ_1 and other Σ_2. LEED symmetry analysis is in favour of a Σ_1-type distortion /15/. Fasolino, Santoro and Tosatti /41/ and Fasolino and Tosatti /97/ have proposed that the long wave length modulated incommensurate reconstruction arises not because of long-range interactions between the atoms, but rather from a coupling between two soft modes, one with displacements perpendicular to the surface (M1) and one in the plane of the surface (M5). The mechanism is illustrated in Fig.1.16. Incommensurability arises when the

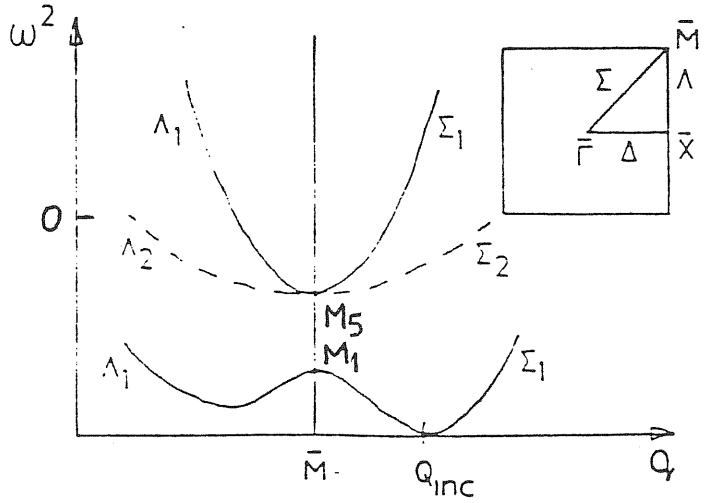

Fig.1.16 Phonon soft mode coupling between M5 and M1 symmetry modes to produce incommensurate wave-vector Q_{inc}.

two different soft-mode, the planar M5 mode and the vertical M1 mode - are both unstable and very close in (imaginary) frequency. If they could mix, one of the two mixed modes would end up being lowest. Symmetry of course prevents mixing at the M-point. However, mixing becomes allowed away from the M-point, where the symmetry is lowered. For k along either <11> or <10>, the M1-compatible mode and one member of the twofold degenerate M5-compatible modes have same symmentry. As the M1 and M5 frequencies cross each other this leads to a range where the lowest mode is at an incommensurate wavevector.

1.6 Landau description of the W(001) and Mo(001) surface phase transition

The phenomenological Landau and Landau-Ginzburg hamiltonians approach to the W(001) and Mo(001) surface phase transitions has been described by several authors /19,20,21,37,42,43/. In this approach the change of energy (or free-energy at $T \neq 0$) upon reconstruction is cast in the form of a power series of one or more order parameters. While the nature of the order parameter is dictated by physical considerations, the detailed form of the expansion relies solely on symmetry /59/.

The wave vector characterizing the reconstructed phase of W(001) is $\vec{K1} = \frac{2\pi}{a}(1/2,1/2)$. The corresponding distortion

pattern is

$$\vec{u}_1(\vec{r}) = u_1 \hat{K}_1 \exp(i\vec{K}_1 \cdot \vec{R}) \qquad (1.3)$$

where $\hat{K}1$ is a unit vector along $\vec{K}1$. This structure is degenerate with the distortion

$$u_2(\vec{r}) = u_2 \hat{K}_2 \exp(i\vec{K}_2 \cdot \vec{R}) \qquad (1.4)$$

where $\vec{K}2 = \frac{2\pi}{a}(-1/2, 1/2)$ is related to K1 through the fourfold axis. The order parameter thus is two dimensional $\rho e^{i\varphi} = (u_1, u_2)$. The corresponding Landau hamiltonian is

$$F = \frac{1}{2} r (u_1^2 + u_2^2) + a (u_1^2 + u_2^2)^2 + v u_1^2 u_2^2 + \frac{1}{2}(\nabla u_1)^2 + \frac{1}{2}(\nabla u_2)^2 + \cdots \qquad (1.5)$$

This is the most general form which is invariant under the symmetry operations of the C4v group of the W(001) surface. From the phase transition point of view, this hamiltonian represents a 2D X-Y model with cubic anisotropy given by the v-term. There are three possible continuous phase transitions depending on the sign of v. 1). $v>0$, the ordered phase has one of four domains ($u_1 = \pm\rho$, $u_2 = 0$ or $u_1 = 0, u_2 = \pm\rho$); 2). $v<0$, in this case there are four ordered domains with $u_1 = u_2 = \pm\frac{1}{\sqrt{2}}\rho$; 3) $v=0$, in this case the ordered phase may take up any orientation in the space of u_1 and u_2. The stability of the two types of domains given by

(1.3) and (1.4) respectively requires $\gamma > 0$ for clean W(001) surface. However, the adsorption of a small coverage of hydrogen causes symmetry switching from atomic displacements along <11> to <10> directions /18,47/ associated with γ changing sign. Since very small amount of H-coverage was found able to cause such switching, evidently, the anisotropy is very small for W(001).

The critical behaviour of an X-Y model with cubic anisotropy is expected to depend on the actual physical interactions (non-universality). Ying et al. have gone into considerable more detail and have investigated the switching from pure X-Y (Kosterlitz-Thouless) to non-universal, roughly Ising-like behaviour in the presence of cubic anisotropy /19,20,21,40/. Using Monte Carlo simulation and renormalization group techniques, Ying and Roelofs /40/, Roelofs, Hu and Ying /19/ and Roelofs /21/ have studied a two-dimensional X-Y model with cubic anisotropy which has the appropriate symmetry of the (1x1) to c(2x2) transition on W(001) surface. Their results of these finite temperature studies clarify the gradual development of short range order as one approaches the transition from above and resolve some apparent experimental inconsistencies /19/. Other quantities such as the temperature-coverage phase diagram are also calculated. However, a detailed quantitative comparison with the experimental data is not possible because the two-dimensional model hamiltonian used in these studies is too

simple to represent the true W(001) surface in detail.

The incommensurate phase arises on Mo(001) because of the competition between tendencies to distort vertically and horizontally as we have discussed in the previous section. Hence, both types of degrees of freedom must be included in the Landau Ginzburg hamiltonian. The horizontal distortion consists of frozen—in M5 (two-fold degenerate) vibration mode and we need a two-dimensional order parametr $\rho e^{i\varphi} = (u_1, u_2)$ to describe them. The other order parameter for describing the vertical M1 distortion is V. The general form of Landau Ginzburg hamiltonian for the three component order parameter system has been carried out by Fasolino and Tosatti /43/. It reads

$$
\begin{aligned}
F = \int d\vec{r} \{ & -r(u_1^2 + u_2^2 + V^2) + a(u_1^2 + u_2^2 + V^2)^2 \\
& + \Delta V^2 \\
& + b u_1^2 u_2^2 + b_1 (u_1^2 + u_2^2) V^2 \\
& - \delta [(u_1 \vec{\nabla}_{11} V - V \vec{\nabla}_{11} u_1) + (u_2 \vec{\nabla}_{1\bar{1}} V - V \nabla_{1\bar{1}} u_2)] \\
& + J_0 [(\vec{\nabla} u_1)^2 + (\vec{\nabla} u_2)^2] + J_1 (\vec{\nabla} V)^2 \}
\end{aligned}
\qquad (1.6)
$$

where the term ΔV^2 accounts for the energy splitting

between M5 and M1 modes. The incommensurability is driven by the 'Lifshitz term' proportional to δ. The competition leading to incommensurability occurs between u_1 and v in the <110> direction, and between u_2 and v in the $\langle 1\bar{1}0\rangle$ direction.

Let us transform the hamiltonian from the form of e.q (1.6) into polar coordinates, by putting

$$(u_1, u_2, v) = (\rho \sin\theta\cos\varphi,\ \rho\sin\theta\sin\varphi,\ \rho\cos\theta)$$

hence

$$\begin{aligned} F = \int d\vec{r}\,\{ & -r\rho^2 + a\rho^4 + \rho^4[b\sin^2 2\varphi(2\sin^2\theta - \sin^2 2\theta) + 2b_1\sin^2 2\theta] \\ & + \Delta\rho^2\cos^2\theta \\ & + \delta\rho^2[\vec{\nabla}_{11}\theta\cos\varphi + \vec{\nabla}_{1\bar{1}}\theta\sin\varphi + \sin 2\theta(\vec{\nabla}_{1\bar{1}}\varphi\cos\varphi - \vec{\nabla}_{11}\varphi\sin\varphi)/2] \\ & + J_0\rho^2[(\vec{\nabla}\theta)^2\cos^2\theta + (\vec{\nabla}\varphi)^2\sin^2\theta] + J_1\rho^2(\vec{\nabla}\theta)^2\sin^2\theta\} \end{aligned}$$

(1.7)

where an additional ('phase-only') approximation of constant amplitude, $\vec{\nabla}\rho = 0$ has been introduced.

E.q (1.7) represents a functional $\Delta E = \Delta E[\theta(r), \varphi(r)]$ of two phase θ , φ . The minimization of this functional should yield the two functions $\theta(\vec{r})$ and $\varphi(\vec{r})$ which describe the true nature of the incommensurate surface structures of Mo(001).

With the additional assumption φ = constant = $n\pi$, one of the two components u_1 or u_2 is set equal to zero. The hamiltonian (1.7) is reduced to

$$F = \int d\vec{r} \{ -r\rho^2 + \rho^4(a + 2b_1 \times \sin^2 2\theta) + \Delta\rho^2 \cos^2\theta + \delta\rho^2 \vec{\nabla}_{11}\theta + J_0\rho^2[(\vec{\nabla}\theta)^2\cos^2\theta + J_1\rho^2(\nabla\theta)^2\sin^2\theta \} \quad (1.8)$$

This type of hamiltonian will lead to soliton lattice of Fig. 1.17. The physical picture of the incommensurate phase here consists of domain of commensurate region with in-plane displacement separated by solitons (anti-phase domain walls) in which there are mixed parallel and perpendicular displacements, as have been discussed by Ying et al. /44/ and illustrated in FIg. 1.18.

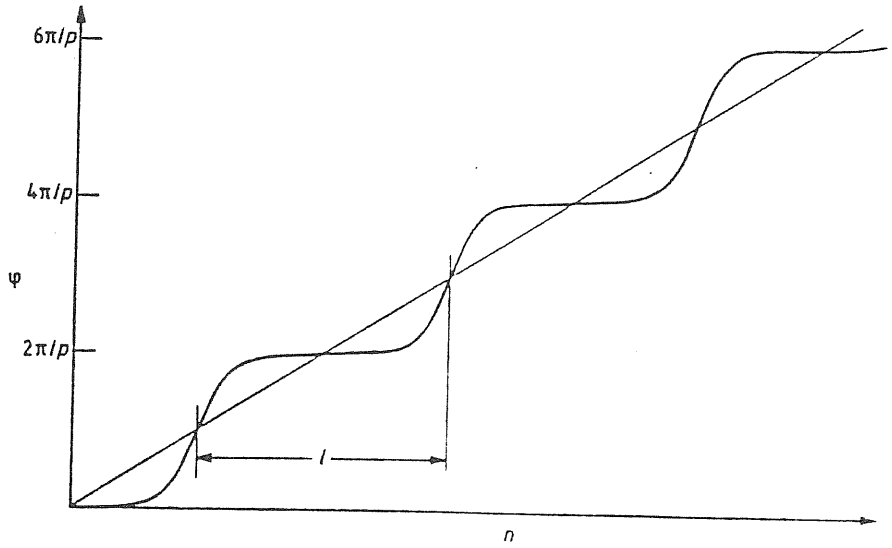

Fig. 1.17 Regular soliton lattice solution to the sine-Gordon equation . The straight line corresponds to an unperturbed incommensurate structure.

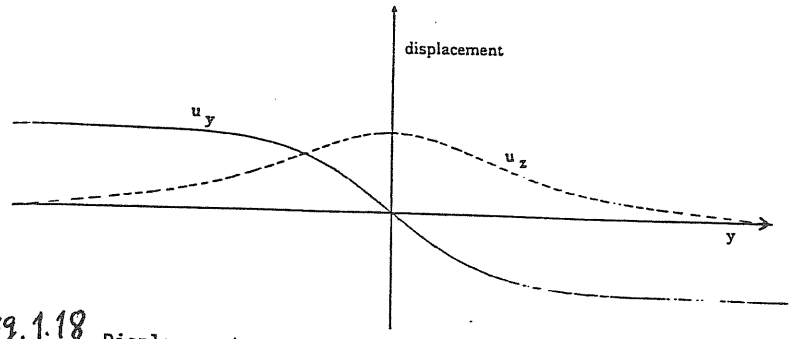

Fig. 1.18 Displacement pattern in an anti-phase domain wall of the incommensurate phase

1.6 Effective lattice hamiltonian description of W(001) and Mo(001) surface reconstructions

In the spirit of the strong-coupling CWD and short-range driving force, an effective lattice dynamical model for the W(001) and Mo(001) surface reconstructions has been proposed by Fasolino, Santoro and Tosatti /39/. In this model, the reconstructions have been treated as an 'effective' lattice phenomenon. Electrons are integrated out, their driving effect being represented by extra forces between surface atoms. The lattice hamiltonian for the description of the W(001) and Mo(001) surface is

$$\mathcal{H} = \sum_i \frac{p_i^2}{2m} + \frac{1}{2}\sum_{\substack{(i,j)\\ \neq \langle i,j\rangle}} V^B(|\vec{R}_i - \vec{R}_j|) + \frac{1}{2}\sum_{\substack{\langle i,j\rangle \\ = \text{first Surface neighbors}}} V^S(|\vec{R}_i - \vec{R}_j|) \qquad (1.10)$$

where $V^B(R)$ is supposed to describe the bulk lattice properties of W(or Mo) and $V^S(R)$ is the interaction potential between pairs of surface atoms $\langle i,j\rangle$, which represents an effective electronic driving effect arising from the half-filled surface electronic states. $V^B(R)$ is in general different from $V^S(R)$ as required by the different electronic structures of the surface and of the bulk. Both $V^B(R)$ and $V^S(R)$ are taken to be pairwise and short-ranged. If a pair of atoms is first or second neighbour and is not at the same surface(bulk neighbours) they interact via $V^B(R)$. On the

other hand, pairs of first neighbour atoms on the same surface interact via $V^S(R)$. Further interactions are not included.

The potentials (both $V^B(R)$ and $V^S(R)$) in the hamiltonian (1.10) have been expressed as a simple expansion to the fourth order, namely

$$V_i(R) = R_{oi}^2 \left[\alpha_i \left(\frac{R}{R_{oi}} - 1 \right) + \frac{1}{2!} \beta_i \left(\frac{R}{R_{oi}} - 1 \right)^2 + \frac{1}{3!} \gamma_i \left(\frac{R}{R_{oi}} - 1 \right)^3 + \frac{1}{4!} \delta_i \left(\frac{R}{R_{oi}} - 1 \right)^4 \right] \qquad (1.11)$$

where

$$\alpha_i = \left(\frac{1}{R} \frac{\partial V_i}{\partial R} \right)_{R_{oi}} , \quad \beta_i = \left(\frac{\partial^2 V_i}{\partial R^2} \right)_{R_{oi}} ,$$

$$\gamma_i = \left(R \frac{\partial^3 V_i}{\partial R^3} \right)_{R_{oi}} , \quad \delta_i = \left(R^2 \frac{\partial^4 V_i}{\partial R^4} \right)_{R_{oi}} \qquad (1.12)$$

represent harmonic and anharmonic force constants which are treated as parameters and i=1,2,s are the subscripts for the first bulk neighbour, second bulk neighbour and first surface neighbour respectively.

Although such a model cannot directly elucidate the underlying electronic mechanism, it does allow a detailed calculation of the thermal and structural behaviour of the reconstruction phase transition. Fasolino et al /39,41/ took the first step toward this goal by analyzing the phonon mode instabilities and showing that all the experimentally

observed phases, including the (clean surface) c(2x2) and the incommensurate phase that occurs on Mo(001) can be accounted for by an appropriate choice of surface force constant. Fig.1.19 shows the phase diagram obtained by such stability analysis for both W(001) /39,43/ and Mo(001) /41/ surfaces. By choosing the surface harmonic force constant in the M5 region of Fig.1.19, $\alpha_S = -0.496$ eV/A, $\beta_S = -0.914$ eV/A for example, the M5 mode of the (1x1) W(001) surface is found to be soft at M point as shown in Fig.1.20 /39,43/. The commensurate c(2x2) reconstructed structure of Fig.1.4 is then realized by freezing-in such a soft phonon mode. On the other hand, Fig.1.21 shows how an absolute minimum in the frequency can occur slightly off the M point, corresponding to the incommensurate distortion on Mo(001) surface according to the mechanism outlined previously in section 1.4, when the surface potential parameters are appropriate chosen such that the M5 (in plane) and the M1 (vertical) soft mode happens to come sufficiently close in energy /41/.

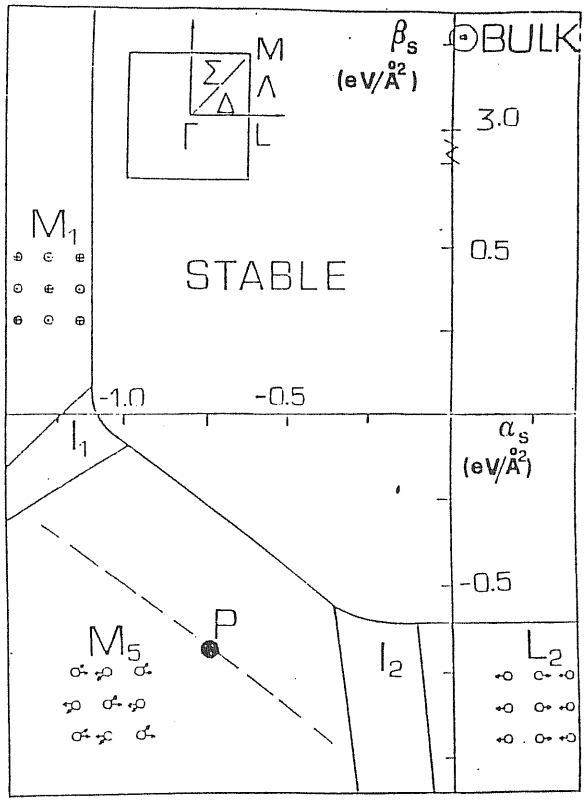

Fig. 1.19 (a) T=0 phase diagram as a function of the surface force constants of W (100). (from Fasolino, Santoro and Tosatti, ref. 43

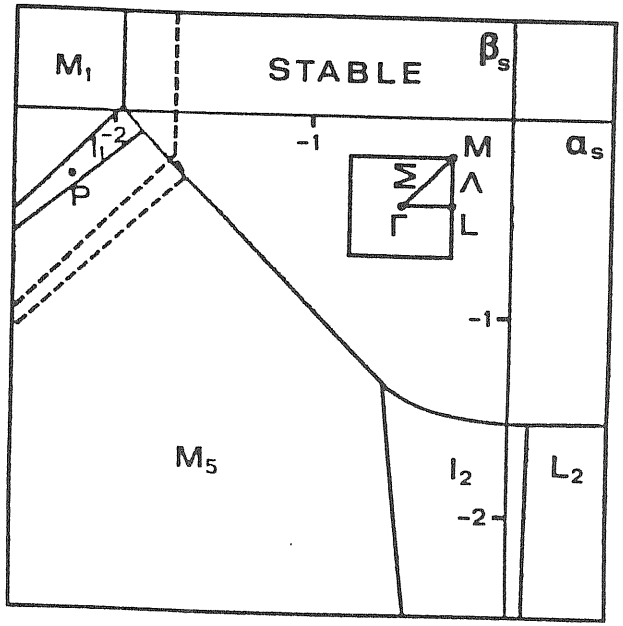

Fig. 1.19 (b). T=0 phase diagram as a function of the surface force constants of Mo (100). (from Fasolino, Santoro and Tosatti, ref. 41)

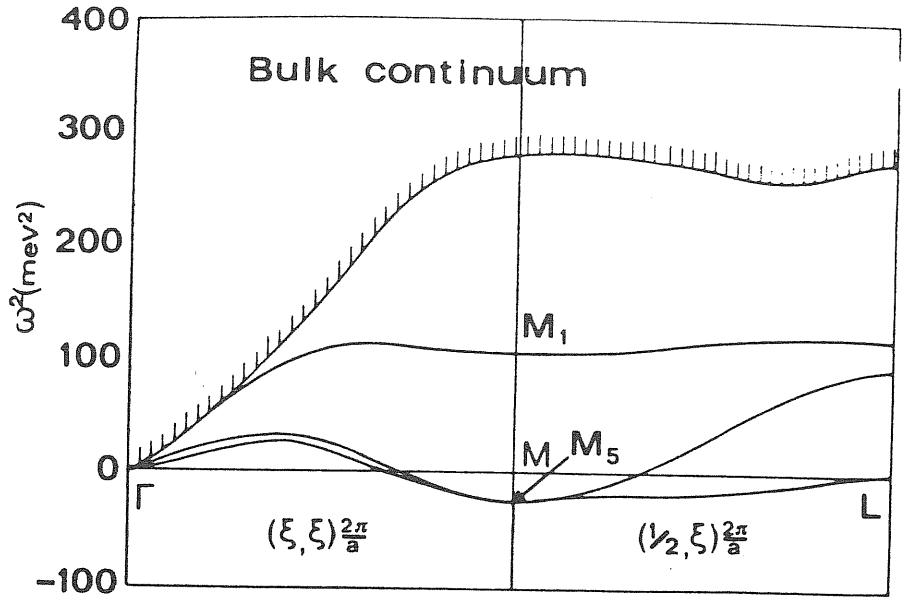

Fig. 1.20 Frequency (squared) of surface phonons on W (001) (1 x 1) from lattice dynamical calculations. (from Fasolino, Santoro and Tosatti, ref. 39)

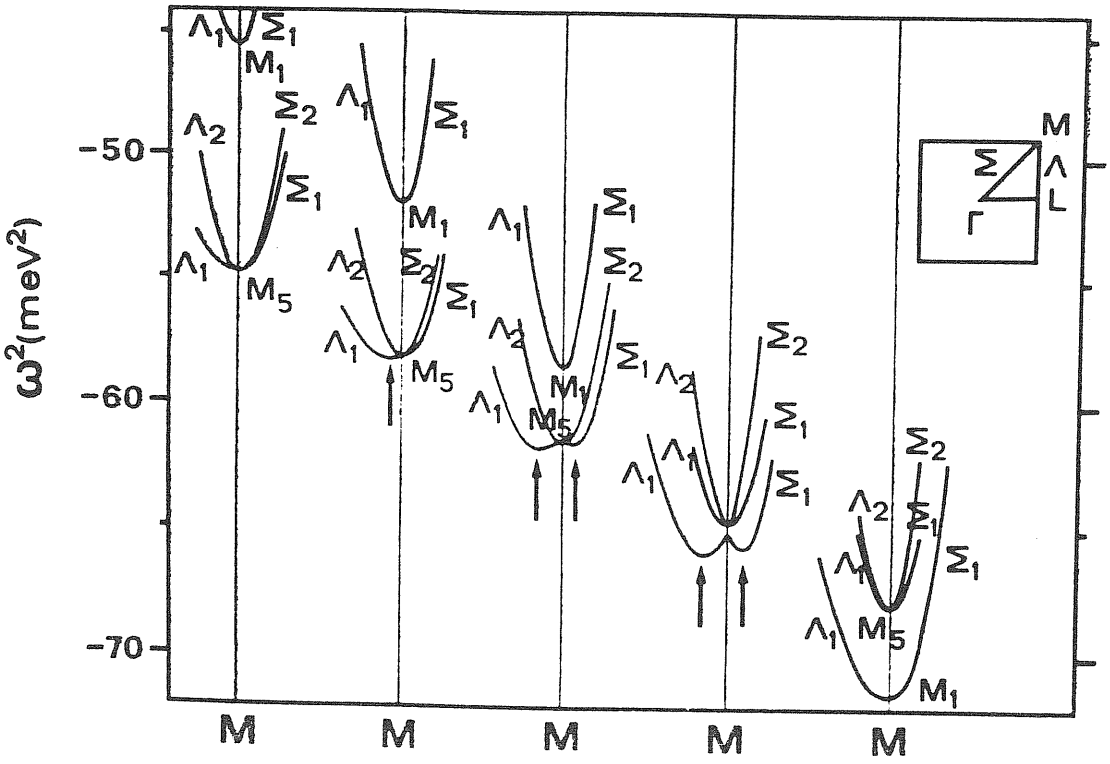

Fig. 1.21 Surface phonon branches of Mo(100) along the Σ and Λ directions (from Fasolino, Santoro and Tosatti, ref. 41)

PART TWO

Chapter 2
An introduction to Part two

Although the nature as well as the mechanism of the W(001) and Mo(001) surface reconstruction phase transitions have been widely studied, they are still far from being completely understood. The motivation of this thesis is to provide a quantitative description of the temperature-dependent static and dynamical properties of these surface reconstruction phase transitions. As we have discussed previously, the electrons in the half—filled dangling-bonds form a complicated coupled electron-lattice system. The exact solution of such a system needs to take into account both the electronic and lattice degrees of freedom, which is of course too complicated to handle at present. However, due to the negligible contribution of the electronic entropy and to the short-ranged nature of the interactions in the 'strong-coupling' electron-phonon system, an effective lattice formulation is useful for the study of the W(001) and Mo(001) surface reconstruction phase transitions. Once the electronic force is modeled, the remaining lattice problem can be dealt with quantitatively. Then a number of detailed issues, ranging from distortion geometries and energies to lattice vibrations and all the way to statistical mechanics of the reconstruction phase transition, becomes immediately tractable. Although several lattice model hamiltonians have

been proposed in this spirit /39,19 - 23, 40/, it seems that the two-dimensional lattice hamiltonians used by Ying et al /19 - 23,40/ are too simple to address many of the problems related to the W and Mo(001) surface reconstructions, like the presence of incommensurate phase, effects of surface relaxation and so on. In fact, the second or deeper layers degrees of freedom which might affect strongly the surface reconstruction phase transition are absent in their hamiltonians. We believe that the full three-dimensional approach of Fasolino et al /39/ is more appropriate for a complete understanding of these phenomena. Based on stability studies performed on slabs, Fasolino et al. /39,41,43/ have shown that the commensurate c(2x2) reconstruction of W(001), as well as the incommensurate reconstruction of Mo(001) may appear quite naturally, once the effective intra-surface forces are made sufficiently different from their bulk values. In particular, it is interesting that in this case incommensurability can arise due to strong competition between direct atom-atom forces in the surface and opposing indirect forces that are mediated through the second and deeper layers /43/. This approach provided useful information concerning the mechanism of surface reconstructions. However, Fasolino's lattice dynamical method is unable to determine the optimum force constants for the

W(001) and Mo(001) surfaces since only the static information can be used as input. Moreover, the restriction of the method to zero temperature does not allow a study of the temperature-dependence of the structural phase transition of the W(001) and Mo(001) surfaces; hence a detailed quantitative comparison with the experiments is not possible. Such difficulties can be resolved by using the technique of molecular dynamics. Since according to the effective lattice hamiltonian (1.10), the system is classical with pairwise interactions, the well established MD technique for the simulation of classical systems can be applied directly. Then the temperature-dependence of the distortion geometries and energies, the lattice dynamics and the statistical mechanics of the reconstruction phase transition can be investigated directly. This is the reason why we have chosen to use the molecular dynamics in the present thesis to study the reconstruction phase transition of W(001) and Mo(001) surfaces.

Chapter 3

Molecular dynamics method

3.1 Introduction

The statistics of a classical system can be simulated in one of two ways, either by a Monte Carlo method or by a molecular dynamics method. The Monte Carlo method generate a Markovian chain of spatial configurations according to the rules of the Metropolis algorithm/61/. The static quantities are calculated by the ensemble average. In contrast to the Monte Carlo method the molecular dynamics simulation technique yield the motion of a given number of atoms as governed by their mutual interactions. The solution is given as trajectories of the particles in phase space. Averaging over these trajectories, the average values of dynamical variables which depend on the position and velocity of the particles can be calculated. Namely,

$$\langle \mathcal{F} \rangle_t = \lim_{\tau \to \infty} \frac{1}{\tau} \int_0^\tau \mathcal{F}\left[\vec{r}^N(t), \vec{p}^N(t)\right] dt \qquad (3.1)$$

For static quantities, the time average is identical to the ensemble average if the system is assumed to be ergodic. However, with a molecular dynamics method, not only static but also the dynamic properties of the system can be studied directly. This is one of the important advantages of molecular dynamics over the Monte Carlo method, since the Monte

Carlo method does not generate a real dynamical history of the system.

The molecular dynamics method was first used for a fluid with hard sphere interactions by Alder and Wainwright /62/, extended to liquids with continuous potentials by Rahmam /63/ and since then has been used successfully to study many other situations including plasmas, molten salts, lattice vibrations, superionic conductors, solid structural phase transition etc /64-72/. Recently, the method has also been developed to simulate the quantum systems /73,74 /. The method is emerging as a powerful technique for the study of statistical mechanics. In this chapter we will not attempt to review all the developments of the technique but outline only those relevant to the present work.

3.2 Conventional Molecular Dynamics

In a conventional molecular dynamics simulation a set of N classical particles are contained in a 'box' (MD cell) of volume V. The microscopic state of the system at a given instant is completely specified by the values of 3N coordinates $\vec{r}_i$ globally denoted by $\vec{r}^N$ and the 3N momentum $\vec{p}_i$, denoted similarly by $\vec{p}^N$. The value of the variables $\vec{r}^N$, $\vec{p}^N$ define a point in a 6N-dimensional phase space, Γ_N ; As time changes the phase point moves along a phase trajectory. If $H(\vec{r}^N, \vec{p}^N)$ is the hamiltonian of the system, the

phase point is determined by the equations of motion

$$\dot{\vec{r}}_i = \frac{\partial \mathcal{H}}{\partial \vec{p}_i} \quad , \quad \dot{\vec{p}}_i = -\frac{\partial \mathcal{H}}{\partial \vec{r}_i} \qquad (3.2)$$

where i=1,2,... ...,N. In the most studies, the particles are assumed to interact through some pairwise potential

$$V_n = \frac{1}{2} \sum_i {}' \sum_j {}' \phi(r_{ij}) \qquad (3.3)$$

where

$$r_{ij} = |\vec{r}_{ij}| = |\vec{r}_i - \vec{r}_j| \qquad (3.4)$$

Newton's equations are then given by

$$m_i \ddot{\vec{r}}_i = - \sum_{j \neq i} \frac{1}{r_{ij}} \frac{d\phi}{dr_{ij}} \vec{r}_{ij} \quad , \quad i = 1, \cdots N \qquad (3.5)$$

These N coupled equations are solved numerically by a suitable choice of algorithm. Once the positions and velocities of all the particles are known as functions of time, the average values of dynamical variables which depend on these positions and velocities are computed by time averaging

$$\langle F \rangle = M^{-1} \sum_{j=1}^{M} F(\tau_j) \qquad (3.6)$$

In the meanwhile, the correlation functions can be computed as

$$\langle F(t)F(0) \rangle = \langle F(t+\tau)F(\tau) \rangle = M^{-1} \sum_{j=1}^{M} F(t+\tau_j)F(\tau_j) \qquad (3.7)$$

here M denotes the number of MD steps used in the sums.

The temperature of the system, which plays an important role in thermodynamics, is defined as the average value of the kinetic energy of the particles and can be given as

$$T = \frac{1}{3MNmk_B} \sum_{m=1}^{M} \sum_{j=1}^{N} |\vec{P}_{mj}(t)|^2 \qquad (3.8)$$

If one wants to 'heat' or 'cool' the system in order to study the thermal behaviour of the system, a simple way is to multiply the velocity of the particles by a factor α ($\alpha>1$ for heating, $\alpha<1$ for cooling) since the temperature of the system is obtained by averaging the kinetic energy of the particles. The choice of α and the frequency with which it is applied will vary according to circumstances.

In a conventional MD simulation, the volume and shape of the MD cell is fixed and the system isolated. Since the potential energy Vn does not depend on time, the total energy E of the system is conserved. Thus the statistical ensemble generated in a conventional MD calculation is a (VEN) ensemble or microcanonical ensemble. The average of any property of the system with specified values of N, V and E is equivalent to an average over a microcanonical ensemble if the trajectories passes through all parts of phase-space that have the specified energy.

It is well known that in the thermodynamical limit, average quantities are independent of the choice of ensemble,

whereas fluctuations depend very much on the choice made. Special problems may arise when a conventional MD method is used to study systems which have a structrual phase transition /67,75-77/. In particular the fluctuations of the total energy and volume of the system which are generally associated with a phase transition may be suppressed in a conventional MD simulation. In order for these fluctuation effects to be simulated, we need to extend the method in order to allow for the simulation at constant temperature and constant pressure, i.e. the simulation of canonical or isothermal-isobatic ensembles.

3.3 Extended molecular dynamics

In order to overcome the above difficults associated with conventional MD simulation, various extended MD methods have been successively developed /75-86/ to enable one to simulate the system under constant temperature and constant pressure conditions. In what follows, we will describe briefly the methods which have been employed in the present work.

A). MD simulation at constant pressure - Andersen-Parrinello-Rahman method

A structural phase transition is generally associated with the change of volume and shape of the unit cell. The average volume is determined by the balance between the

internal pressure and the externally set pressure. The idea of MD simulations at constant pressure is then to let the volume of the MD cell becomes a variable and allow it to fluctuate. This idea was originaly introduced by Andersen /75/ and subsequently extented by Parrinello and Rahman to allow for changes of not only the volume of the MD cell but also its shape /76,77/ (the so called new MD method).

In the new MD, the MD cell can have an arbitrary shape and volume completely described by three vectors $\vec{a}$, $\vec{b}$, and $\vec{c}$ that span the edges of the MD cell. The vector $\vec{a}$, $\vec{b}$ and $\vec{c}$ can have different lengths and arbitrary mutual orientations. An alternative description is obtained by arranging the vectors ($\vec{a},\vec{b},\vec{c}$) to form a 3x3 matrix whose columns are the components of $\vec{a}$, $\vec{b}$ and $\vec{c}$ respectively. The volume is given by

$$V = \| \vec{h} \| = \vec{a} \cdot (\vec{b} \times \vec{c}) \qquad (3.9)$$

The position $\vec{r}_i$ of particle i can be written in terms of $\vec{h}$ and of a column vector $\vec{s}_i$, with components ξ_i, η_i and ζ_i as

$$\vec{r}_i = \vec{h}\,\vec{s}_i = \xi_i \vec{a} + \eta_i \vec{b} + \zeta_i \vec{c} \qquad (3.10)$$

Where $0 < \xi_i, \eta_i, \zeta_i < 1$. In fact, we can think of ξ_i, η_i, ζ_i as the coordinates of the ith particle in a scaled MD cell. The images of si are at $\vec{s}_i + (\lambda, \mu, \nu)$ where λ, μ, ν are integers from $-\infty$ to $+\infty$. The square of the distance

between i and j is given by

$$r_{ij}^2 = (\vec{s}_i - \vec{s}_j)^{\sim} \vec{\vec{G}} (\vec{s}_i - \vec{s}_j) \qquad (3.11)$$

Where

$$\vec{\vec{G}} = \vec{\vec{h}}^{\sim} \vec{\vec{h}}$$

The reciprocal space is spanned by the vectors $\frac{2\pi}{V}$(bxc, cxa, axb)= $\frac{2\pi}{V}\vec{\vec{\sigma}}$. The matrix $\vec{\vec{\sigma}} = V(\vec{\vec{h}}^{\sim})^{-1}$ carries information concerning the size and orientation of the MD cell.

In the case where only hydrostatic pressure is applied, the 3N dynamical variables that describe the positions of the N particles were augmented by the nine components of $\vec{\vec{h}}$. The time evolution of the 3N+9 variables was then obtained from the Lagrangian

$$\mathcal{L} = \frac{1}{2}\sum_{i=1}^{N} m_i \dot{\vec{s}}_i^{\sim} \vec{\vec{G}} \dot{\vec{s}}_i - \sum_{i=1}^{N}\sum_{j>i}^{N} \Phi(r_{ij}) + \frac{1}{2} W \mathrm{Tr}\, \dot{\vec{\vec{h}}}^{\sim} \dot{\vec{\vec{h}}} - PV \qquad (3.12)$$

Where P denotes the externally applied hydrostatic pressure, $\Phi(r)$ the pair potential. The kinetic term associated with the time variation of $\vec{\vec{h}}$ has a constant of proportionality w which has the dimension of mass. As has been pointed out by Parrinello and Rahman, the Lagrangian (3.12) will generate an isoenthalpic-isobaric ensemble, apart from a small correction arising from the $1/2w\dot{\vec{\vec{h}}}^2$ term.

From (3.12) the Lagrangian equations of motion are

easily written down

$$\ddot{\vec{S}} = -\sum_{j\neq i} m_i^{-1} \left(\frac{\Phi'}{r_{ij}}\right)(\vec{S}_i - \vec{S}_j) - \vec{\vec{G}}^{-1}\dot{\vec{G}}\,\dot{\vec{S}}_i \qquad i = 1, \cdots N \qquad (3.13)$$

$$W\ddot{\vec{h}} = (\vec{\vec{\Pi}} - p)\vec{\sigma} \qquad (3.14)$$

where, using the usual dyadic notation $\vec{V}_i = \vec{h}\,\dot{\vec{S}}_i$

$$V\vec{\vec{\Pi}} = \sum_i m_i \vec{V}_i \vec{V}_i - \sum_i \sum_{j>i} \left(\Phi'/r_{ij}\right)\vec{r}_{ij}\,\vec{r}_{ij} \qquad (3.15)$$

Note that for the special case of $\vec{h}$=constant, i.e., when the MD cell is fixed in volume and shape, $\dot{\vec{G}}$=0 and due to e.q.(3.10), e.q.(3.13) become identical to e.q.(3.5) thus the formula described above reduce to the standard MD by simply setting h=constant.

B). MD simulation at constant temperature

In order to simulate a canonical ensemble, we need some procedure to simulate the effects of a heatbath such that the Boltzman distribution $e^{-\beta\mathcal{H}}$ is ensured.

One such procedures has been proposed by Andersen /75/ where stochastic collisions from a heatbath are required for thermostating. Each stochastic collision is an instantaneous event that affects the momentum of one particle. The collisions suffered by a particle occur in accord with a stochastic process and the times at which different particles suffer collisions are statistically uncorrelated. Between

stochastic collisions, the state of the system evolves in accordance with the equations of motion.

Andersen's method is given by the following procedure. An initial set of positions and momenta are chosen, and Hamilton's equations of motion are integrated over some small time interval τ . Random numbers are used to decide which particles are to suffer stochastic collisions at the end of this time interval, the mean number being equal to $N\nu$, where ν is the mean rate at which each particle is assumed to suffer stochastic collisions. If particle i suffers a collision, the value of the momentum of particle i after the collision is chosen at random from a Boltzmann distribution at temperature T. The momentum change takes place instantaneously, and all other particles are unaffected by the collision. This is done for all chosen particles. Then Hamilton's equations for the entire collection of N particles are integrated until the next stochastic collision process. This procedure is repeated. In what follows we refer to this method of temperature control as canonical-temperature control. As has been pointed out by Andersen /75/, the results of this constant temperature MD procedure is a set of trajectories, specified by $\vec{r}_i(t)$ and $\vec{p}_i(t)$ for the N particles in a volume V with periodic boundary conditions and the average of any function $F(\vec{r}_i, \vec{p}_i, V)$

over their trajectories is equal to the ensemble average of F for the canonical ensemble in which the temperature is T.

Another method for performing the constant temperature MD simulation has been subsequently developed by Nose /78,79/. By the introduction of an additional degree of freedom through mass scaling, the total energy of the physical system is allowed to fluctuate. The additional degree of freedom s acts as an external system for the physical system, by an appropriate choice of potential (3N+1)kTlns for the variable S, the hamiltonian for the three-dimensional monoatomic system of N particles reads

$$\mathcal{H}_N = \sum_{i=1}^{N} \frac{\vec{p}_i^{\,2}}{2m_i s^2} + \Phi(\vec{r}_1 \cdots \vec{r}_N) + \frac{p_s^2}{2\alpha} + \frac{(3N+1)}{\beta} \ln s \qquad (3.16)$$

The first two terms are the ordinary hamiltonian of a system of N particles of masses mi, momenta pi, interacting via a potential Φ(r1,... ..., rN). The last two terms are the kinetic energy and potential energy associated with the new variables. As Nose has shown/78,79/, the average of a physical quantity over the trajectories generated by this hamiltonian are equivalent to a canonical average at temperature T.

Nose's method is purely dynamical and deterministic. This method gives the rigorous canonical distribution both in momentum and in coordinate space. However, when the

method is used to simulate a system at low temperature, it will probably cause some trouble as the system tends to equilibrium, namely the system may trap itself in a particular vibrational mode because at low temperature the system is mainly governed by the harmonic part of potential. On the other hand, in the Andersen's method, the stochastic procedure breaks the harmonicity and drives the system to equilibrium. In the present work most of the MD slab simulations for the W(001) surface will be performed at rather low temperatures, i.e. 50K to 500K, which are very low compare to the melting temperature 3500K the bulk Tungsten. Although in our system the surface is very anharmonic, the bulk is, however, rather harmonic. For the reason discussed above , we have chosen to adopt the stochastic method of Andersen.

3.4 The algorithm

In order to solve Newton's equations (3.15) numerically, we have to convert the differential equations into a set of difference equations which enable us to go from time t to $t+\Delta t$ with a suitable choice of Δt.

The simplest algorithm is that used by Verlet /88/ and his collaborators. Using q(t) to represent any one of the 3N coordinates which describe the system completely, we have

$$q(t+\Delta t) = q(t) + \Delta t\dot{q}(t) + \frac{1}{2}(\Delta t)^2\ddot{q}(t) + \cdots$$
$$q(t-\Delta t) = q(t) - \Delta t\dot{q}(t) + \frac{1}{2}(\Delta t)^2\ddot{q}(t) + \cdots \qquad (3.17)$$

Therefore

$$q_i(t+\Delta t) = 2q_i(t) - q_i(t-\Delta t) + (\Delta t)^2 \frac{1}{m} \sum_{j \neq i} F_{ij}(t) + O(\Delta t)^4 \qquad (3.18)$$

where Fij(t) is the force exerted by particle j on particle i at time t. The error introduced is of order $(\Delta t)^4$. If we subtract the two expansions in (3.17) we find that the velocity of particle i at time t can be calculated from

$$\dot{q}_i(t) \approx \frac{1}{2\Delta t}[q_i(t+\Delta t) - q_i(t-\Delta t)] \qquad (3.19)$$

The error is of the order $(\Delta t)^3$, but the velocities play no part in the integration of the equation of motion.

An alternative algorithm is a predictor-corrector type developed by Rahman and Gear /88,89/. This algorithm makes use of the derivatives of q up to a predetermined order, say five, for example. Let us denote q by q_0, $q\Delta t$ by q_1, $q(\Delta t)^2/2!$ by q_2 and so on. By using a Tayler expansion it is possible to predict the values of all the derivatives of the positions at $t+\Delta t$. Denoting the predicted values of q_i by P_i, one obtains

$$\begin{aligned}
P_0 &= q_0 + q_1 + q_2 + q_3 + q_4 + q_5 \\
P_1 &= q_1 + 2q_2 + 3q_3 + 4q_4 + 5q_5 \\
P_2 &= q_2 + 3q_3 + 6q_4 + 10q_5 \\
P_3 &= q_3 + 4q_4 + 10q_5 \\
P_4 &= q_4 + 5q_5 \\
P_5 &= q_5
\end{aligned} \qquad 3.20$$

Hence from P_2 we can get the predicted value of the acceleration at $t+\Delta t$. Using P_0, which are the predicted positions at $t+\Delta t$ the accelerations in predicted positions can be calculated using the equation of motion. Let $a(P_0)$ denote these accelerations and $\tilde{P}_2$ denote $a(P_0)(\Delta t)^2/2!$, the difference $D=\tilde{P}_2-P_2$ allows us to get corrected values C_i from the predicted values P_i as follows

$$C_i = P_i + f_{i2}^{(5)} D \qquad i=0, 1, 2, 3, 4, 5 \qquad (3.21)$$

Where the numbers $f_{i2}^{(5)}$ are 3/16, 251/360, 11/18, 1/6, 1/60 respectively for i=0, 1, 2, 3, 4, 5.

The predictor-corrector method has the advantage that one can use the differences C_0-P_0 and C_1-P_1 to put bounds on the acceptable error. The predictor-corrector loop can be repeated if necessary by using the corrected values as the predicted values and going back to the calculation of $a(C_0)$ and then Δ becomes $\tilde{C}_2-C_2$, $\tilde{C}_2$ being $a(C_0)\times(\Delta t)^2/2!$.

3.5 Periodic boundary condition

Due to the limitation of present computer memory space. The number of particles N in the MD simulation is restricted to $10^3 \sim 10^6$ and for small systems surface effects are obviously very important. In order to minimize the surface effects and to simulate more closely the properties of an infinite system, a periodic boundary condition is almost invariably imposed. The way in which this boundary condition

works in a two-dimensional system is illustrated in Fig.3.1. The particles of interest lie in the central cell and this basic unit is surrounded on all sides by periodically repeating replicas of itself. Each image cell contains N particles in the same relative positions. When a particle enters or leaves through one face of the basic cell the move is balanced by an image of that particle leaving or entering a neighbouring cell through the opposite face.

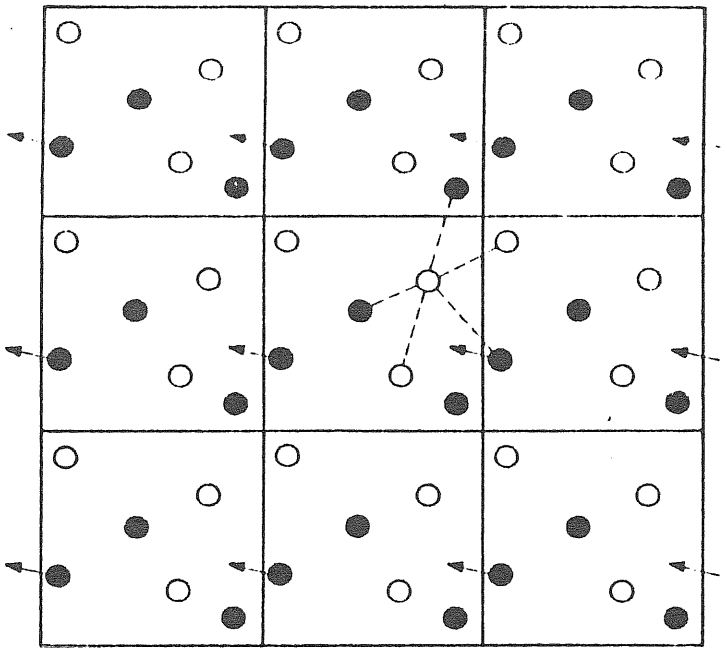

Fig.3.1 Periodic boundary conditions used in computer experiments.

In many cases, small systems with periodic boundary conditions are a good approximation to the macroscopic system. Some problems may arise for critical phenomena because the large-scale fluctuations which characterize the critical region are suppressed by the use of periodic boundary conditions. However, one still can learn a lot of information concerning the phase transition from the computer simulation on a finite size sample with periodic boundary condition provide the size of the sample is appropriate chosen. The critical behaviour can also be studied quite accurately by the computer simulation once the finite size scaling technique is used/58/.

Chapter 4

Choice of potentials for W

4.1 Introduction

In chapter 1 we have introduced the effective lattice hamiltonian developed by Fasolino, Santoro and Tosatti /39/, namely

$$\mathcal{H} = \sum_{\ell} \frac{P_\ell^2}{2m} + \frac{1}{2} \sum_{(ij) \neq \langle ij \rangle} V^B(|\vec{R}_i - \vec{R}_j|) + \frac{1}{2} \sum_{\langle ij \rangle} V^S(|\vec{R}_i - \vec{R}_j|) \qquad (4.1)$$

$\langle ij \rangle$ = 1st surface neighbors

with

$$V^B(R) = V_1(R) + V_2(R)$$

$$V_1(R) = V_{10} + R_1^{0^2}\left[\alpha_1\left(\frac{R}{R_1^0} - 1\right) + \frac{1}{2!}\beta_1\left(\frac{R}{R_1^0} - 1\right)^2 + \frac{1}{3!}\gamma_1\left(\frac{R}{R_1^0} - 1\right)^3 + \frac{1}{4!}\delta_1\left(\frac{R}{R_1^0} - 1\right)^4\right]$$

$$V_2(R) = V_{20} + R_2^{0^2}\left[\alpha_2\left(\frac{R}{R_1^0} - 1\right) + \frac{1}{2!}\beta_2\left(\frac{R}{R_2^0} - 1\right)^2 + \frac{1}{3!}\gamma_2\left(\frac{R}{R_2^0} - 1\right)^3 + \frac{1}{4!}\delta_2\left(\frac{R}{R_2^0} - 1\right)^4\right] \qquad (4.2)$$

and

$$V_S(R) = V_{S0} + R_S^{0^2}\left[\alpha_S\left(\frac{R}{R_S^0} - 1\right) + \frac{1}{2}\beta_S\left(\frac{R}{R_S^0} - 1\right)^2 + \frac{1}{3!}\gamma_S\left(\frac{R}{R_S^0} - 1\right)^3 + \frac{1}{4!}\delta_S\left(\frac{R}{R_S^0} - 1\right)^4\right]$$

In the present work this Hamiltonian is used for a realistic study of the temperature dependent reconstruction phase transitions of the W(001) and Mo(001) surfaces by a molecular dynamics simulation. We need to know $V^B(R)$ and $V^S(R)$ over a wide range of R, not just near equilibrium as in the lattice dynamical calculations /39,43/. It is obviously not trivial to construct a set of satisfactory poten-

tials $V^B(R)$ and $V^S(R)$, because there are many parameters in the hamiltonian to be optimized. Since a first principle calculation of those parameters in (4.2) is not yet available, we have to choose them empirically through many tests.

4.2 The bulk potential

The bulk potential is supposed to describe the lattice properties of the bulk W as required by the model. This means that our constructed potential should be able to reproduce the known bulk properties, both harmonic and anharmonic, as much as possible. Based on this requirement, several properties have been particularly considered in the choice of bulk potential parameters as we now outline.

1). The set of harmonic parameters α_1, β_1, α_2 and β_2 satisfy $\alpha_1 = -\alpha_2$ and are taken $\alpha_1 = -0.03$ eV/Å^2, $\beta_1 = 4.60$ eV/Å^2, $\beta_2 = 3.29$ eV/Å^2 from the bulk phonon fitting of Castiel et al. /90/, which reproduces well the experimental bulk phonon spectrum as shown in Fig.4.1.

2). The anharmonic parameters γ_1, γ_2 have been determined by Fasolino and Tosatti /43/, fitting the linear thermal expansion coefficient $\alpha = 3.76\ 10^{-6} K^{-1}$ and the linear temperature coefficient of the C_{44} elastic constant $\Lambda_{44} = -0.644 \times 10^{-4} K^{-1}$ /91/. Given an average potential energy per atom U(a) for a local lattice parameter a, they found that a crude but simple way to evaluate the thermal expansion coefficient

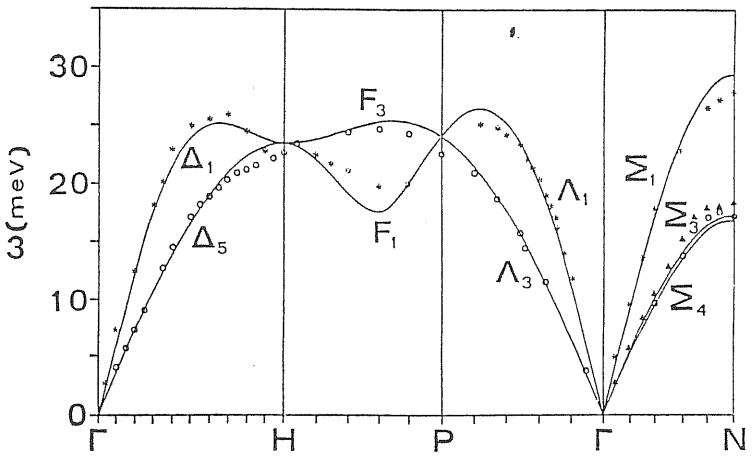

Fig.4.1 Bulk phonon spectrum of tungsten as obtained by the phonon fitting of Ref.90. Experimental points are taken from B.N.Brockhouse in 'Phonons in perfect lattices and lattices with point imperfections' ed. R.W.H.Stevenson, p.110, Oliver & Boyd, Edinburgh and London, 1966.

is the Einstein average

$$\langle a - a_0 \rangle = \frac{\int_{-\infty}^{\infty} (a-a_0) \exp\left[-\left(U(a) - U(a_0)\right)/k_B T\right] da}{\int_{-\infty}^{\infty} \exp\left[-\left(U(a) - U(a_0)\right)/k_B T\right] da} \simeq a_0 \alpha T \qquad (4.3)$$

Since $U(a) = 1/2\,(8\,V_1(R = a/\sqrt{2}) + 6\,V_2(R = a))$, we obtain, by inserting for $V_1(R)$ and $V_2(R)$ the form (4.2)

$$\frac{\alpha}{k_B} = -\frac{(\gamma_1 + \gamma_2)}{6\,a_0^2\,(\beta_1 + \beta_2)^2} \qquad (4.4)$$

In the quasi-harmonic approximation the elastic constant change is obtained simply by recalculating C_{44} at $a=a(1+\alpha T)$

$$\Lambda_{44} = \alpha \left[\frac{-1+\beta_2-\alpha_2+\gamma_1/3+2(\beta_1-\alpha_1)/3}{\alpha_2+(\beta_1+2\alpha_1)/3} \right] \qquad (4.5)$$

giving $\gamma_1=-94.3$ eV/Å^2, $\gamma_2=-79.0$ eV/Å^2.

3). Since distortions at the surface are generally not small, we need to specify also bulk fourth order anharmonicities δ_1 and δ_2 as in E.q (4.2). Although we could in principle try to determine δ_1, δ_2 e.g. from the quadratic temperature coefficient of thermal expansion and elastic constants, in practice it was found to be handier and safer to determine them by a molecular dynamics run of bulk potential as specified by E.q(4.2). As it turns out, the expansion curve is very dependent upon the choice of δ_1 and δ_2 already at relative low temperatures (see Fig.4.2). The best values yielding a reasonable low-temperature expansion as on Fig.4.3 turned out to be $\delta_1=3.0\times10^3$ eV/Å^2, $\delta_2=1.5\times10^3$ eV/Å^2.

We note that these parameters cannot fit the experimental thermal expansion at temperature higher than 2000K. This is because the tail of our potentials $V_1(R)$ and $V_2(R)$ (see Fig.4.5 in the following) are too steep at large R. In order

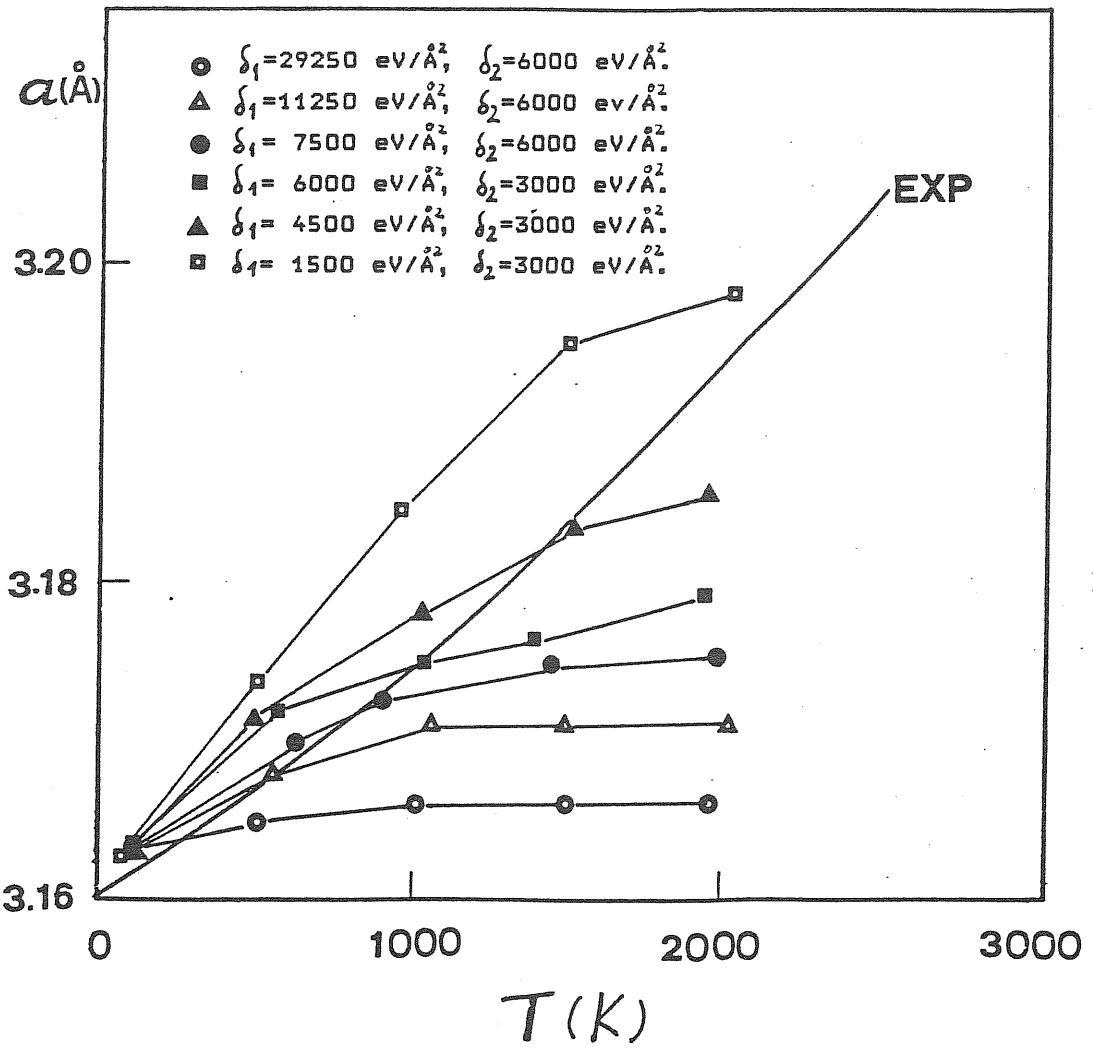

Fig.4.2 MD results of tungsten lattice thermal expansion by various choice of fourth anharmonic force constants δ_1 and δ_2 .

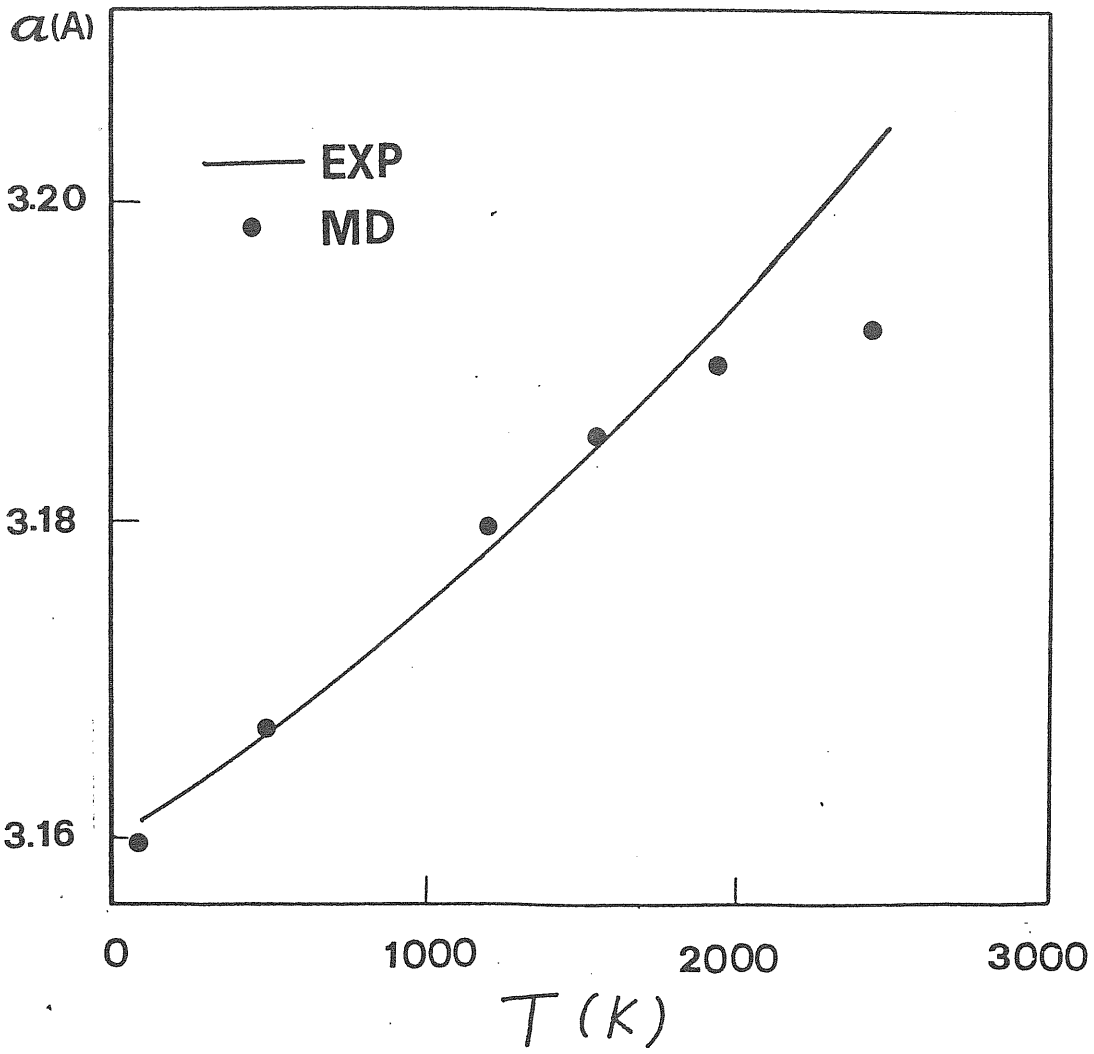

Fig.4.3 Comparison of experimental thermal expansion of the bulk W (Ref.91) with MD results obtained with the bulk potential described in section 2 (and will show in Fig.4.5).

to improve the situation, higher order terms would have to be included in the expansion of E.q.(4.2). This, however, would require the introduction of more free parameters. Since the present work aims at a study of the surface reconstruction phase transitions where the interesting temperatures are $0 < T < 1000$ K, we believe the expansion terminated to the fourth order is sufficient for the present purpose.

4). The potential strength is described by the parameters V_{1o} and V_{2o}. First of all, these two parameters should be chosen to fit the cohesive energy of the bulk tungsten. That is,

$$E_C = \frac{1}{2N} \sum_{(\vec{R}^o \vec{R}'^o)} V^B(|\vec{R}^o - \vec{R}'^o|) = \frac{1}{2}(6V_{1o} + 8V_{2o}) = 8.66\ eV \quad (4.6)$$

where $\vec{R}^o$ and $\vec{R}'^o$ are the equilibrium positions of the W atoms at T=0, 6 and 8 are the number of the nearest and next-nearest neighbours of the bcc lattice, 8.66 eV is the cohesive energy (per atom) of bcc tungsten. By the bulk MD simulation, it was found that the relative values of V_{1o} and V_{2o} are very critical in the determination of the crystal structures (bcc or fcc). In order to obtain a stable bcc structure, the optimal choice of V_{1o} and V_{2o} is found to be $V_{1o} = -1.2545$eV, $V_{2o} = -1.2139$eV /92/.

5). For a given set of parameters, there are still some arbitrariness left in the choice of the form of the potential. One may, for example, construct a potential as that shown in Fig.4.4a, in which $V_1(R)$ and $V_2(R)$ are smoothly joined, given a certain energy barrier between first and second neighbour distance. One also can, on the other hand, construct a bulk potential like the one shown in Fig.4.4b, there the first neighbour interaction $V_1(R)$ and the second

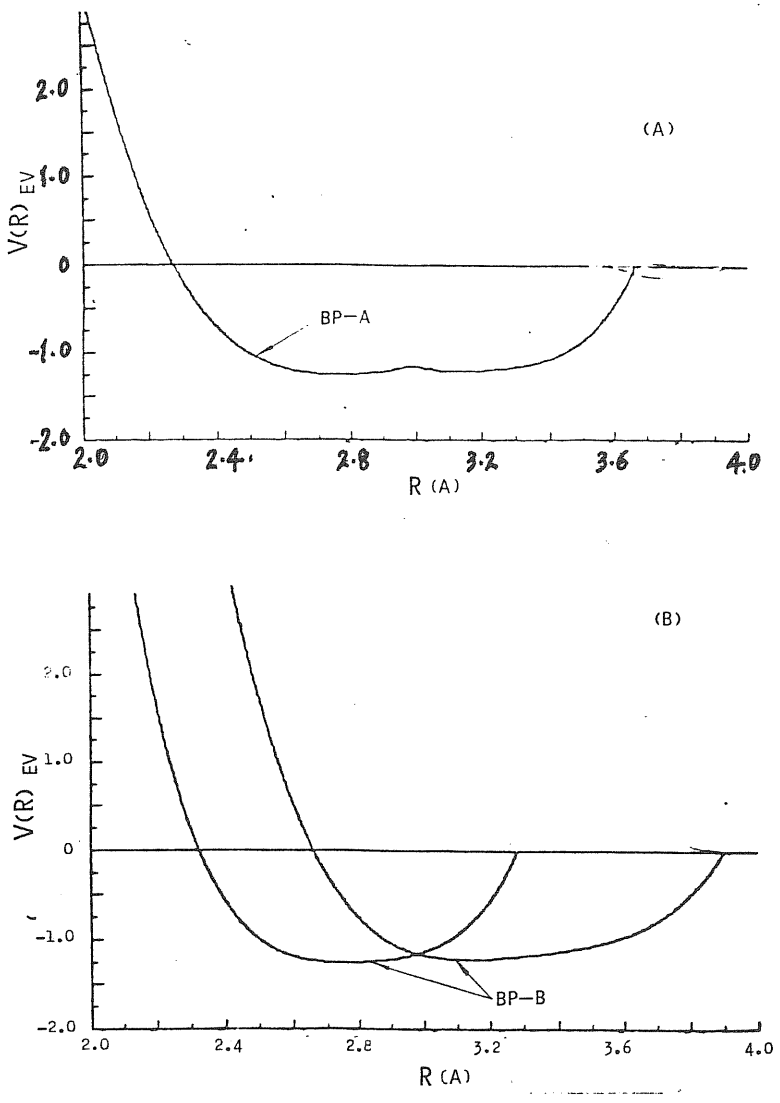

Fig.4.4 The two possible form of the bulk potentials.

neighbour interaction $V_2(R)$ are independent. If at T=0 two atoms are nearest neighbour, they will always interact through $V_1(R)$, while if they are second neighbours, they will interact via $V_2(R)$ at any time and temperature.

If we are going to simulate a bulk solid, these two choices would be equivalent as long as the system is far from melting, since then the atoms do not move very far from their original equilibrium positions. However, if the potential is used for a slab MD simulation, some spurious effects may arise from potential of the kind 4.4a, particularly due to the existence of surfaces. We found that by using the potential 4.4a in a slab MD simulation, the surface layer atoms tend to escape from their first neighbour distance toward next-nearest neighbour positions for two reasons. Firstly, since the bulk potential is very asymmetric (due to the strong anharmonicity) with a rather steep repulsive core and a relative flat tail, the atoms are likely to relax to a large distance. Secondly, once a surface atom fluctuates beyond a certain distance Rm with respect to its first neighbours, it will then continuously fall into the second neighbour well because there is no balancing force on the other side of a surface to push it back. In order to eliminate this undesired effects (since we require the bulk potential to keep well a bulk structure,

even when it is used in a slab calculation), a higher energy barrier is required if one insists on using this form of potential. However, experimental data on thermal expansion and phonon spectrum impose several restrictions on the choice of the parameters and it is impossible to introduce a sufficiently high energy barrier. On the other hand, such a difficulty can be automatically solved once a potential in the form of Fig.4.4b is used. From a chemical bond point of view, this kind of potential provides a suitable representation for the bonds between first neighbour atoms and second neighbour atoms respectively. Since we are going to perform the MD simulation in a slab, it is necessary to adopt the bulk potential in the form of Fig.4.4b.

The bulk potential $V^B(R)$ thus constructed is shown in Fig.4.5, which corresponds to the parameters determined above and summarized again as following

V_{10} =-1.2545 eV, α_1 =-0.03 eV/Å^2, β_1=4.60 ev/Å^2,

γ_1 =-93.3 eV/Å^2, δ_1=3010.0 eV/Å^2;

V_{20} =-1.2139 eV, α_2=0.03 eV/Å^2, β_2=3.29 ev/Å^2,

γ_2 =-79.6 eV/Å^2, δ_2=1510.0 eV/Å^2;

As we have pointed out before, this potential reproduces well the experimental bulk phonon spectrum (see Fig.4.1), and predicts correct thermal expansion behaviour compared to

experiments (Fig.4.2). Moreover, this bulk potential can also ensure a stable bcc structure. The bulk structure has been tested by the new MD method of Parrinello and Rahman /76,77/. We started with initial configuration of the bcc crystal of W. The possible structural transformation is not inhibited by the new MD method. However, as indicated by the pair correlation function of Fig.4.6, the system retains a very stable bcc structure.

We can thus conclude that the bulk potential we have constructed is an optimized representation of the effective interactions between the bulk W atoms. This bulk potential will be kept unchanged throughout our calculations for W systems.

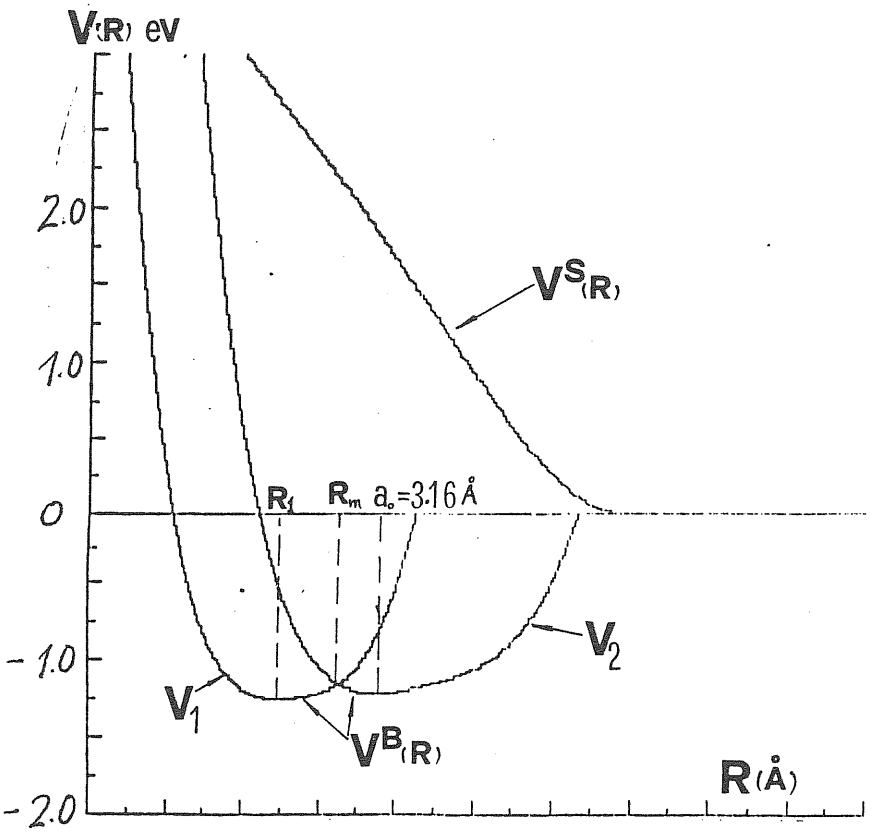

Fig.4.5 The optimized bulk and surface potentials used for the study of W(001) surface reconstruction.

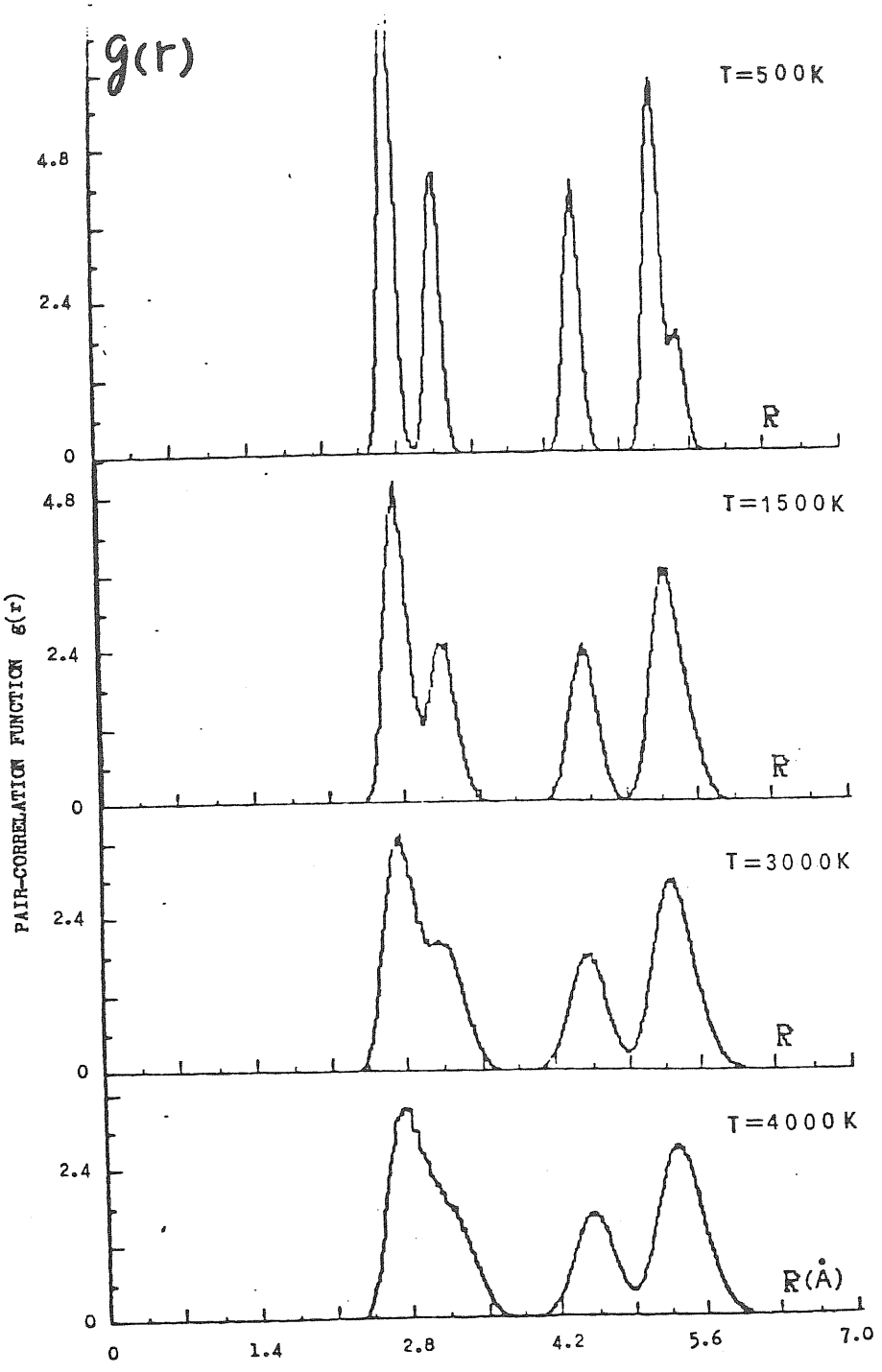

Fig.4.6 MD results of pair-correlation function of bulk tungsten obtained with the bulk potential of Fig.4.5.

4.3 The surface potential

The surface potential $V^S(R)$ for W(001) surface is also constructed in an empirical way as we have done for the bulk potential. However, in the case of the surface, much less experimental data about cohesive energy, phonon spectrum and lattice thermal expansion as in the case of bulk, are available and can be used in order to determine the potential parameters. The only experimental informations for judging the constructed surface potential are the surface structure, the amplitude of the reconstruction distortion and the corresponding phase transition temperature. On the other hand, much useful information concerning the surface potential, especially the harmonic force constants can be learned from the lattice dynamical calculation of Fasolino et al/39,43/. Although the Fasolino's calculation cannot tell us the optimal surface force constants, it does provide us with an useful guide in the choice of those parameters, particularly because the harmonic force constants α_S, β_S chosen from M5 region of Fig.1.19 will destabilize the (1x1) surface and lead to a c(2x2) distortion. Practically, we first choose a set of α_S, β_S from M5 region of Fig.1.19, then the corresponding anharmonic force constants γ_S, δ_S, which act to terminate the distortion, are adjusted in order to give an equilibrium distortion amplitude ρ_0=0.2 Å accord-

ing to the experimental estimation and a $c(2x2)_{<11>}$ distortion. This set of parameters should also ensure a reasonable amount of energy gain ΔE for the reconstructed structure at T=0. Having this set of force constants the surface potential $V^S(R)$ is constructed according to (4.2) provided the potential strength V_{S0} is suitable chosen. Then the potential, together with the bulk potential of Fig.4.5 are plugged into the hamiltonian (4.1) and tested by an n-layer slab MD simulation. The procedure is repeated until the set of optimized parameters are obtained. By this we mean that the constructed potentials have to be able to give a correct $c(2x2)_{<11>}$ reconstructed structure as that of Fig.1.4 and a correct transition temperature compared to experiment. A set of optimized parameters obtained in this way is α_S=-0.75eV/Å^2 , β_S=-0.94eV/Å^2 , γ_S=3.76eV/Å^2 , δ_S=225.0eV/Å^2 , V_{S0}=1.7579eV. The corresponding potential is also shown in Fig.4.5, labeled by $V^S(R)$. Fig.4.7 shows the T=0 energy gain of c(2x2), reconstructed structure, with various distortion amplitude with respect to the (1x1) surface, obtained by using this set of optimized potentials. The maximun energy gain is found to be at ρ_0= 0.23 Å, which is within the range of values estimated by the experiment. The energy gain at this distortion is 31 mev per surface atom. From Fig.4.7 we also see that the <11> distortion is ener-

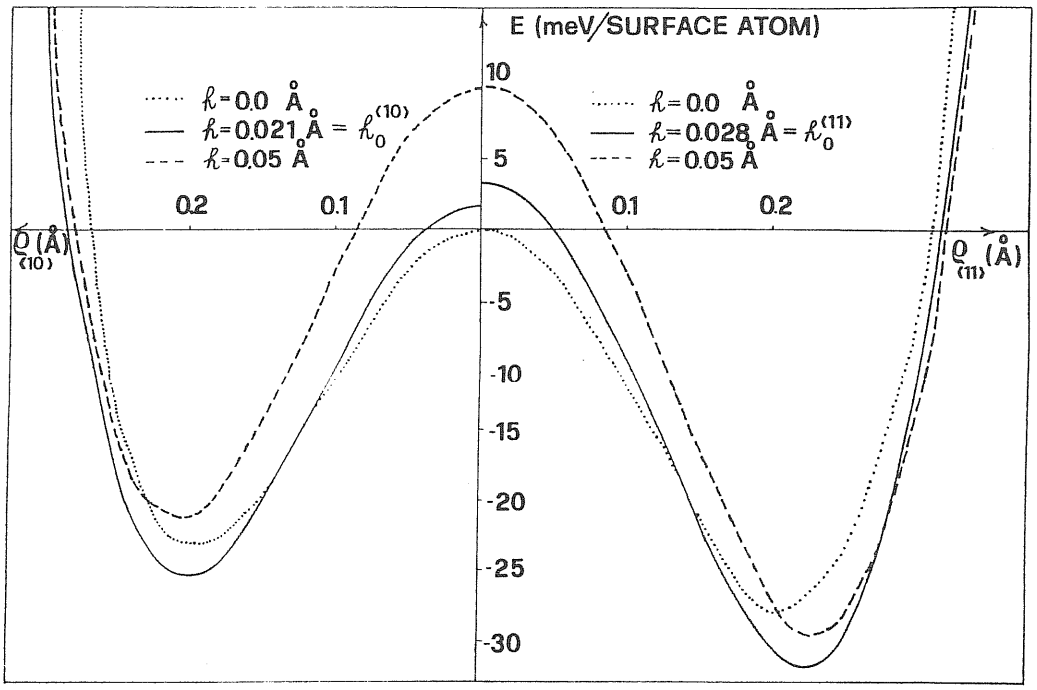

Fig.4.7 Distortion energy as a function of the c(2x2) distortion magnitude along <110> and <100>, where h is the surface relaxation.

getically favoured with respect to the <10> distortion by the constructed potentials as required.

Note that in our construction the parameter V_{s_0} has been adjusted in such a way that the minimum value of the surface potential is zero and the truncation has been made at the minimum point to give a total positive surface potential $V^S(R)$. Through the MD simulation, we have found that with an attractive surface potential well of Fig.4.8(inset), the surface atoms tend to fall into the well and the C(2x2) reconstruction structure is damaged as one sees from the surface pair-correlation function of Fig.4.8.

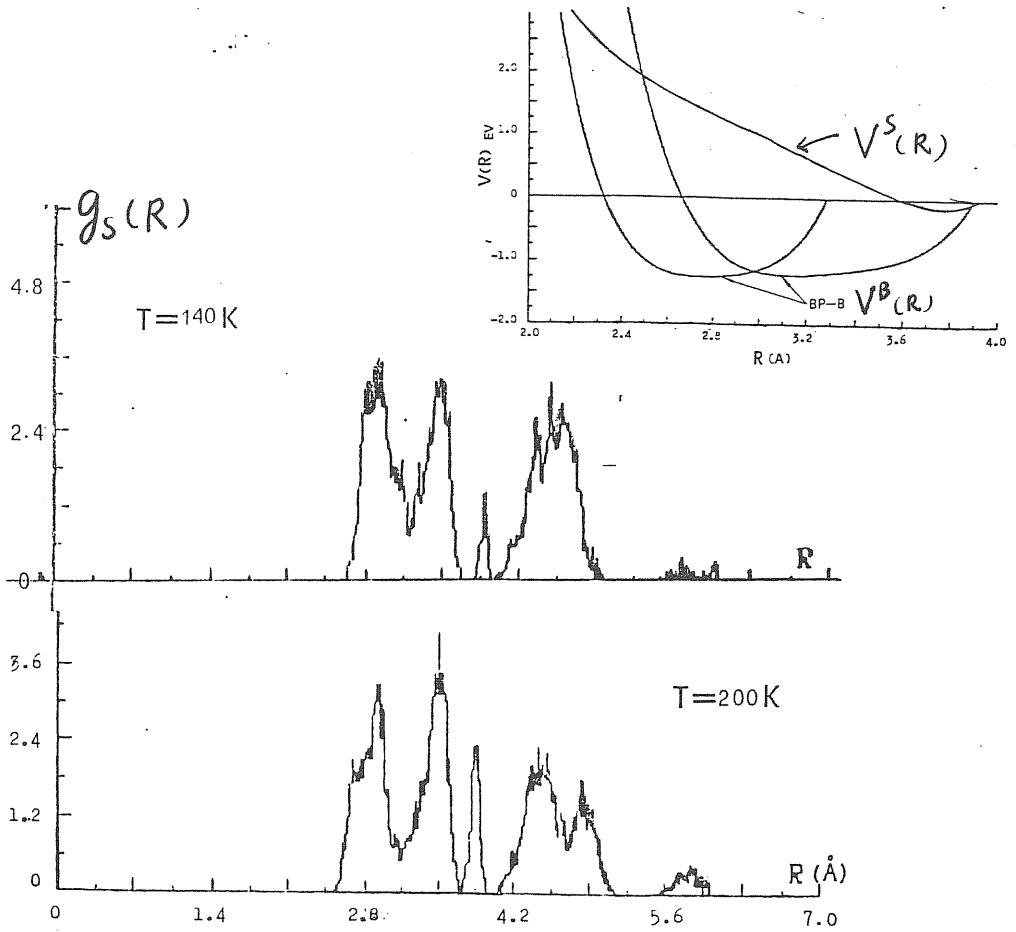

Fig.4.8 The pair-correlation function of the surface layer by using the surface potential as shown in inset.

Chapter 5

MD Results of W(001) Surface Reconstruction Phase Transition

5.1 Introduction

In order to provide a quantitative description for the W(001) surface reconstruction phase transition, we have carried out an extensive molecular dynamics simulation study based on the effective lattice hamiltonian(4.1) and the potentials developed in chapter 4. The purpose of this study is, 1). Study the temperature behaviour of the surface reconstruction and hence the nature of this displacive phase transition. 2). Characterize the lattice distortion ,i.e., the atomic structure for various phases. 3). Study the thermodynamics of this phase transition.

This chapter is arranged as following, in section 5.2 the molecular dynamics simulation procedure used in the present study is briefly summarized. Section 5.3 presents the MD results concerning the temperature behaviour of the order parameters of the reconstructed W(001) surface. Then, section 5.4 is followed to discuss the nature of the intermediate phases found in section 5.3. The surface atomic structure and some thermodynamical properties of the reconstruction are given in section 5.5 and section 5.6. Finally, a summary discussion is given in section 5.7.

5.2 MD simulation procedure

The MD simulation was performed at constant temperature, constant volume and on bcc slabs of various sizes, shapes and thicknesses with periodic (x,y) boundary conditions. A thickness of only six layers was found to be sufficient, once a bulk-like termination for the lower surface is provided. The number n of atoms per layer was varied from n=128 to 288, for a(roughly) square box oriented along <110>, and from n=64 to 256 for a square box oriented along <100>.

We start the simulation with a $c(2x2)_{<11>}$ reconstructed surface and approach the transition from the low temperature side. (However, it has been checked that the final results are independent of initial configurations as we will show in the following). A small random displacement of the particles from the initial positions and zero velocities provided the conditions for the ensuing dynamics. With the time step $\Delta t=3x10^{-15}$ sec., the fifth order predictor-corrector algorithm was used to integrate the equations of motion. The canonical temperature control method described in chapter 3 was used to perform the simulation at constant temperature. The MD cell was fixed at given temperature but it was allowed to expand according to the thermal expansion data given by the bulk potential (see Fig.4.5) when the temperature is varied. A typical cycle at each temperature con-

sisted of at least 4000 equilibration time steps followed by between 4000 and 10000 steps for useful averaging.

The MD results presented in this chapter refer to a <110> box with n=288, using the potentials of Fig.4.5. The results of the other choice of surface potential and size will be discussed in the following chapter.

5.3 Temperature behaviour of the order parameters

As we have discussed in chapter 1, the order parameter for describing the W(001) surface reconstruction phase transition is in a two-dimensional form $\rho e^{i\varphi}=(u_1,u_2)$ with ρ the distortion magnitude and φ the distortion phase relative to the <110> direction.

Another useful quantity concerning the order parameter is the surface static structure factor S(kx,ky) with Kx=1/2 Ky=$\pm$1/2, which can be directly compared with surface diffraction intensities and is defined as

$$S(k_x,k_y)=\frac{1}{n^2}\left|\sum_l \exp[i(k_x x_l+k_y y_l)]\right|^2 \qquad (5.1)$$

where l runs over all n surface atoms.

In Fig.5.1, the MD results of temperature dependence of the W(001) surface reconstruction phase transition are presented. There the static surface structure factor S(Kx,Ky) is shown for Kx=1/2, Ky=$\pm$1/2. $\langle\rho\rangle$ and $\langle\cos\varphi\rangle$ are

the staggered averages of the distortion amplitude ρ and of the phase $\cos\varphi$ over the surface atoms, i.e.,

$$\langle \rho \rangle = \frac{1}{n} \sum_{l=1}^{n} \rho_l \cos(\vec{K}_0 \cdot \vec{R}_l^0)$$

$$\langle \cos\varphi \rangle = \frac{1}{n} \sum_{l=1}^{n} \cos\varphi_l \cdot \cos(\vec{K}_0 \cdot \vec{R}_l^0) \qquad (5.2)$$

where $\vec{K}_0 = 2\pi/a(1/2,1/2)$ is the two dimensional wave vector characterizing the reconstructed surface of W(001). $\vec{R}_l^0$ denotes the unperturbed position of atom l on the surface. Hence $\cos(\vec{k}_0 \cdot \vec{R}_l^0)$ alternates between -1 and +1 for neighbouring sites.

Coursely, one sees in our theory as in experiments a change from the low temperature c(2x2) structure, where $S(1/2,1/2) \neq 0$ $S(1/2,-1/2) \approx 0$ to a high-temperature disordered state where $S(1/2,1/2) = S(1/2,-1/2) \approx 0$. The transition is found to occur through loss of phase coherence, as signalled by the decline of $\langle \cos\varphi \rangle$ in the same figure. The order parameter magnitude $\langle \rho \rangle$ shows only a modest decrease. Stronger and clearer evidence of this point is found by examining the phase and magnitude susceptibilities

$$\chi_\varphi = \left[\langle \cos^2\varphi_l \rangle - \langle \cos\varphi_l \rangle^2 \right] / k_B T \qquad (5.3)$$

and

$$\chi_\rho = \left[(\langle \rho^2 \rangle - \langle \rho \rangle^2)/\text{Å}^2 \right] / k_B T \qquad (5.4)$$

as shown in Fig. 5.2.

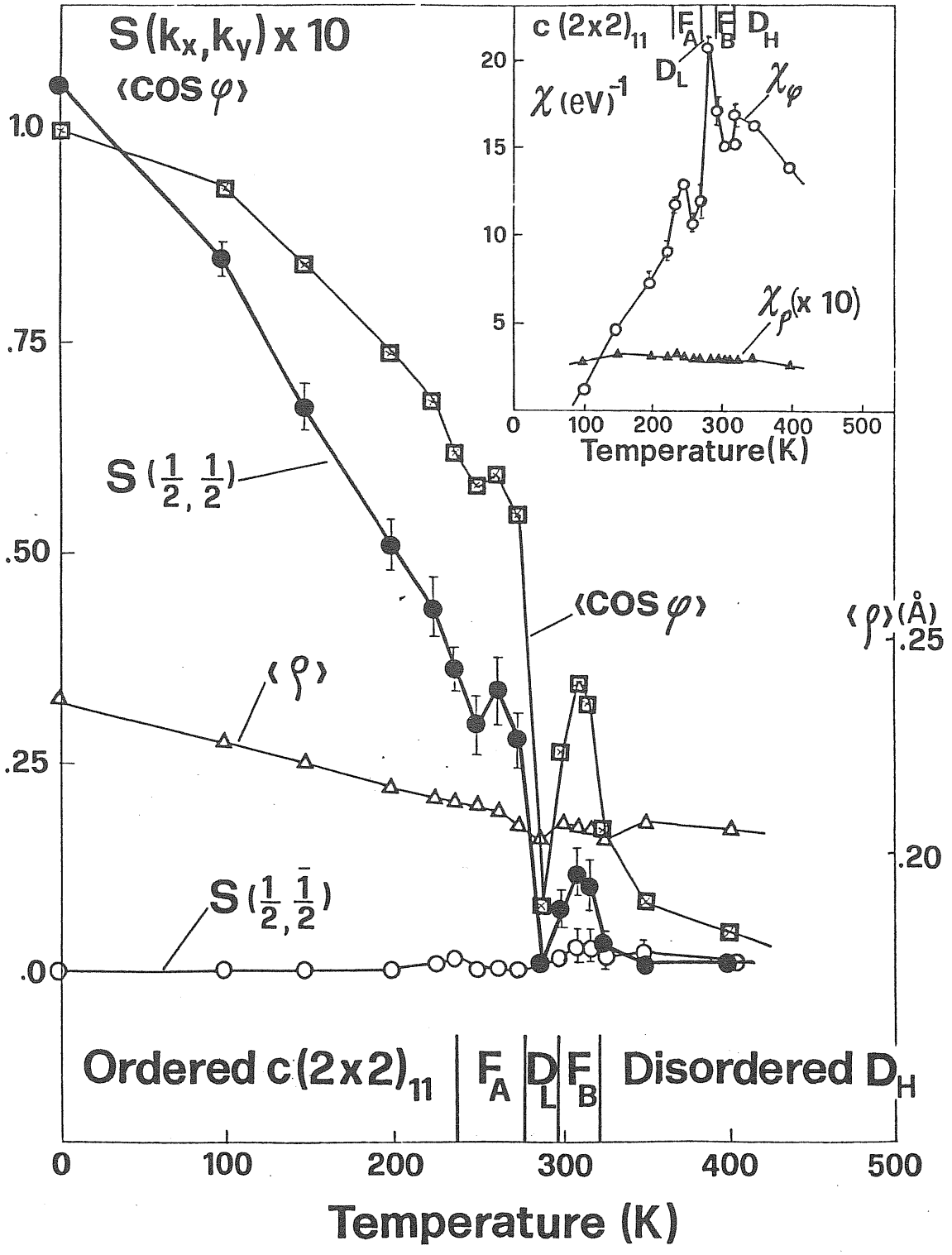

Fig.5.1 Surface structure factor and order parameter of the reconstructed W(001) surface. Phase boundaries indicated at the bottom are obtained by studying phase correlations (see section 5.4).

The flatness of χ_ρ confirms that amplitude fluctuations are not important. The peaks of χ_φ, instead, underline the crucial rule of phase fluctuations.

In finer detail the switch from order to disorder takes place through three intermediate transitions all compressed in a rather narrow temperature range near 300K. These transitions are heralded by weak structures appearing in S(1/2,1/2) as well as in $\langle\cos\varphi\rangle$ and also confirmed by

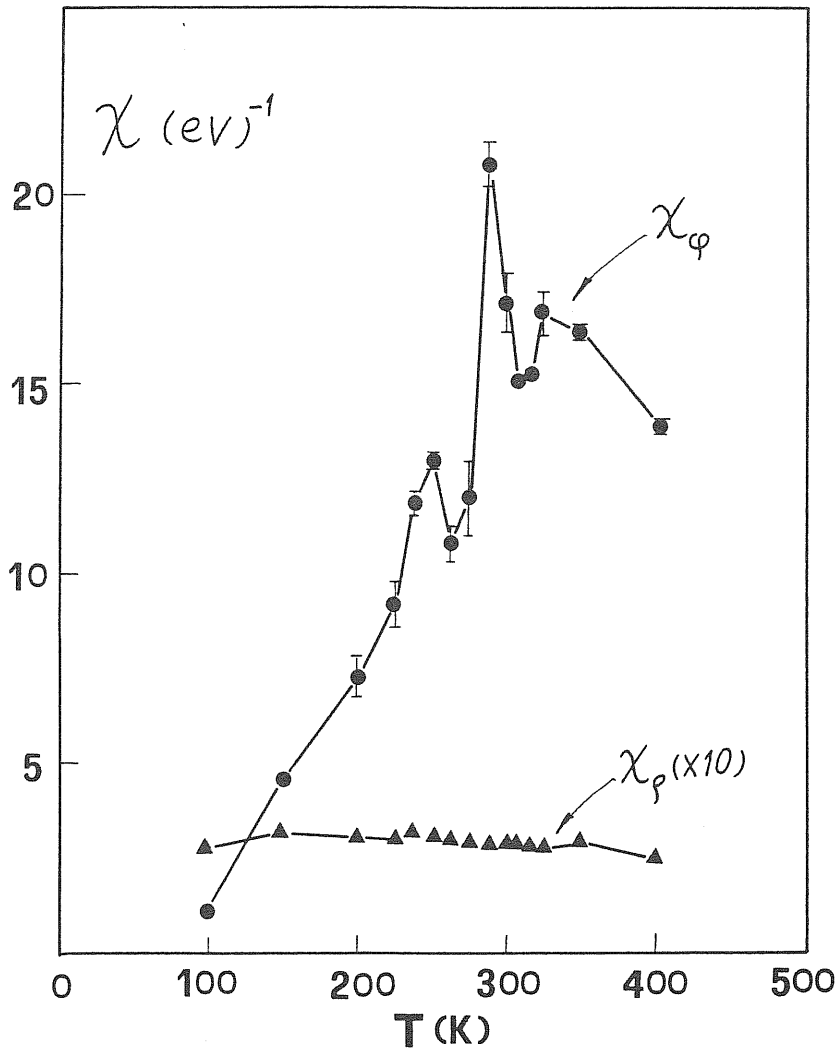

Fig.5.2 Phase and amplitude susceptibilities χ_ρ and χ_φ of W(001) surface.

several peaks of the phase susceptibility χ_φ appearing on that temperature range. The feature of these intermediate phases and values of transition temperatures between them, as we denoted in the bottom of Fig.5.1, have been clarified by the study of surface spatial correlations as we will show in the following section.

5.4 Floating nature of intermediate phases

In order to clarify the nature of the intermediate phases and the values of transition temperatures between them, we have chosen to study the surface spatial correlations

$$C(R_{\ell m}) = \langle \cos\varphi_\ell \cos\varphi_m \rangle$$

As it has been discussed in the literature /93,94/, for large separation $R_{\ell m}$, a nonzero constant limit of $C(R_{\ell m})$ indicates long-range order, an exponential decay indicates disorder, and a power-law decay $|R_{\ell m}|^{-\eta}$ is expected for a two dimensional floating phase. Our results of spatial correlations for the W(001) surface are shown in Fig 5.3 for various temperatures. Dramatic switches between three regimes are apparent near 250K (ordered to floating), between 275 and 287K (floating to disordered) between 287 and 300K (disordered to floating), and finally near 320K (floating to disordered). We have denoted the corresponding phases as c(2x2), F_A, D_L, F_B, and D_H respectively, as shown

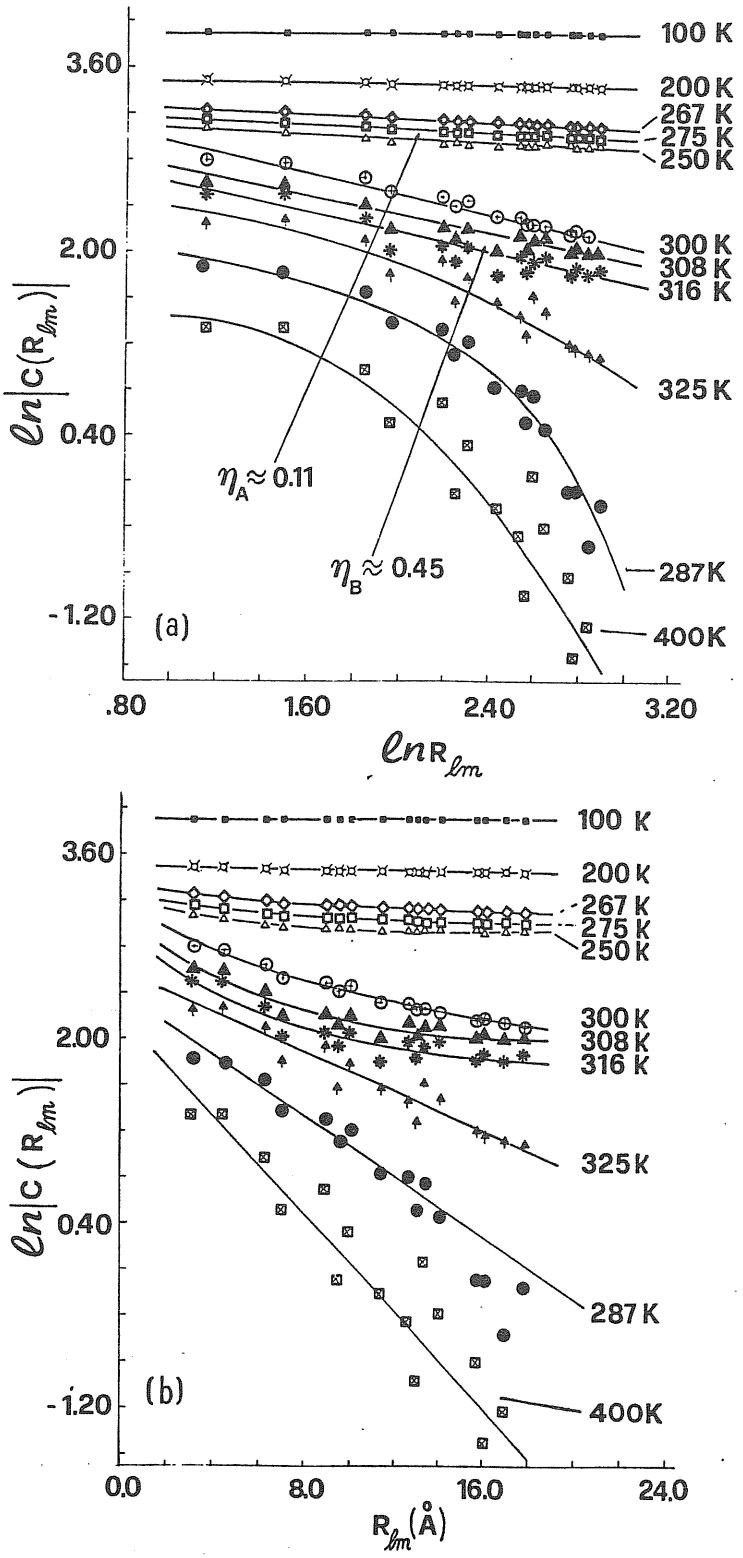

Fig.5.3 Spatial decay of phase correlations at various temperatures. Note sharp switches between ordered (constant), floating (power-law) and disordered (exponential).

in Fig. 5.1. The phases D_L and D_H exhibit exponential decay and are disordered. Instead the F_A and F_B phases display power-law correlations with η_A=0.11 and η_B=0.45 and are floating/93,94/.

The presence of ordered domains typical of a warm incommensurate phase is detectable in the snapshots of Fig.5.4 for both F_A and F_B. In the case of F_A, four types of domains (denoted α, β, γ and δ meaning $\langle\varphi\rangle$=0, $\pi/2$, π and $3\pi/2$ respectively) tend to show up (though Fig.5.4 shows only three of them). The phase F_B also shows domains, but differs from F_A in two important ways. First, the average distortion phase $\langle\varphi\rangle$ inside each domain has switched from 0 to $\pi/4$ (modulo $\pi/2$). This means that locally the reconstruction has become C(2x2)<100>, like in H/W(001) /18,47/. Secondly, only two types of domains, namely α', β' meaning $\langle\varphi\rangle=-\pi/4$ and $\pi/4$ respectively, or γ', δ' with $\langle\varphi\rangle=3\pi/4$, $-3\pi/4$ tend to appear simultaneously. It is tempting to associate the latter difference between F_A and F_B with their different power-law exponents η_A and η_B. In fact/93,94/, for an incommensurate phase with four types of domains (P=4) one expects $\eta=2/p^2=0.125$; with two types of domains (p=2) $\eta=2/p^2=0.5$. These two values are rather close to η_A and η_B, respectively.

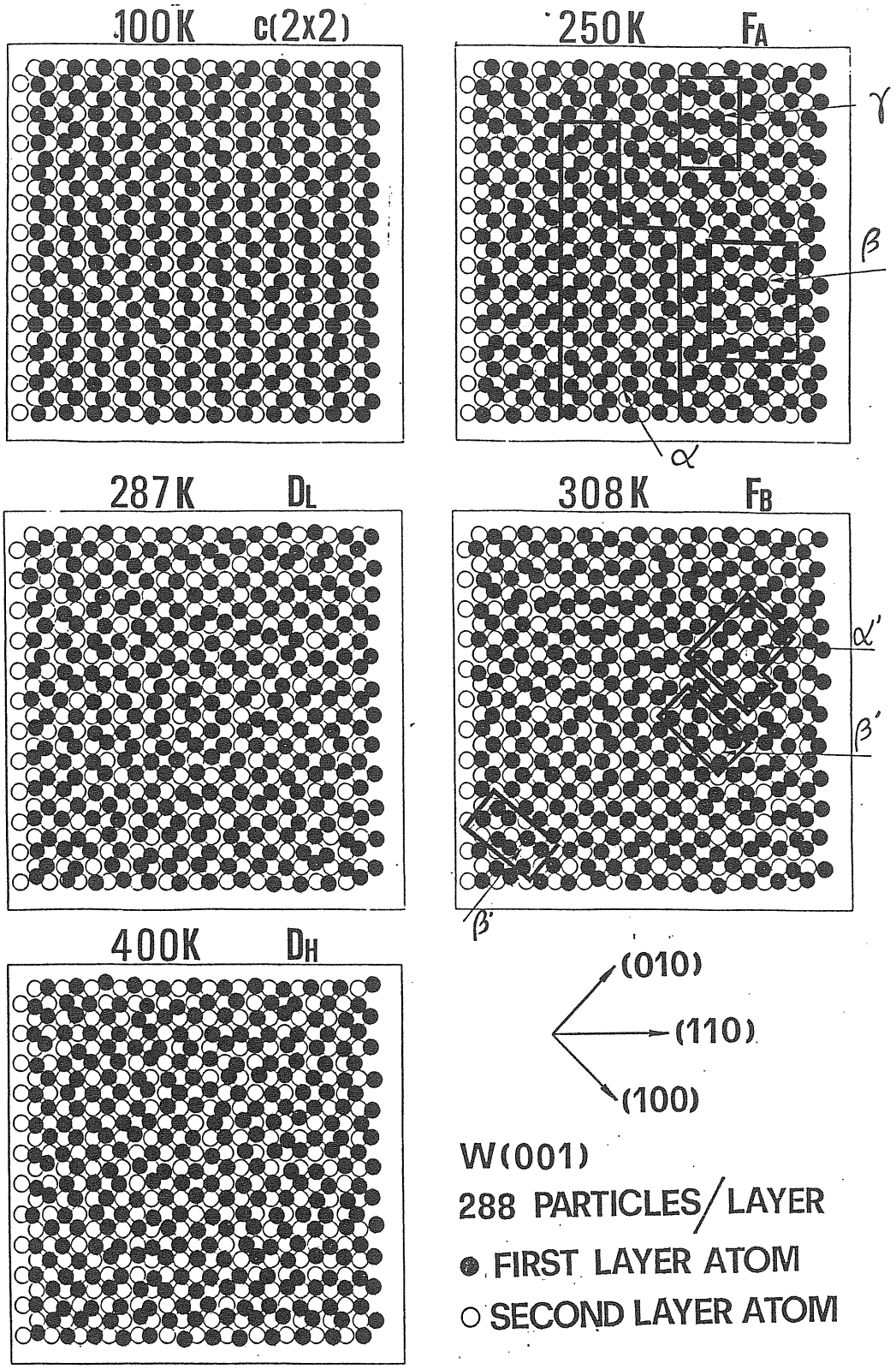

Fig.5.4 Snapshots of the two upperst atomic layers in the five different phases obtained. Some domains of different orientation simultaneously present in the two floating phases F_A and F_B are marked. The radius of the circles used to represent the atoms has been arbitrarily chosen and the distortion amplitudes enhanced by a factor of three for better visualization.

5.5 Surface Atomic Structure

In our MD simulations, we have monitored the surface atomic structures in real and reciprocal space by the calculated surface pair-correlation function $g_S(r)$ and the surface static structure factor S(kx,ky). We have also plotted the averaged atomic positions in order to give a visual impression of the surface atomic structures.

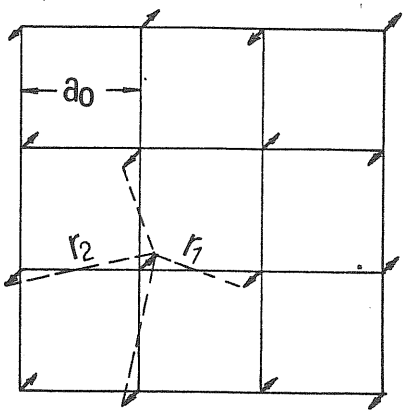

Fig.5.5 Illustration of surface pair-correlation function splitting upon the c(2x2) reconstruction.

The surface pair-correlation function was defined in the conventional way but it refers now only to surface atoms, i.e., $g_s(r)$ is a probability of finding another surface atom at distance r while a surface atom is in the origin. As one can see from Fig.5.5, on a (1x1) surface each surface atom has four nearest surface neighbours at distance a =3.16A and four next-nearest neighbours at distance $R=\sqrt{2}\,a_o$=4.47A. When the surface is reconstructed to $c(2x2)_{<11>}$ structure, the four nearest neighbours of the (1x1) surface will split into two couples of neighbours at distances

$$r_1 = a_o\sqrt{1-\sqrt{2}\left(\frac{2\rho_o}{a_o}\right)+\left(\frac{2\rho_o}{a_o}\right)^2}$$

$$r_2 = a_o\sqrt{1+\sqrt{2}\left(\frac{2\rho_o}{a_o}\right)+\left(\frac{2\rho_o}{a_o}\right)^2}$$

respectively.

The MD result of surface pair-correlation functions for the W(001) surface is shown in Fig. 5.6. Two peaks at R1≈ 2.80 Å and R2≈3.48 Å at low temperature T=100K clearly indicate the formation of c(2x2) zig-zag structure with distortion amplitude ρ_0=0.22Å. As the temperature is increased, these two peaks begin to smear out and finally at T=400K become a broad single peak around a_ρ=3.16 Å, i.e., the first surface neighbour distance of the (1x1) surface. Therefore, the W(001) at high temperature is disordered because the peak of $g_s(r)$ is very broad.

A direct study of S(kx,ky) near (1/2,1/2) and (1/2,-1/2) is shown in Fig.5.7. The sharp extra spots at (1/2,1/2) at T=100K and the much broader distribution of S(Kx,Ky) around (1/2,1/2) at T=400K also indicate the c(2x2) phase for low temperature and a disordered phase for high temperature. Moreover, the splitting of one or other k-point intensities in the intermediate temperature range directly suggests the incommensurate nature of the intermediate phases. Note that in the meanwhile an apparent incommensurate splitting of the (1/2,1/2) spots are seen at 250K and 287K. Correlations show that incommensurability is still present at 308K while at 287K the surface is disordered.

The time plot of S(Kx,Ky) for Kx=1/2, Ky= $\pm$1/2 is shown

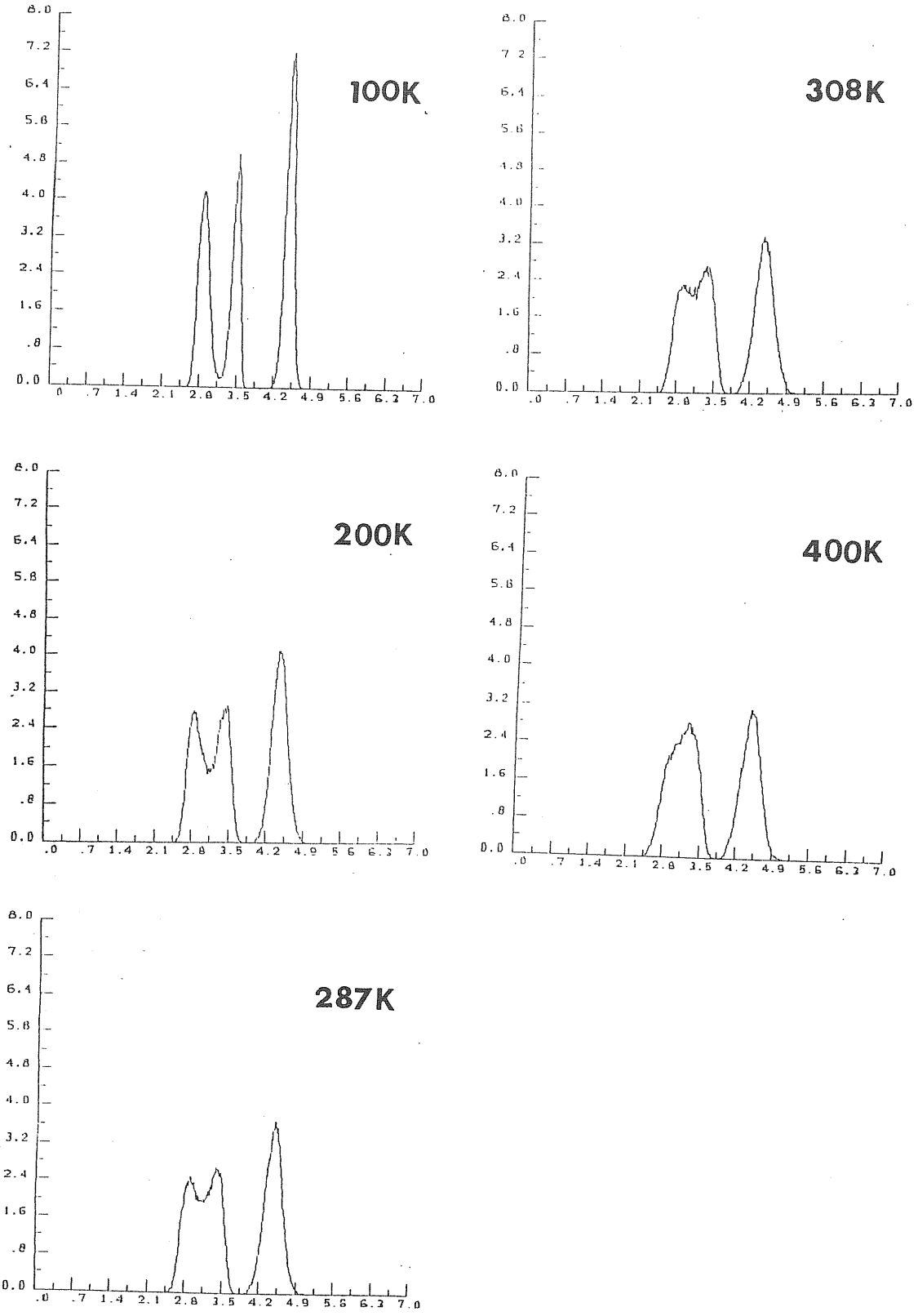

Fig.5.6 The pair-correlation functions of the upper surface at various temperature.

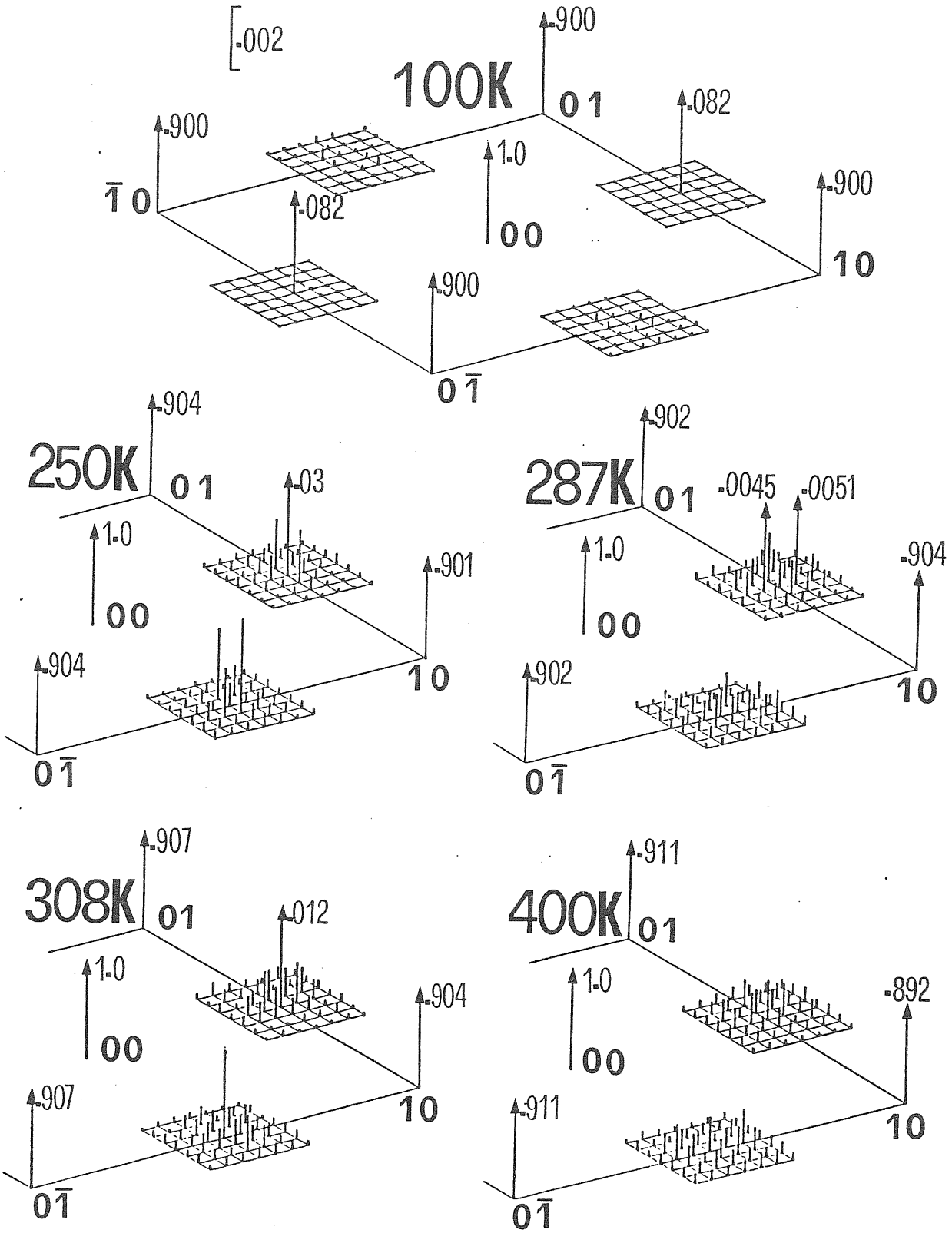

Fig.5.7 Perspective view of S(Kx,Ky) at five different temperatures. The picture shows the (0,0)(0,1) Bragg peaks and the K-space regions around (1/2,1/2) and (1/2,-1/2). Our K-grid, due to finite box size, is $\Delta K = 2\pi/a(0.06, 0.06)$.

in Fig.5.8. One sees again that while at low temperature only one type of domains is present, two types of domains tend to show up near the transition region. The development of domains not only suggests the possible incommensurability, but also suggests the persistence of short-range order in the disordered phase. This short-range order nature can also be seen from the integration of S(K) about $k = 2\pi/a(1/2,1/2)$ as shown in Fig.5.9. It shows that there is still a remarkable intensity distributed around the half order position at those high (T=400K) temperatures.

In order to give a visual impression of the surface structure, we have plotted out the averaged atomic coordinates for the five different temperatures corresponding to the five phases denoted in Fig.5.1 as shown in Fig.5.10. Again one sees clearly the zig-zag row parallel to <110> at T=100K and short-range order structure at higher temperature.

Finally, the log plot of distortion amplitude $u_l^\circ (= \rho \cos\varphi)$ versus layer index l at T=100K is given in Fig.5.11. The straight line of $\log u_l^\circ$ verses l indicates the exponential decay of the distortion amplitude into the bulk $u_l^\circ = u_1^\circ e^{-(l-1)a/2\lambda}$ (l=1 denote the surface layer) with $\lambda \approx 1$ Å. This means that the reconstruction is mostly localized on the surface layer and the phase transition is two dimensional in nature.

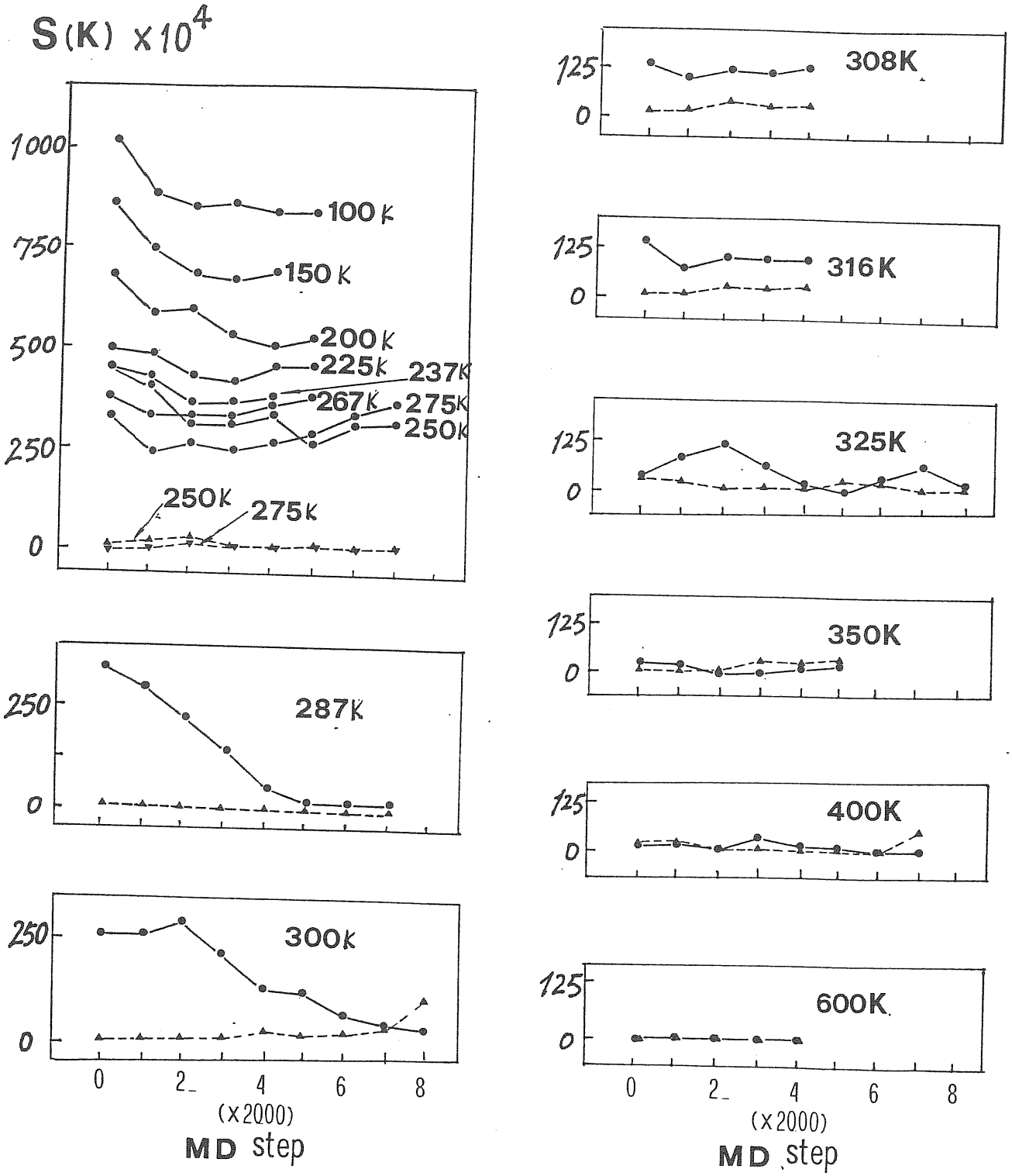

Fig.5.8 S(1/2,1/2) (solid line) and S(1/2,-1/2) (dash line) as a function of MD run at various temperatures. Each MD point consists of 2000 MD steps averaging.

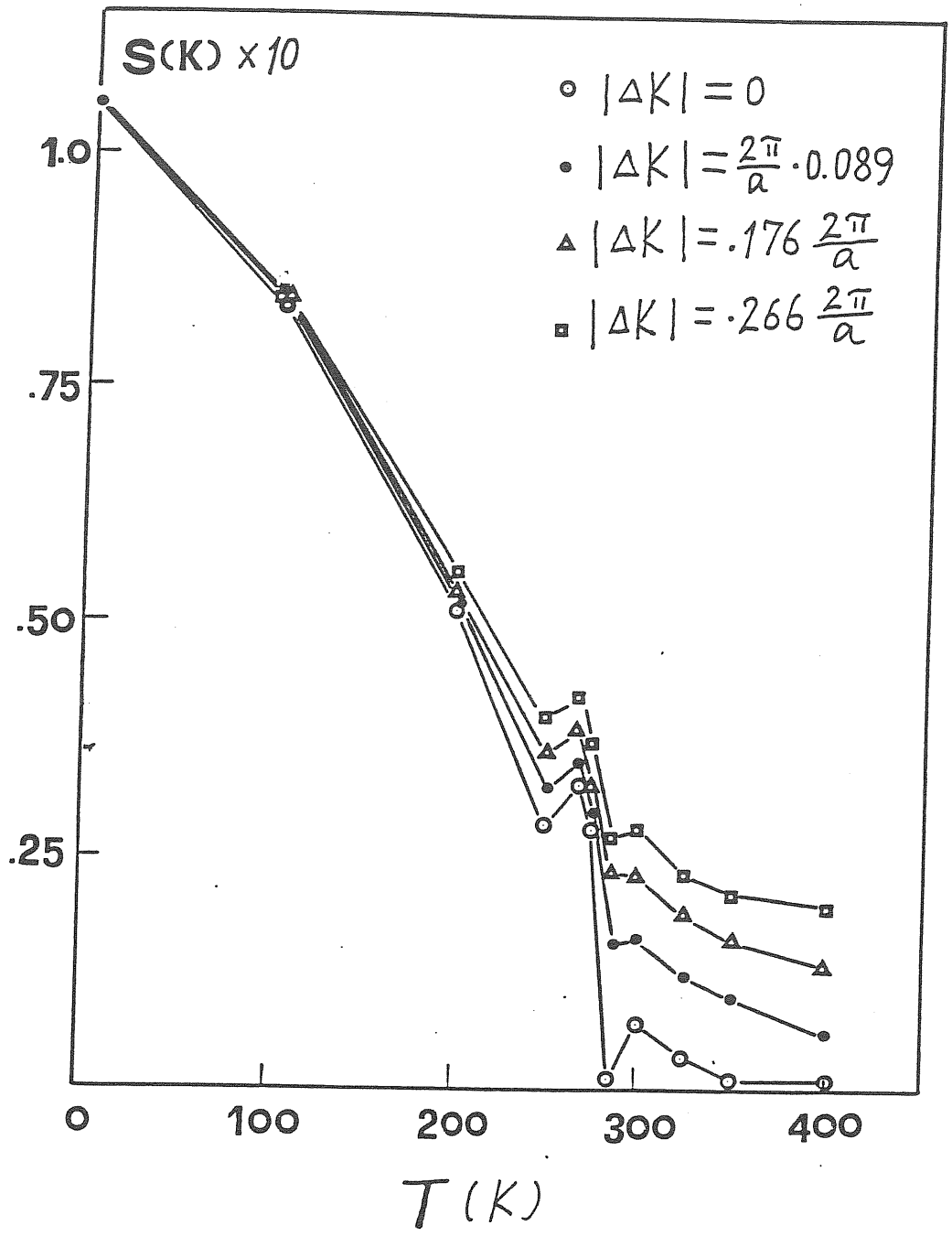

Fig.5.9 The integrated surface structure factor S(Kx,Ky) near Kx=Ky=1/2. The values of S(K) are the sum of S(Kx,Ky) over all K points within a circle of radius $|\Delta\vec{K}|$ and centred at K =2π/a(1/2,1/2) respectively.

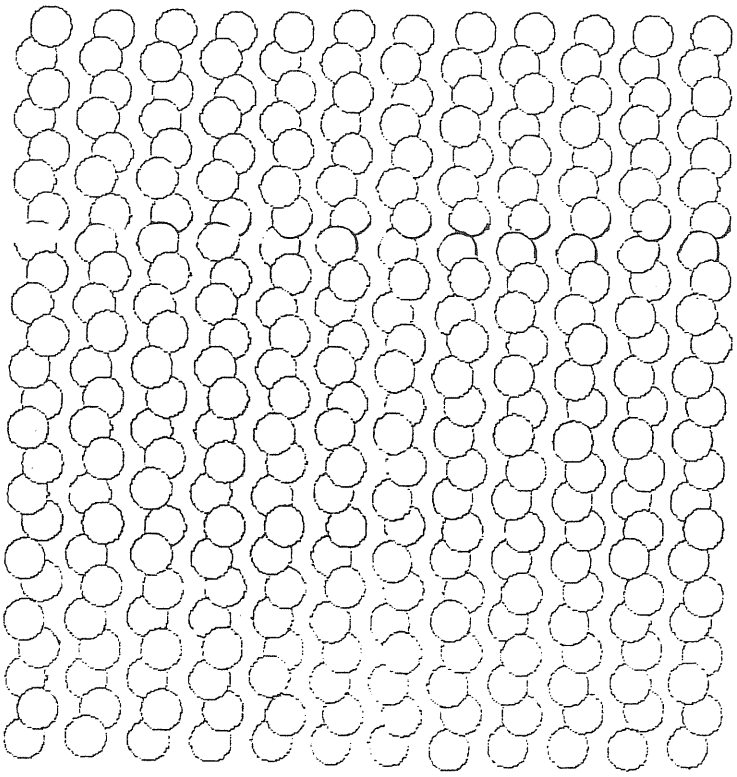

100K

TOP VIEW
(SURFACE LAYER)

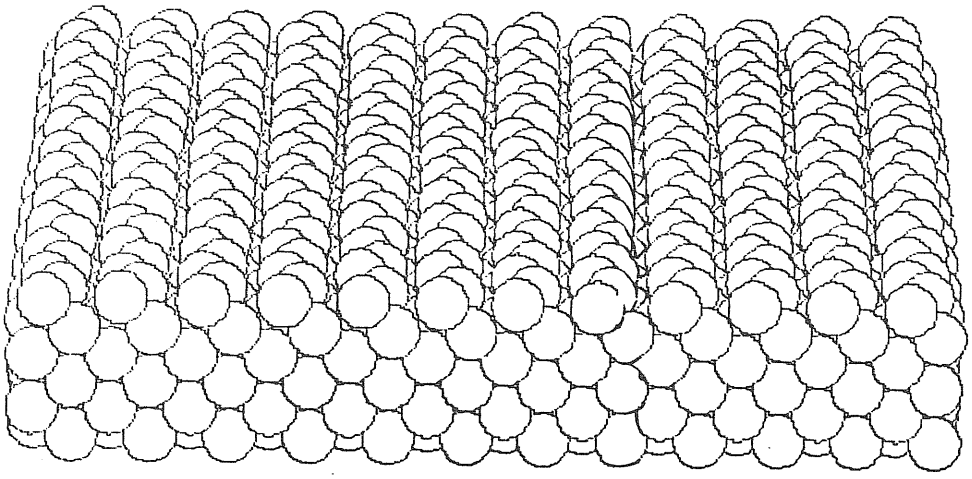

FRONT VIEW

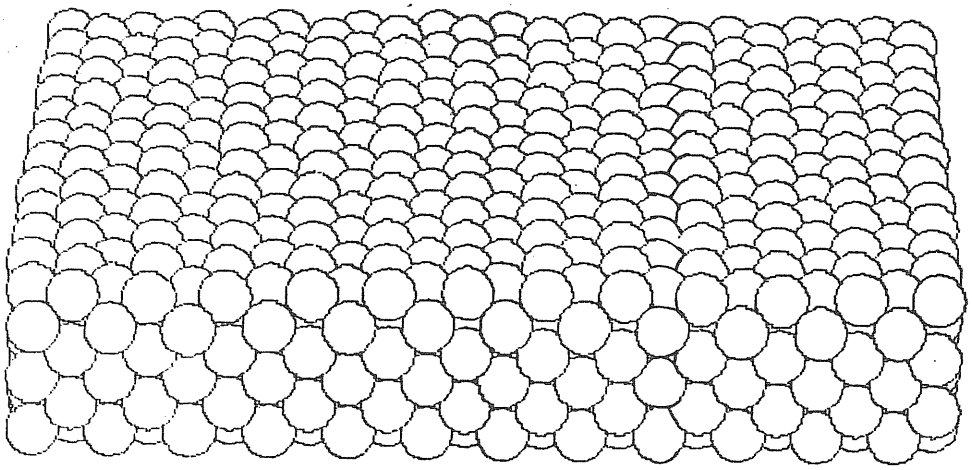

RIGHT SIDE VIEW

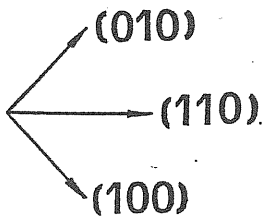

Fig.5.10 The views of atomic position of W(001) surface at five different temperatures. The radius of the circles used to represent the atoms have been arbitrarily chosen and the distortion amplitudes enhanced by a factor of three for better visualization. *(See also the next 4 pages)*

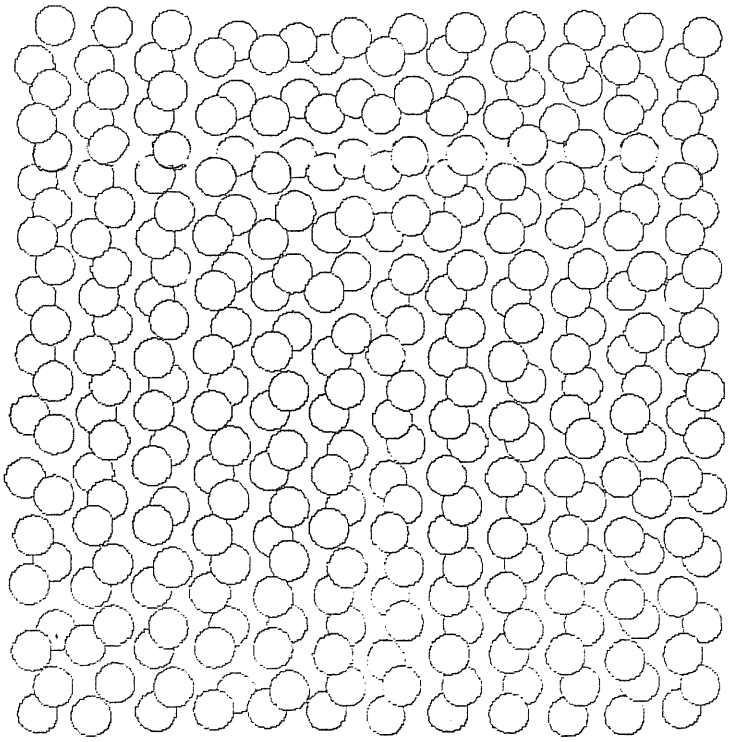

250K

TOP VIEW
(SURFACE LAYER)

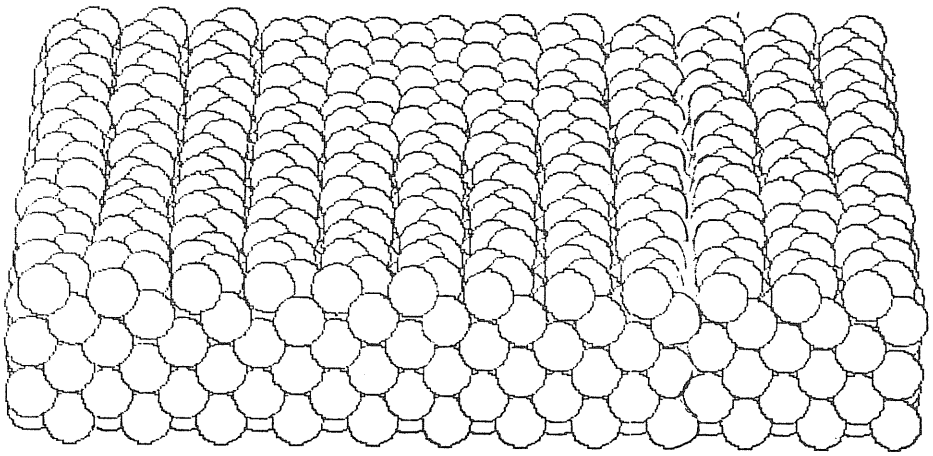

FRONT VIEW

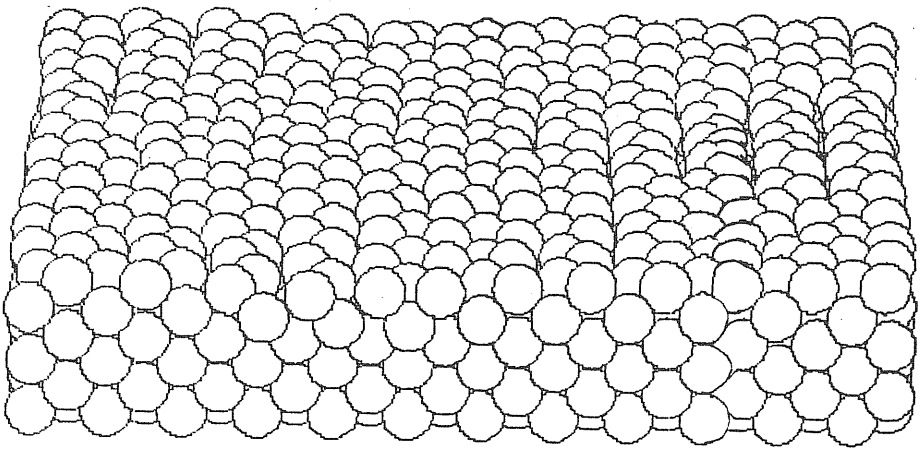

RIGHT SIDE VIEW

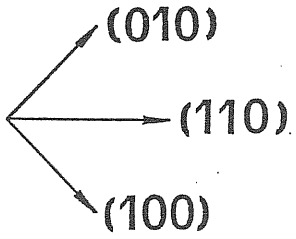

Fig. 5.10 (b)

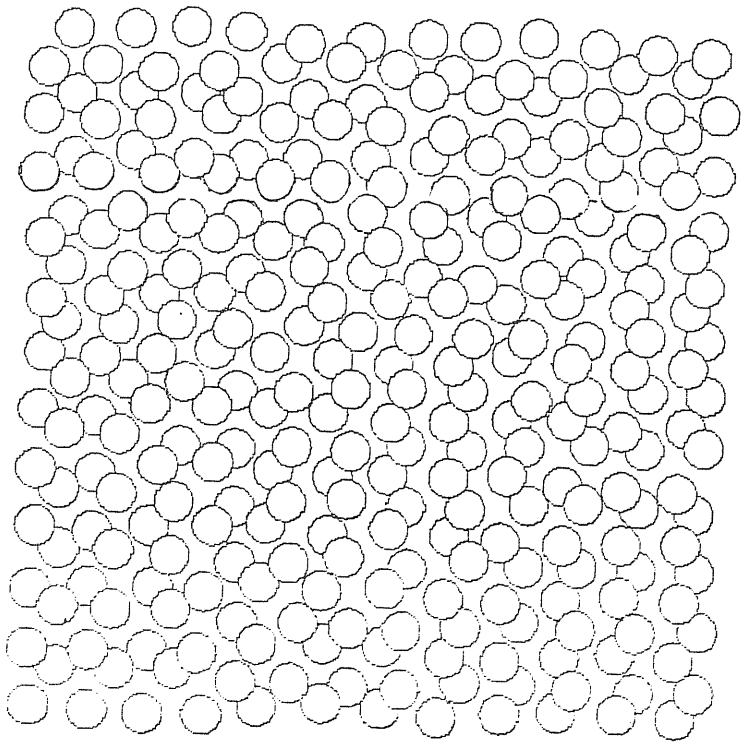

287K

TOP VIEW
(SURFACE LAYER)

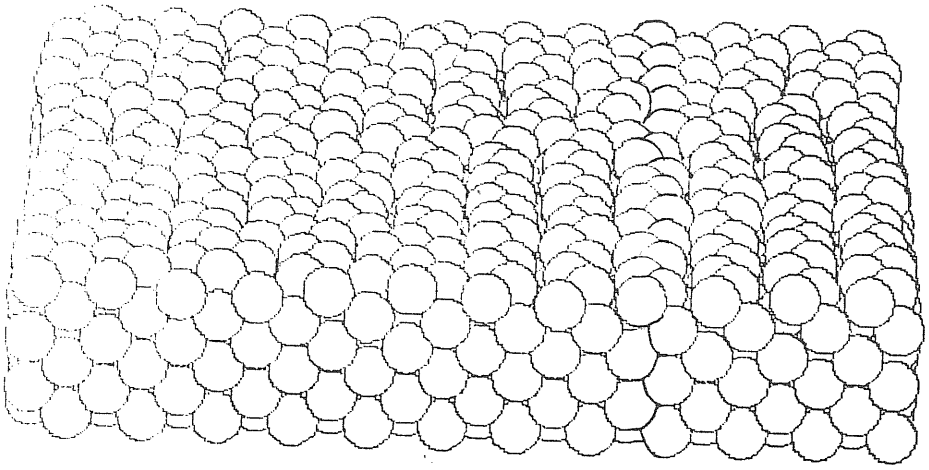

FRONT VIEW

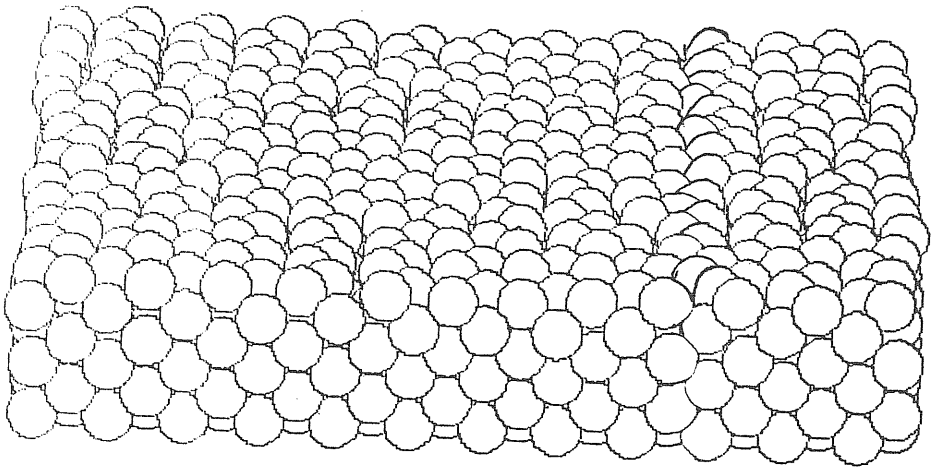

RIGHT SIDE VIEW

(010)

(110)

(100)

Fig. 5.10 (c)

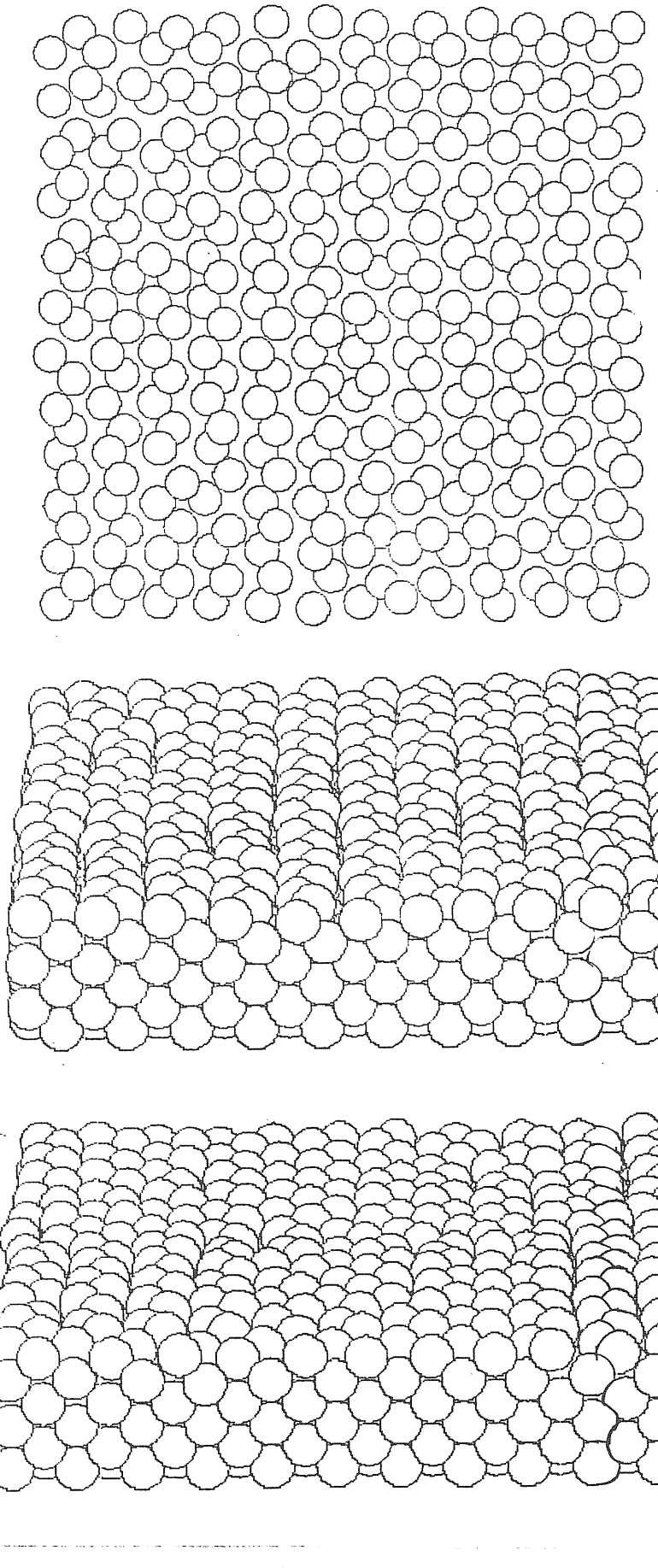
308K
TOP VIEW
(SURFACE LAYER)
FRONT VIEW
RIGHT SIDE VIEW
(010)
(110)
(100)

Fig. 5.10 (d)

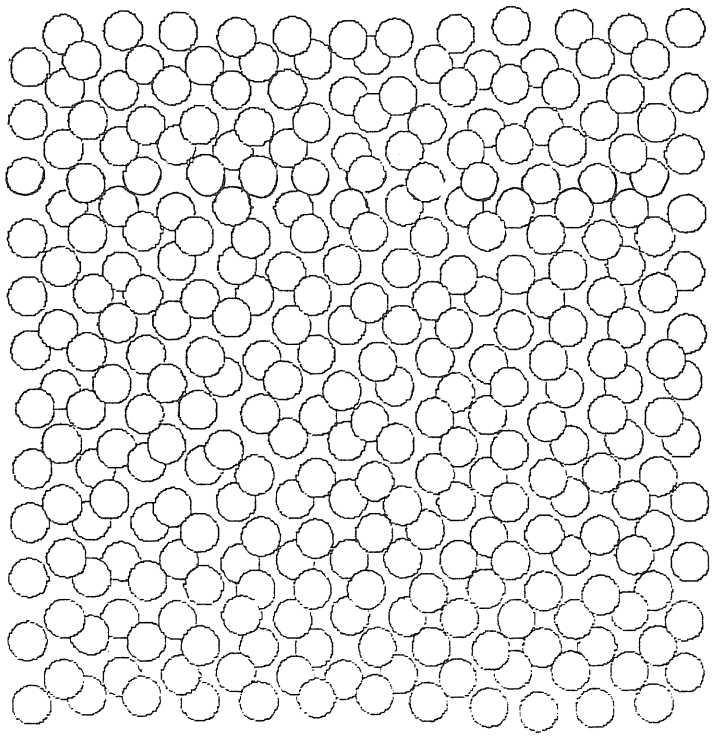

400K

TOP VIEW
(SURFACE LAYER)

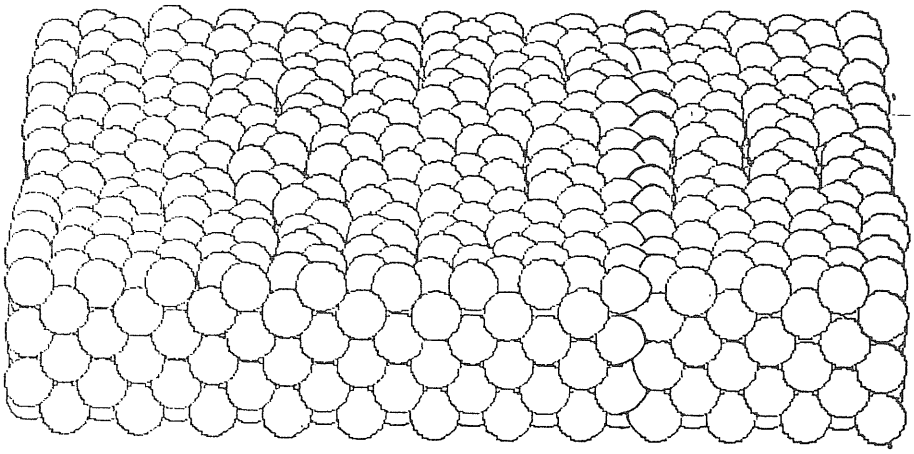

FRONT VIEW

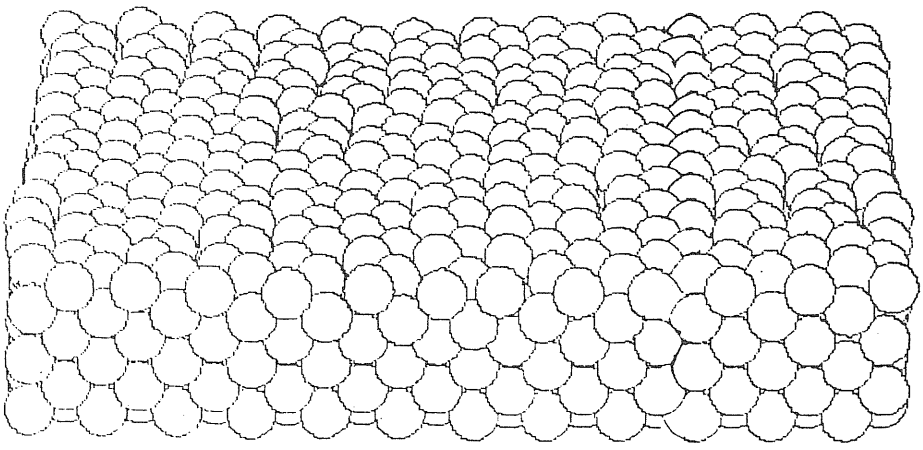

RIGHT SIDE VIEW

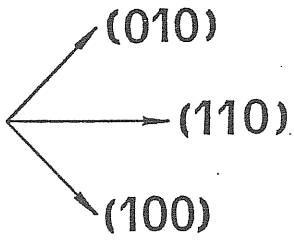

Fig. 5.10 (e)

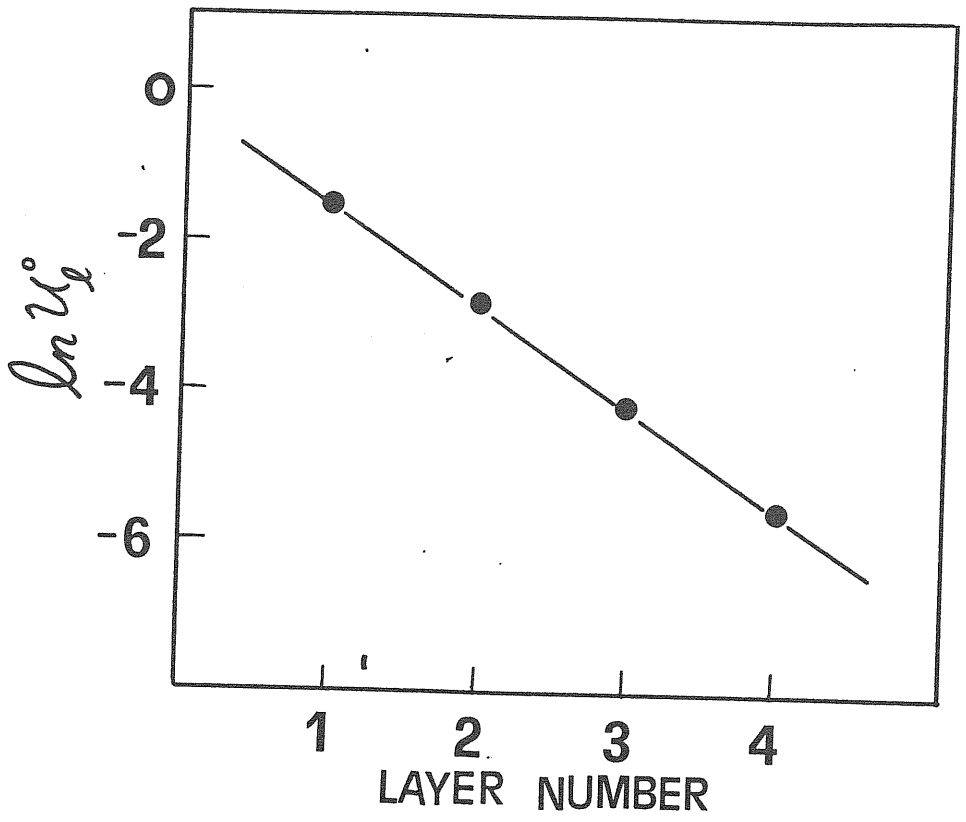

Fig.5.11 Distortion amplitude of the reconstructed W(001) surface as a function of the depth (surface l=1).

5.6 Energy and specific heat

Since the system is not subjected to time dependent external forces, the hamiltonian of the system is a constant of the motion. With a fixed MD cell, the hamiltonian reads

$$\mathcal{H} = \sum_i \frac{1}{2} m_i v_i^2 + \frac{1}{2} \sum_{<ij>}{}' \phi(r_{ij}) \qquad (5.5)$$

Here Vi is the velocity of the ith particle and $\phi(r_{ij})$ is the potential energy described in chapter 4. The total energy of the system is evaluated through the time average of H in the course of MD simulation

$$E = \langle \mathcal{H} \rangle \qquad (5.6)$$

An alternative way of writing Eq.(5.5) is

$$\mathcal{H} = \sum_i \left[\frac{1}{2} m v_i^2 + \frac{1}{2} \sum_j{}' \phi(r_{ij}) \right] = \sum_i \varepsilon_i \qquad (5.7)$$

then

$$E = \langle \mathcal{H} \rangle = \langle \sum_i \varepsilon_i \rangle = \sum_i \langle \varepsilon_i \rangle \qquad (5.8)$$

where

$$\langle \varepsilon_i \rangle = \langle \frac{1}{2} m v_i^2 + \frac{1}{2} \sum_j{}' \phi(r_{ij}) \rangle$$

is the energy associated with the ith particle.

It is clear that in addition to total energy of the system, the energy associated with each atomic layer can also

be evaluated in the MD simulation. For example, we can define the surface energy as the sum of energies of the surface layer atoms, i.e.,

$$E_S = \langle \mathcal{H}_S \rangle = \sum_{\ell} \langle \mathcal{E}_{\ell} \rangle \qquad (5.9)$$

where $Hs = \sum_{\ell} \mathcal{E}_{\ell}$ is the hamiltonian associated with the surface layer, the sum running over all surface atoms.

Fig.5.12 shows the total energy as a function of temperature. The almost straight E-T line shows weak evidence of the phase transitions, contrary to the behaviour of the order parameters. We have attributed this result to the dominating bulk contributions, since the surface reconstruction affects mainly the surface layer, the changes in the structure of other bulk layers being negligible. On the other hand, the plot of surface energy Es of Fig.5.13 does show strong evidence of a second order phase transition, namely the change in the slope of Es-T curve near the transition temperature.

In a constant temperature, constant volume MD simulation, the specific heat of the system can be evaluated by means of total energy fluctuations /59/,

$$C_V = \frac{\partial E}{\partial T} = \frac{\langle \mathcal{H}^2 \rangle - \langle \mathcal{H} \rangle^2}{k_B T^2} \qquad (5.10)$$

Our calculation of Cv according to (5.10) versus temperature is given in Fig. 5.14a. Several peaks in the transition region are already visible. However, due to the same rea-

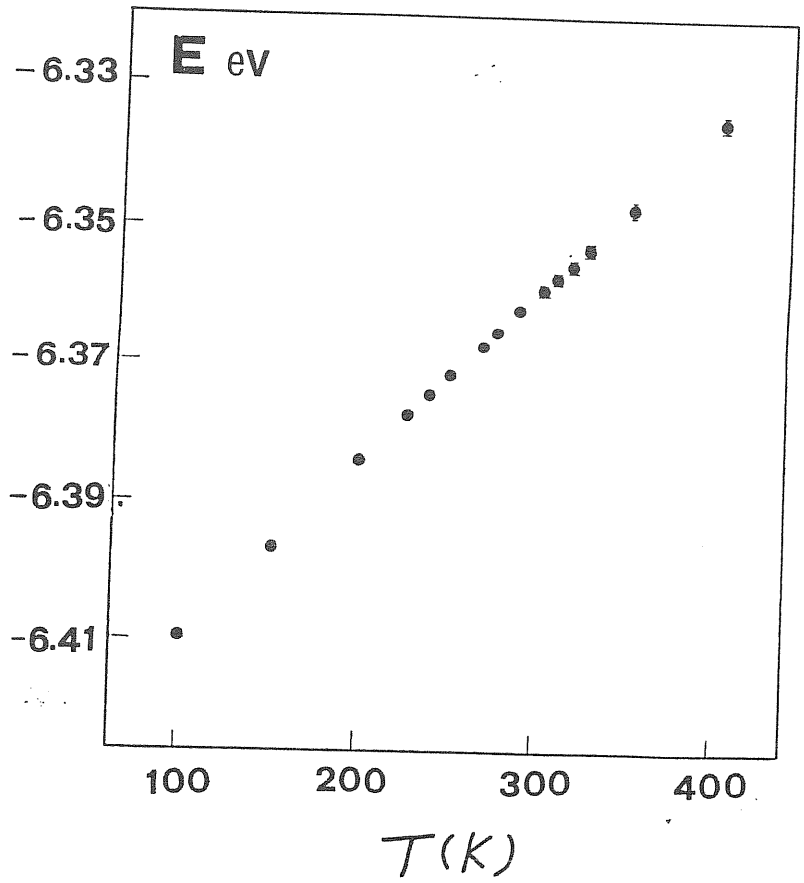

Fig.5.12 Total energy as a function of the temperature.

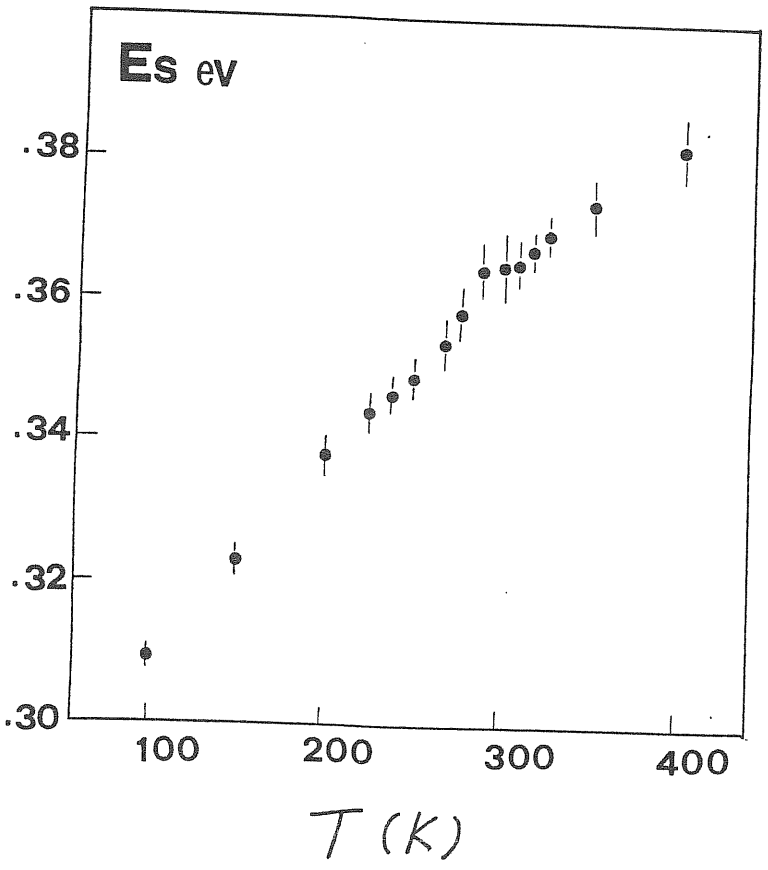

Fig.5.13 Surface energy as a function of the temperature.

son as for the total energy, the singularity of Cv at the transition temperature has been reduced by the bulk contributions.

In order to characterize the surface phase transition we found it possible to single out the contribution of the surface atoms to the specific heat Cv. We refer to this partial contribution as surface specific heat C_v^S. Following the classical statistical mechanics, the average surface energy Es defined as (5.9) can be calculated as

$$E_S = \langle \mathcal{H}_S \rangle = \frac{\int d\vec{r}^N d\vec{p}^N \mathcal{H}_S e^{-\beta \mathcal{H}}}{\int d\vec{r}^N d\vec{p}^N e^{-\beta \mathcal{H}}} \qquad (5.11)$$

Hence

$$\int d\vec{r}^N d\vec{p}^N [E_S - \mathcal{H}_S(\vec{r}^N \vec{p}^N) e^{\beta[A(V,T) - \mathcal{H}(\vec{r}^N \vec{p}^N)]} = 0 \qquad (5.12)$$

where A(v,t) is the free energy of the system. Differentiating both sides with respect to β we obtain

$$\frac{\partial E_S}{\partial \beta} + \int d\vec{r}^N d\vec{p}^N e^{\beta(A-\mathcal{H})}(E_S - \mathcal{H}_S)(E - \mathcal{H}) = 0 \qquad (5.13)$$

i.e.

$$k_B T^2 \frac{\partial E_S}{\partial T} = \langle (\mathcal{H}_S - E_S)(\mathcal{H} - E) \rangle \qquad (5.14)$$

Therefore the surface specific heat Cv is given by

$$C_V^S = \frac{\partial E_S}{\partial T} = \frac{\langle (\mathcal{H}_S - E_S)(\mathcal{H} - E) \rangle}{k_B T^2} \qquad (5.15)$$

where Hs, Es, H and E were defined through (5.5), (5.6) and (5.9) respectively. The calculated C_V^S versus temperature is shown in Fig.5.14b. Three peaks clearly show up in the surface specific heat C_V^S signaling that there are at least three phase transitions as also indicated by the phase susceptibility χ_φ of Fig.5.3. However, the peak positions are somewhat different from that of χ_φ due to finite size effects /95/.

5.7 Summary and discussions

While our starting point is clearly phenomenological, a very substantial effort has been made to keep all details as realistic as possible to represent the true state of affairs of clean W(001) surface. There is of course arbitrariness in the choice of surface potential parameters, however, as we will show in the next chapter, none of our essential findings are altered by reasonable parameter changes. In the present study, we have been able to reproduce the low temperature $c(2x2)_{\langle 11\rangle}$ reconstructed surface as suggested by the LEED experiment. The distortion amplitude of $\langle \rho \rangle = 0.23$ Å and the energy gain of $\Delta E = 31$ meV per surface atom have been estimated for the reconstruction. The temperature behaviour of order parameters roughly indicates the phase transition totake place near $T_c \sim 250$K which is very close to the experimental value. While there is still some

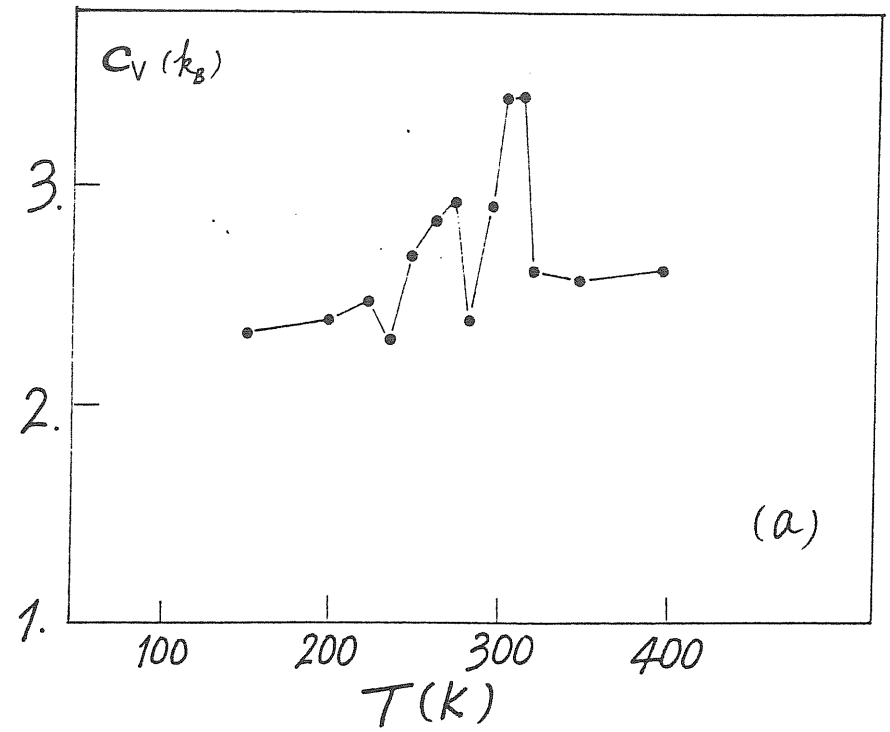

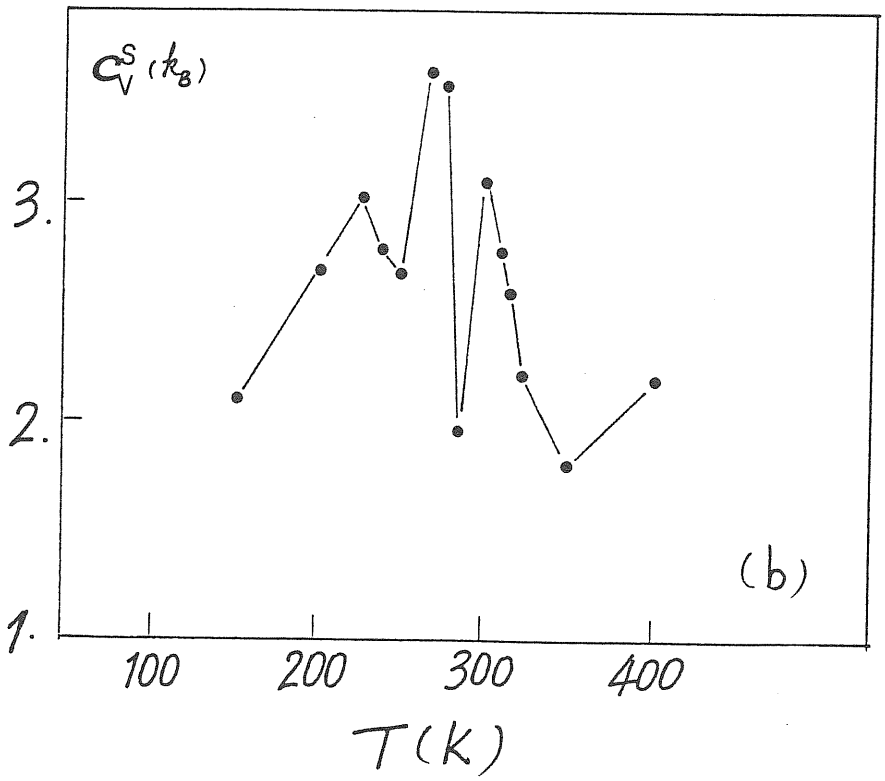

Fig.5.14 Specific heat Cv and surface specific heat C_V^S as a function of the temperature.

controversy on the precise atomic structure of the high temperature phase experimentally, the present MD results indeed tend to suggest a disordered or short-ranged ordered structure for W(001) surface in the high temperature phase. In particular we found the phase transition to occur through loss of phase coherence. Domains develop in the critical region and the phase transition is dominated by the order-disorder behaviour. It is interesting to note that similar results concerning the short-range order nature of the high temperature phase have also been reported by Ying and collabrators based on some simpler two dimensional lattice hamiltonian for the W(001) surface reconstruction /19,20,21,40/. However, in our molecular dynamics simulation, we found that the transition from the ordered low temperature c(2x2) phase to disordered high temperature phase occurs through a sequence of narrow floating phases, which have not yet been detected experimentally.

At least three more points need to be further discussed. The first point concerns the convergency of our MD result presented in this chapter. In table 5.1 the MD steps used in the average have been listed explicitly for each temperature. By comparing this list with the time plot of S(K) of Fig.5.8, it is clear that the results we show in this chapter are converged and meaningful. Although our simula-

Table 5.1

THE MD STEPS USED IN THE AVERAGING

Temperature	MD steps used for averaging
100 K	The last 6000 steps
150 K	The last 4000 steps
200 K	The last 4000 steps
225 K	The last 6000 steps
237 K	The last 4000 steps
250 K	The last 8000 steps
267 K	The last 4000 steps
275 K	The last 8000 steps
287 K	The last 6000 steps
300 K	The last 8000 steps
308 K	The last 4000 steps
316 K	The last 4000 steps
325 K	The last 10,000 steps
350 K	The last 4000 steps
400 K	The last 8000 steps

tion starts from a c(2x2) reconstructed surface, we can also declare that the results are not altered by a different choice of starting configuration for the simulation. In order to clarify this point, we have made a test for a slab of n=144 with <100> orientation in which the simulation is started from T=100K and from an ideal (1x1) surface. The results show that a c(2x2) zig-zag structure is spontaneously formed as one sees from Fig.5.15.

The second point is how starting with our innocent-looking short-range hamiltonian, such a wealth of phases may

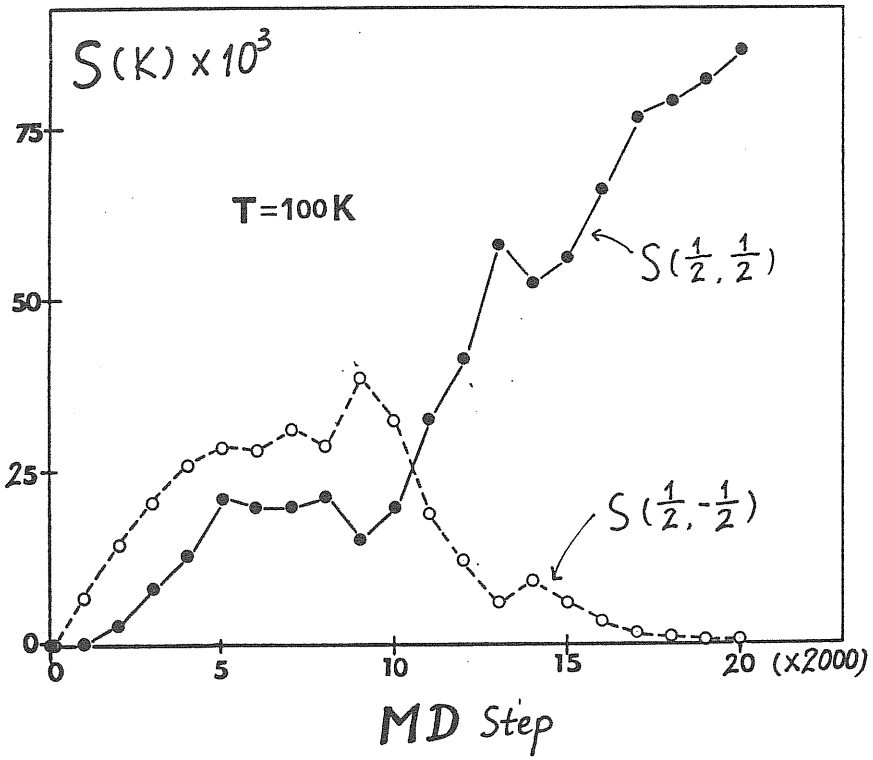

Fig.5.15 Surface structure factors S(1/2, 1/2) as a function of time for a 12X12 surface. The simulation is started with an ideal (1x1) surface. The large value of S(1/2,1/2) and almost zero value of S(1/2,-1/2) at longer time indicate that a single c(2x2) domain was spontaneously formed.

arise. We trace tentatively the reason to the tendency of the c(2x2) surface to reduce its (already small) cubic anisotropy (term γ in Eq.1.5) and eventually to reverse it's sign with temperature. This behaviour in fact can be roughly seen from the plot of the inverse phase susceptibility $1/\chi_\varphi$ versus temperature of Fig.5.16. The zero of $1/\chi_\varphi$ near T=300K suggests a zero cubic anisotropy near that temperature. It seems that the anharmonicity will be the first cause of this reduction of cubic anisotropy. In Fig.5.17 we show that by simply changing the surface anharmonic force constants γ_S and δ_S, we are able to pass from an incommensurate structure of F_A type (Fig.5.17a) to another incommensurate structure of F_B type (Fig.5.17c) with a pure X-Y

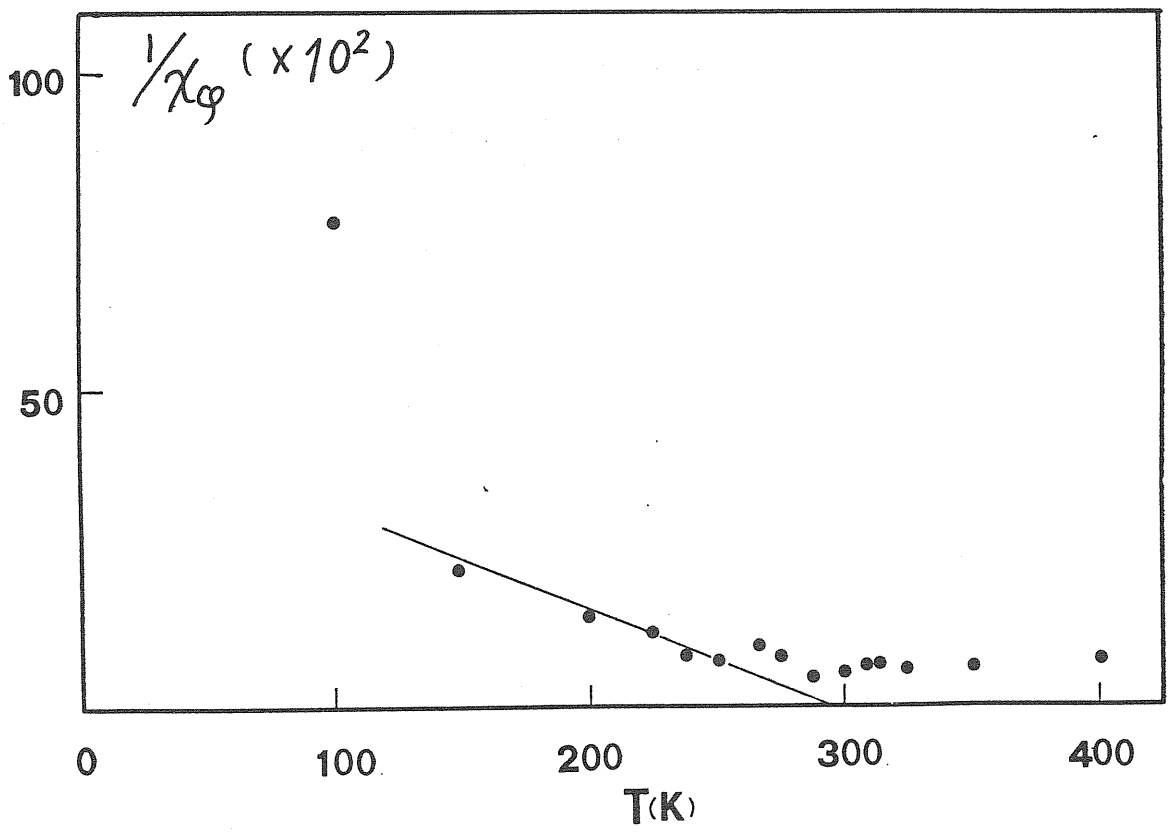

Fig.5.16 Inverse phase susceptibility $1/\chi_\varphi$ as a function of the temperature.

(Kosterlitz-Thouless/96/) type phase in between (Fig.5.17b). A second cause is a tendency, which has also been verified by slab phonon calculation /43,97/ of the cubic anisotropy to reverse sign as $\langle \varphi \rangle$ decreases. As discussed recently by Fasolino and Tosatti /97/, a reversal of cubic anisotropy does not just imply a switch from $\langle \varphi \rangle = 0$ to $\langle \varphi \rangle = \pi/4$. Coupling to surface acoustical modes, leads to incommensurate phases 'sandwiched' in between. Hence F_A and F_B could be sandwiched phases arising from the instablity of the $\langle \varphi \rangle = 0$ and $\langle \varphi \rangle = \pi/4$ parent phases respectively, with a narrow disordered region D_L necessary to divide them.

Finally, we may ask how our predicted phase diagram (Fig5.1) could be checked experimentally. Direct LEED detection of the phases F_A, D_L and F_B is not straightforward. The main reason is that in the absence of any intentional surface asymmetries, the four types of domains α, β, γ and δ are present in equal proportions at low temperatures. Thus, a superposition of four S(k) patterns like those of Fig.5.7, each rotated by 90°, will occur in LEED spectra. The incommensurate splitting becomes unobservable in such a superposition. An attempt at detecting the floating phases requires strong intentional asymmetries, introduced experimentally maybe by means of steps or otherwise /5,10,18/.

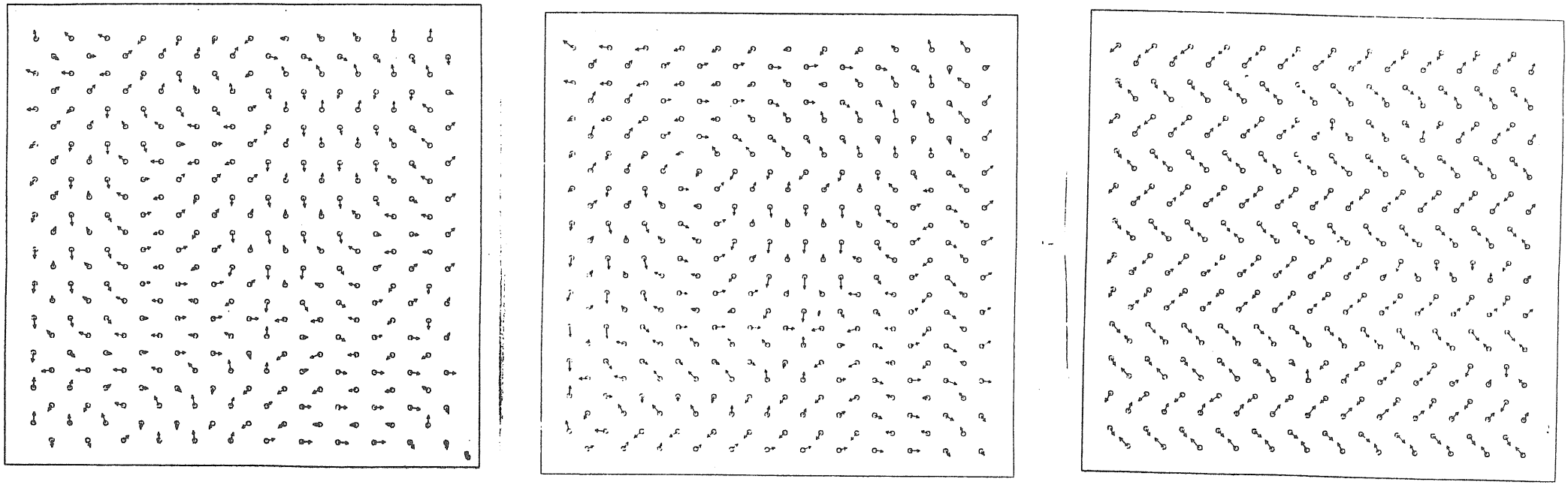

Fig.5.17 Displacement fields of the surface layer atoms corresponding to three different choices of surface anharmonic force constants.

Chapter 6

MD simulation by various choices of surface potentials and sizes

6.1 Introduction

Our result for the clean W(001) surface reconstruction phase transition presented in the previous chapter is based on a particular choice of surface potential parameters and of MD sample. Firstly, the choice of surface potential parameters is of course purely empirical and somewhat arbitrary. It would be interesting to see how the system behaves upon different choices of surface potential parameters. Secondly, it is also of importance to understand which effects might arise from the finite size samples (with periodic boundary conditions) used in the study of phase transitions. Such effects need to be minimized by an appropriate choice of simulation samples in order to obtain meaningful information about the phase transition. In the present study, our consideration of size effects consists of slab thickness effects, surface size effects and MD box orientation effects.

In order to study such effects, we have carried out extensive MD simulations based on various choices of surface potential parameters, and of MD box sizes, thicknesses and orientations in connection with the situation of the W(001)

surface reconstruction phase transition. It is found that none of our essential findings described in the previous chapters is altered by reasonable parameter changes. It is also found that in the transition region the MD simulation results are sensitive to the choice of surface size and orientation of MD samples. In fact, as we will see in the following, the surface potential we have used in the previous chapter is indeed an optimal one for the study of W(001) surface reconstruction phase transition. Moreover, the results presented in the previous chapter are meaningful also from the size effects point of view.

6.2 On the dependence on surface potential parameters

Besides the surface potential used in the previous chapter, we have studied several surface potentials with α_s, β_s differently chosen from the M5 region of phase diagram of Fig.1.19. All these surface potentials are constructed in the same form as that of Fig.4.5. The corresponding parameters are listed in table 6.1, where the potential B is the one we used in the previous chapter. At T=0, all these surface potentials give lower energy for the $c(2x2)_{<11>}$ reconstructed surface with respect to the unreconstructed (1x1) surface. The corresponding T=0 equilibrium distortion amplitude ρ_0 and the energy gain ΔE are also given in table 6.1. The temperature behaviour of

Table 6.1

LIST OF SOME SUFACE POTENTIALS

potential	α_S eV/Å^2	β_S eV/Å^2	γ_S eV/Å^2	δ_S eV/Å^2	V_{s_0}(eV)	E(eV)	Tc(K)	ρ_o(A)	h(A)
A	-0.975	-0.525	7.5	375.0	1.800	10.5	150	.150	0.020
B	-0.75	-0.938	3.75	225.0	1.7579	31	300	.235	0.028
C	-1.125	-0.563	3.75	225.0	2.7102	31	300	.230	0.025
D	-1.163	-0.60	3.75	225.0	2.8458	38	420	.240	0.030
E	-1.20	-0.60	3.75	225.0	2.9645	42	480	.240	0.030
F	-1.238	-0.71	3.75	225.0	3.1429	62	550	.270	0.030

static surface structure factor S(kx,ky) for kx=1/2, ky=1/2 obtained by MD simulation using these surface potentials is shown in Fig.6.1. The MD cell used for the simulation is an 8-layer bcc slab with 64 atoms per layer and oriented along the <100> direction. The simulation procedure is the same as described in chapter 5. Coarsely, one sees that the temperature behaviour of S(1/2,1/2) by various potentials is very similar apart from the value of transition temperature Tc. These results confirm that the soft M5 mode is indeed responsible for the W(001) surface reconstruction. It is also found that the phase transition temperature Tc estimated from the behaviour of S(1/2,1/2) of Fig.6.1 is roughly related to the T=0 energy gain by $\Delta E \sim K_B Tc$ as plotted in Fig.6.2. The larger ΔE, the higher Tc is. In particular, an energy gain of ΔE=30meV is found to predict a transition temperature compatible to the LEED data /1,2,4/.

It is interesting that while the surface potentials C and B predict the same energy gain, the same equilibrium distortion amplitude as well as transition temperature for W(001) surface reconstruction, their harmonic parameters α_S and β_S are, however, different. For this reason, the surface potential C has also been studied in some detail as to make a comparison with the detail results of potential B as described in the previous chapter. With the same MD pro-

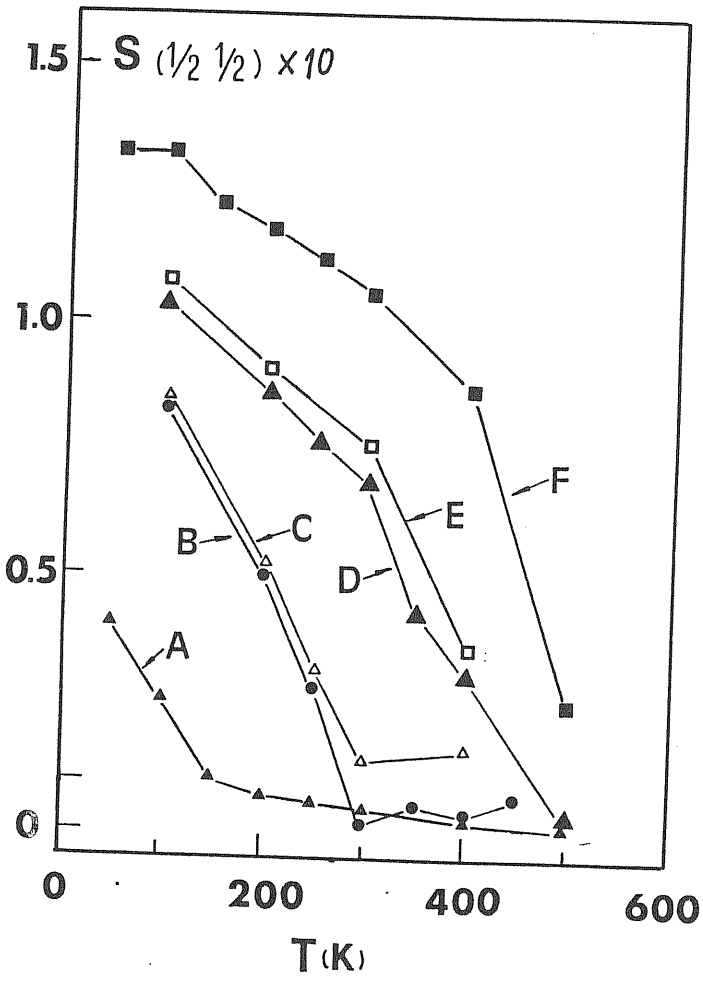

Fig.6.1 MD results of temperature behaviour of S(1/2,1/2) obtained with several different choice of surface potential parameters as indicated in table 6.1.

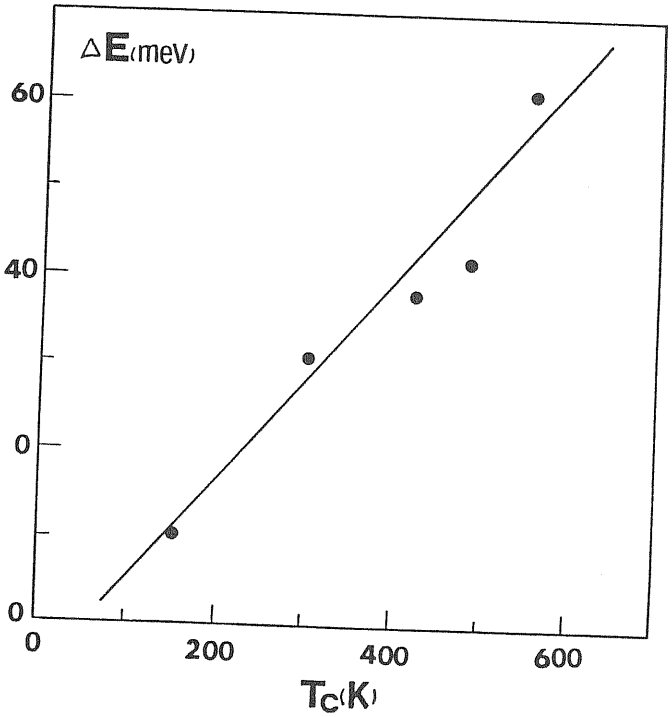

Fig.6.2 c(2x2) reconstruction related energy gain ΔE versus the corresponding transition temperature Tc.

cedure as in the previous chapter, we have in fact carried out the simulations for a 6-layer slab with number of surface atoms n=64, 144, 256 respectively for a square box oriented along <100> and n=128 for a (roughly) square box oriented along <110>. The results from various sizes are similar apart from some size effects as we will discuss in the next section. The result presented below mainly refer to a <110> box with n=128.

The temperature behaviour of the calculated surface structure factor S(kx,ky) for kx=1/2, ky=$\pm$1/2 and the order parameter magnitude $\langle \rho \rangle$ and phase $\langle \cos\varphi \rangle$ as well as the corresponding susceptibilities as defined in the previous chapter are shown in Fig.6.3 and Fig.6.4. One sees that the behaviour of these quantities is very similar to those of Fig.5.1. Again we found the transition to occur through loss of phase coherence. Moreover, the weak structures appearing in S(1/2,1/2) as well as in $\langle \cos\varphi \rangle$ near 250K also suggests existence of the intermediate phases. Although in the present case the intermediate phases have not been studied in great detail as we have done in chapter 5, at least one such a phase between the low temperature c(2x2) and high temperature disordered phase can be detected. This intermediate phase is also incommensurate in nature as directly suggested by S(Kx,Ky) near (1/2,1/2) of Fig.6.5, in which a

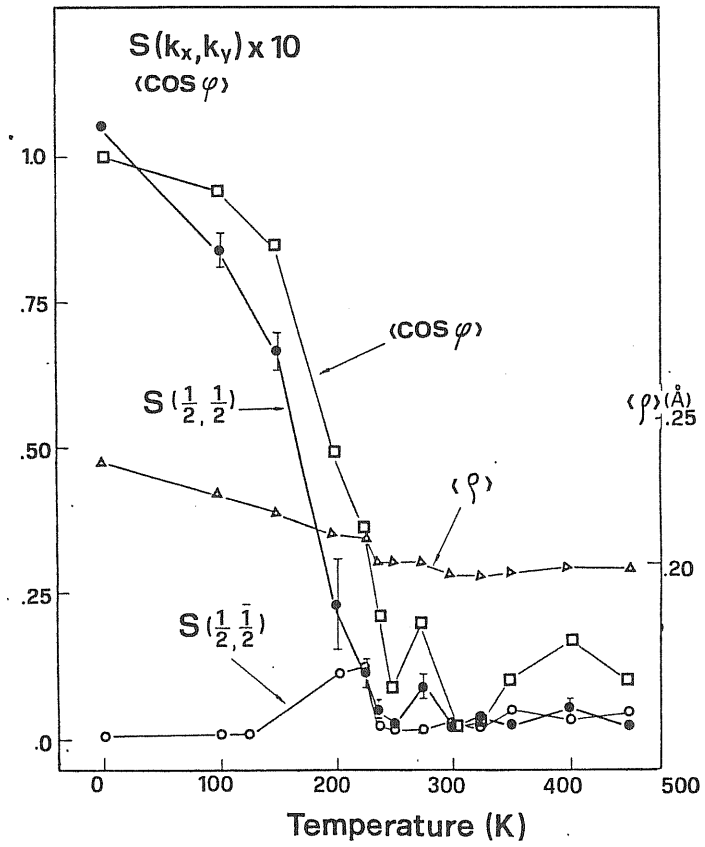

Fig.6.3 Surface structure factor and order parameter f the reconstructed W(001) surface obtained with the urface potential C. The MD sample used for the alculation is <110> oriented with n=128.

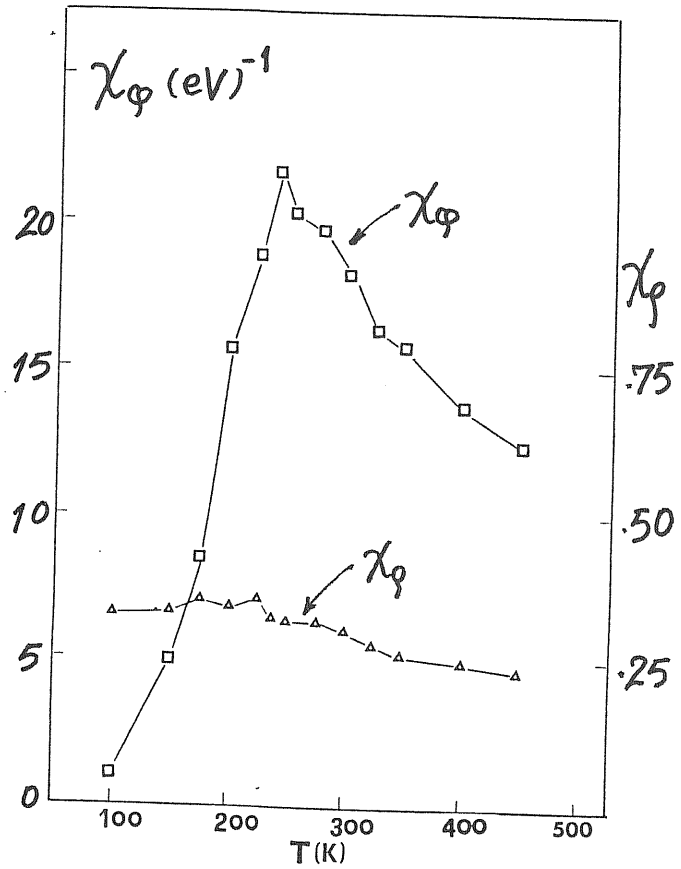

Fig.6.4 The phase and amplitude susceptibilities χ_φ and χ_ρ obtained with the same surface potential and MD sample as used for Fig.6.3.

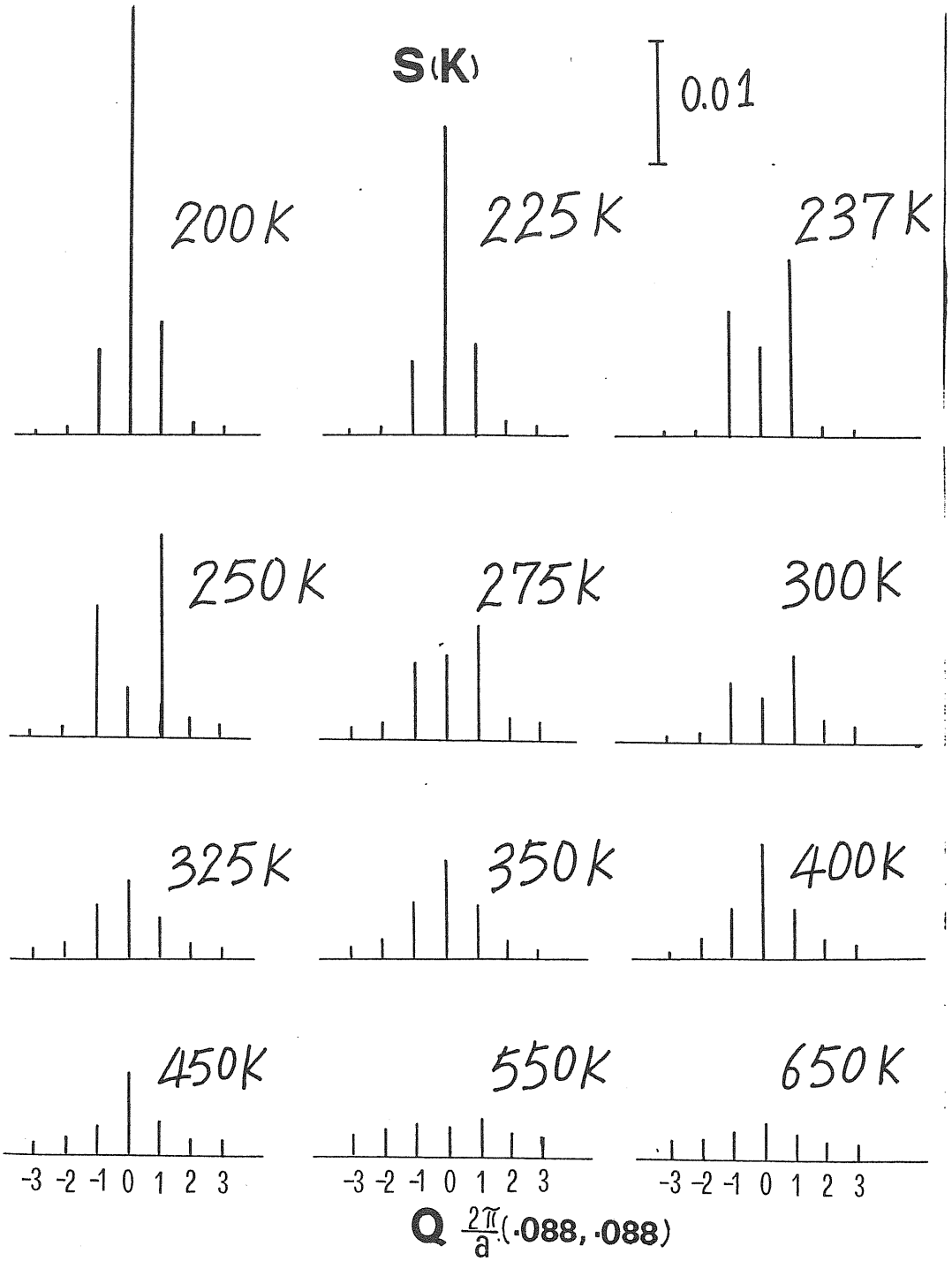

Fig.6.5 Plot of surface structure factor S(K) along about M=$2\pi/a$(1/2,1/2) for virous temperatures. The value of K in S(K) is related to Q by K= KO+Q (KO=2π/a(1/2,1/2). The potential and MD box used is the same as those for Fig.6.3.

splitting of the half order intensity along <110> with $\Delta\vec{K}=2\pi/a$ (0.09,0.09) was found near T=237 K. The development of domains and short-range order structure in the critical region can also be seen in the time plot of the surface static structure factor S(Kx,Ky) for Kx=1/2, Ky=1/2 of Fig. 6.6, and the integration S(K) about $K=2\pi/a$ (1/2,1/2) of Fig.6.7. These two figures are also very similar to the ones we have seen in the previous chapter. This again indicates that the essential features of the two potentials are the same even if their harmonic parameters are different. In fact, our choice of α_s, β_s for the surface potential B and C are just lying on the dashed line inside the M_5 region of Fig.1.19. The $(\alpha_s+\beta_s)$ along this line is a constant. As it has been pointed by Fasolino and Tosatti /43/, the choice of α_s and β_s along this line will basically all yield reasonable distortion features since $\omega_5 \propto \alpha_s+\beta_s$. However, for α_s more negative, the system becomes prone to vertical(M_1) distortions, a tendence which disappears as α_s increases. Since the in-plane distortion picture for the W(001) surface reconstruction is now well-established /5-8,32/, we would conclude that the surface potential B is more plausible for representing the W(001) surface than the surface potential C.

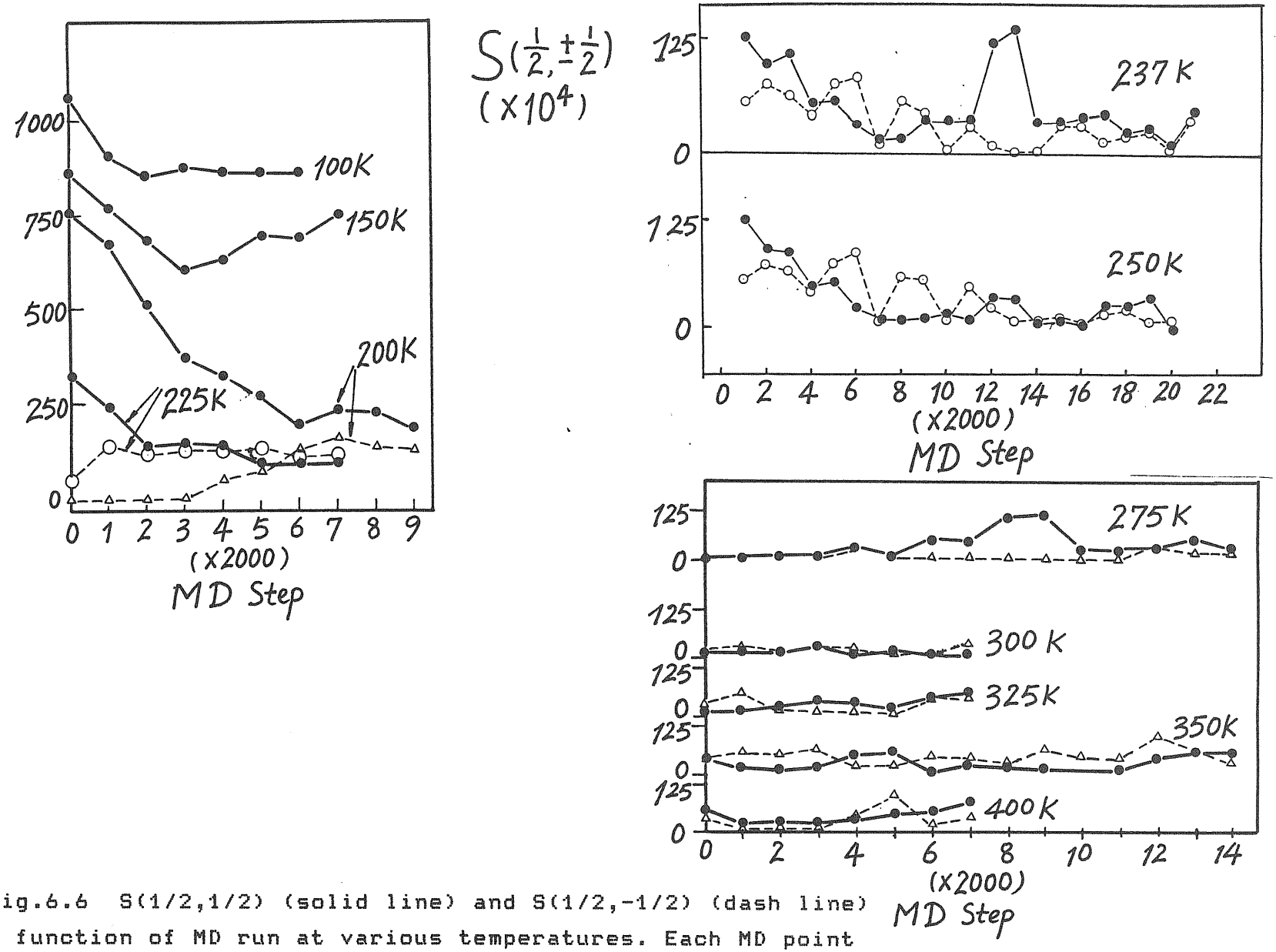

Fig.6.6 S(1/2,1/2) (solid line) and S(1/2,-1/2) (dash line) as a function of MD run at various temperatures. Each MD point consists of 2000 MD steps averaging. The potential and the MD box is the same as those used for Fig.6.3.

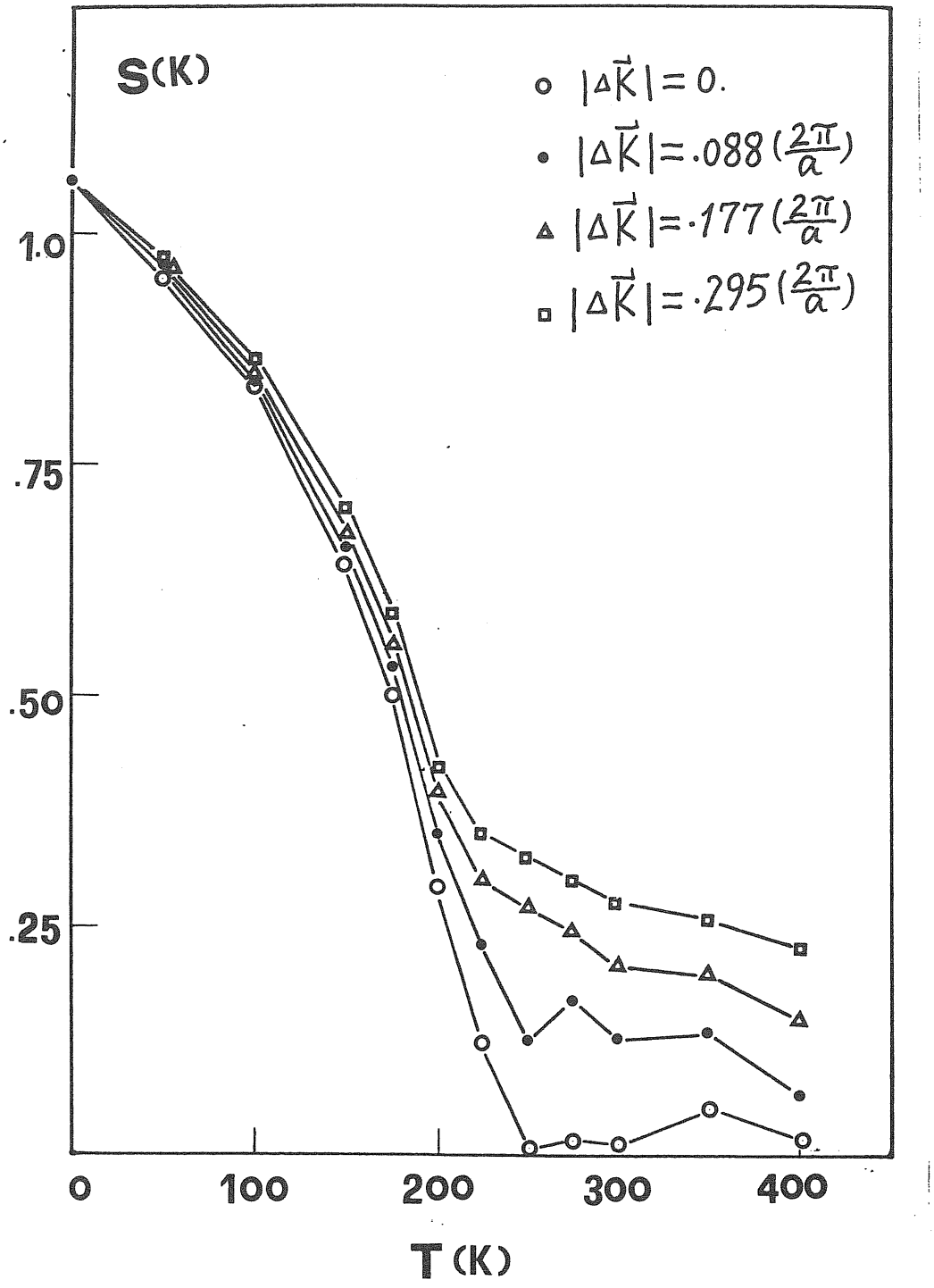

Fig 6.7 The integrated surface structure factor S(Kx,Ky) near Kx=Ky=1/2 obtained with surface potential C and a <100> box with n=256. The values of S(K) are the sum of S(Kx,Ky) over all K points within a circle of radius $|\Delta K|$ and centred at K =2π/a(1/2,1/2), respectively.

6.3 On the dependence of MD 'box'

A) Choice of slab thickness

In the present simulation of surface reconstruction, the periodic boundary conditions apply only on the X-Y plane while a sufficient slab thickness is required to decouple the two surfaces. In order to choose an optimum slab thickness for the present study, we have carried out the MD simulation for a 8x8 slab of 8, 6 and 4 layers of thickness respectively, with the surface potential imposed only on the upper surface, while leaving the interaction for the lower surface the same as in the bulk. By imposing the potential in this way, the lower surface was found to keep the (1x1) bulk termination while the upper surface is reconstructed as shown in Fig.6.8, where the surface pair correlation functions $g_S(r)$ of the upper and lower surface at T=100 K are shown for the 8, 6 and 4 layer slabs respectively. In Fig.6.9, we have also plotted out the layer energy E_ℓ as well as the layer relaxation ΔZ_ℓ as a function of layer index l. The layer energy E_ℓ is defined as the sum of atomic energy in l^{th} layer, similar to that of (5.9); the relaxation ΔZ_ℓ is the averaged Z-component of the lth layer atoms with respect to their ideal bulk positions. From the surface pair correlation of Fig.6.8, it seems that the four-layer thickness slab with bulk potential on the lower surface is already good for the study. However, since we want to simu-

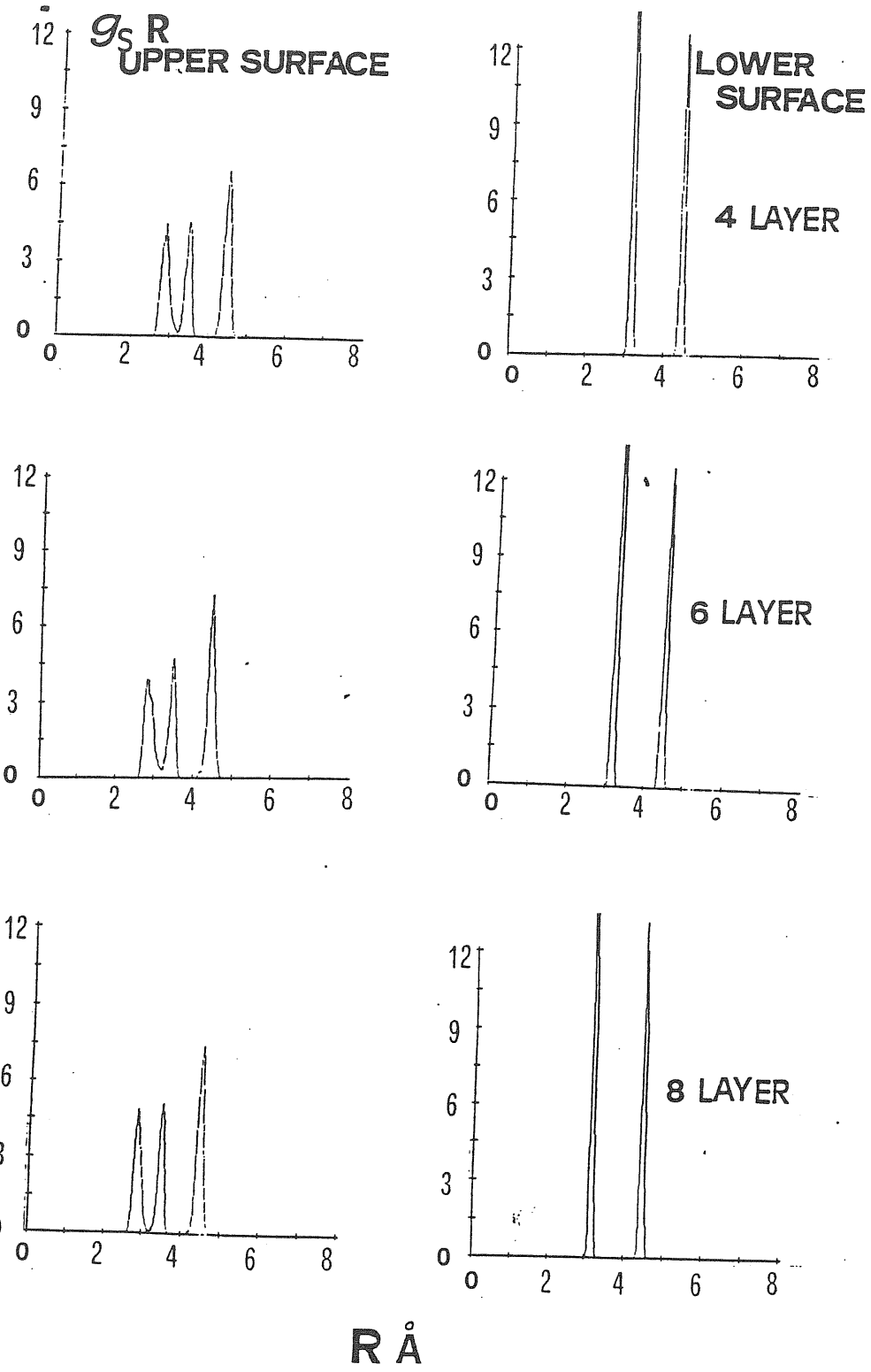

Fig.6.8 Surface pair-correlation functions of the upper and lower surfaces of the four layer, six layer and eight layer slabs.

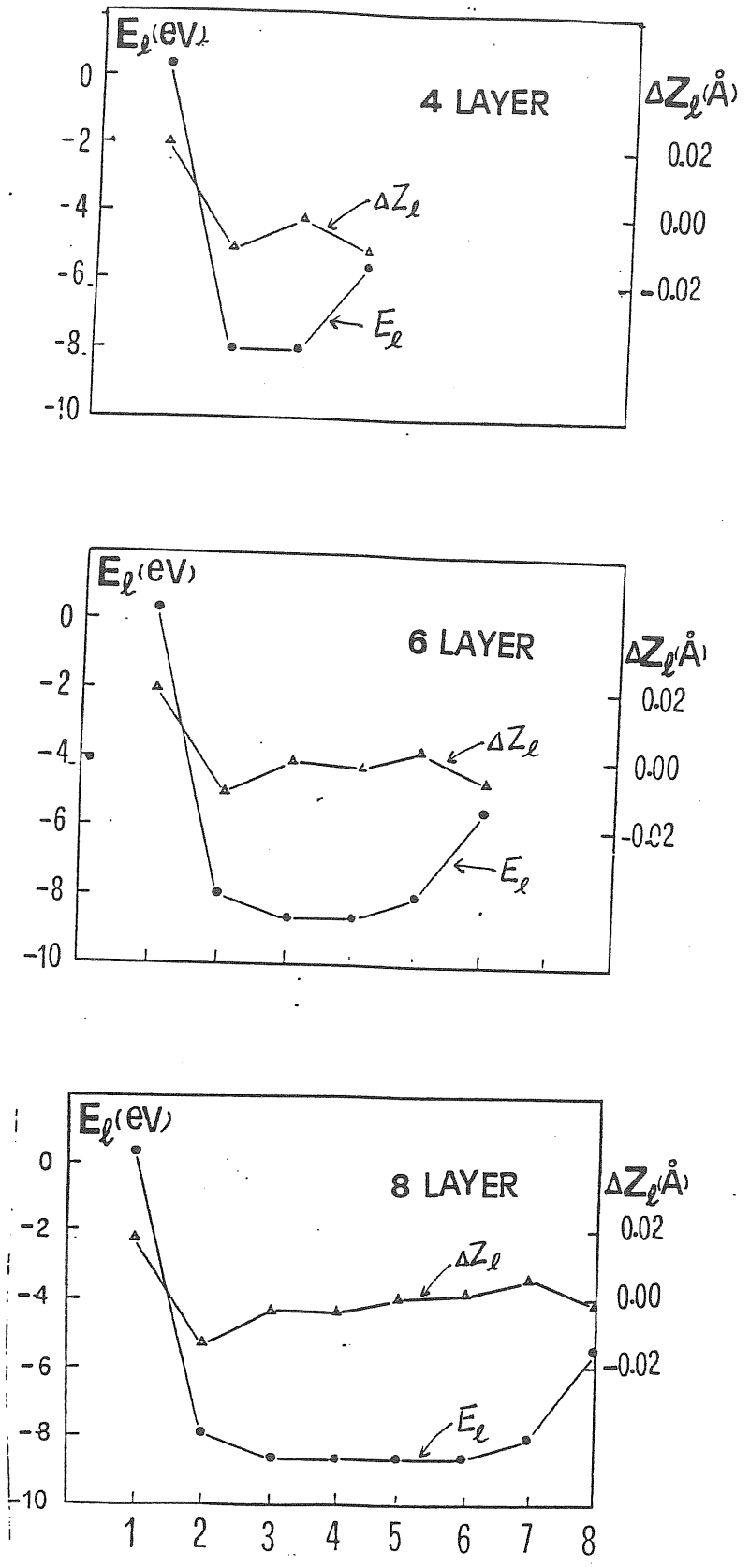

Fig.6.9 Layer energy E_ℓ and relaxation ΔZ_ℓ as a function of layer number for 4-layer and 6-layer and 8-layer slabs respectively, l=1 corresponding to the upper surface layer.

late the surface of a semi-infinite crystal, it is natural to require some bulk-like layers to exist between the two surfaces of the slab. As one sees from Fig.6.9 none such bulk-like layers are found in a 4-layer slab from the layer energy point of view. On the other hand, in a 6-layer slab, two layers (layer 3 and layer 4) can be reasonabely considered as bulk-layers. Moreover, at least up to four layers from the surface, the situation of the 6-layer slab is very similar to that of the 8-layer slab indicating that the 6-layer of thickness is sufficient for the present simulation study.

B) Surface size effects

The second question concerns how large the surface size should be in order to be adequate for the present study of the phase transitions. Obviously, in order to minimize the effects of periodic boundary conditions, the size is required to be larger than the coherence length of the system. In practice this condition is impossible to satisfy once the system is at the critical point, since then the coherence length is diverging. However, as long as we are not attempting to deal with the critical phenomena directly, a sufficient choice of size is possibleto allow us to study the phase transition properties near the critical point. In Fig.6.10 and Fig.6.11, we have compared the temperature

behaviour of S(1/2,$\pm$1/2) from three different size of samples. The number of atoms per layer are n=64, 144, 256 respectively and the boxes are oriented all along <100>. Fig.6.10 is corresponding to the potentials used in the chapter 5, while Fig.6.11 is obtained by using the potential C of previous section. Clearly, the results from a 12x12 surface (n=144) are found to be not very different from the ones of a 16x16 surface (n=256). Size as large as 12x12 seems to be sufficient for the present study of W(001) surface reconstruction phase transition provided we are not attempting to extract the critical exponents directly.

In the W(001) clean surface reconstruction, four types of c(2x2) domains with distortion along <110>, <$\bar{1}\bar{1}$0>, <1$\bar{1}$0> and <$\bar{1}$10> are energetically equivalent. As the phase transition temperature is approached, the surface will wander between these states. For any finite size sample, it is expected that this wandering behaviour will start somewhat before the critical temperature Tc is reached. Such effects can be seen from the plot of S(1/2,$\pm$1/2) as function of each MD run (i.e., of each 2000 MD steps in the present case) as shown for a <110> box with n=288 and n=128 in Fig.5.8 and Fig.6.6 and for a <100> box with n=64,144,256 in Fig.6.12 and Fig.6.13 respectively. There S(1/2,1/2) and S(1/2,-1/2) characterize the domains with distortion along the <110> (or

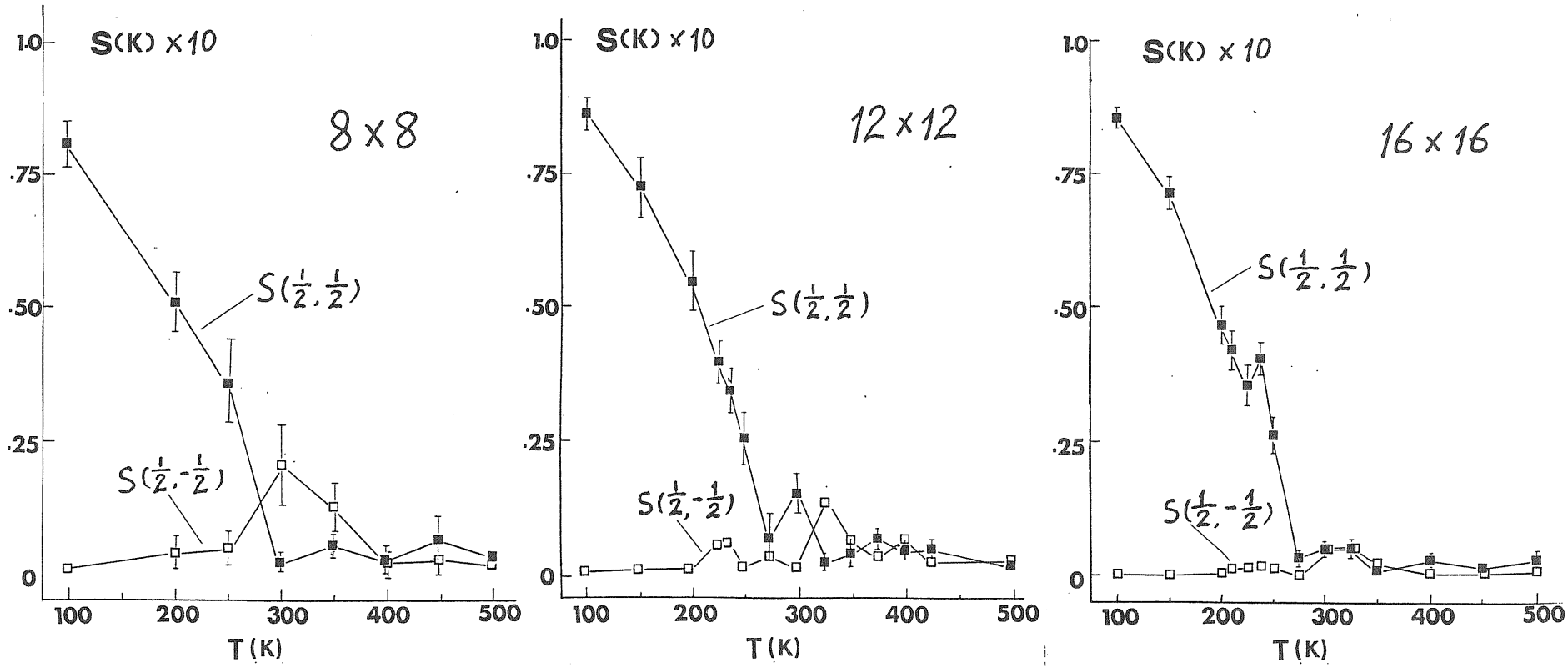

Fig.6.10 Temperature behaviour of S(1/2, ±1/2) from three different size of 6-layer slabs with surface potential B. The size of the surface are (a). n=64 (8x8), (b). n=144 (12x12) and (c). n=256 (16x16). The MD box is oriented along <100>.

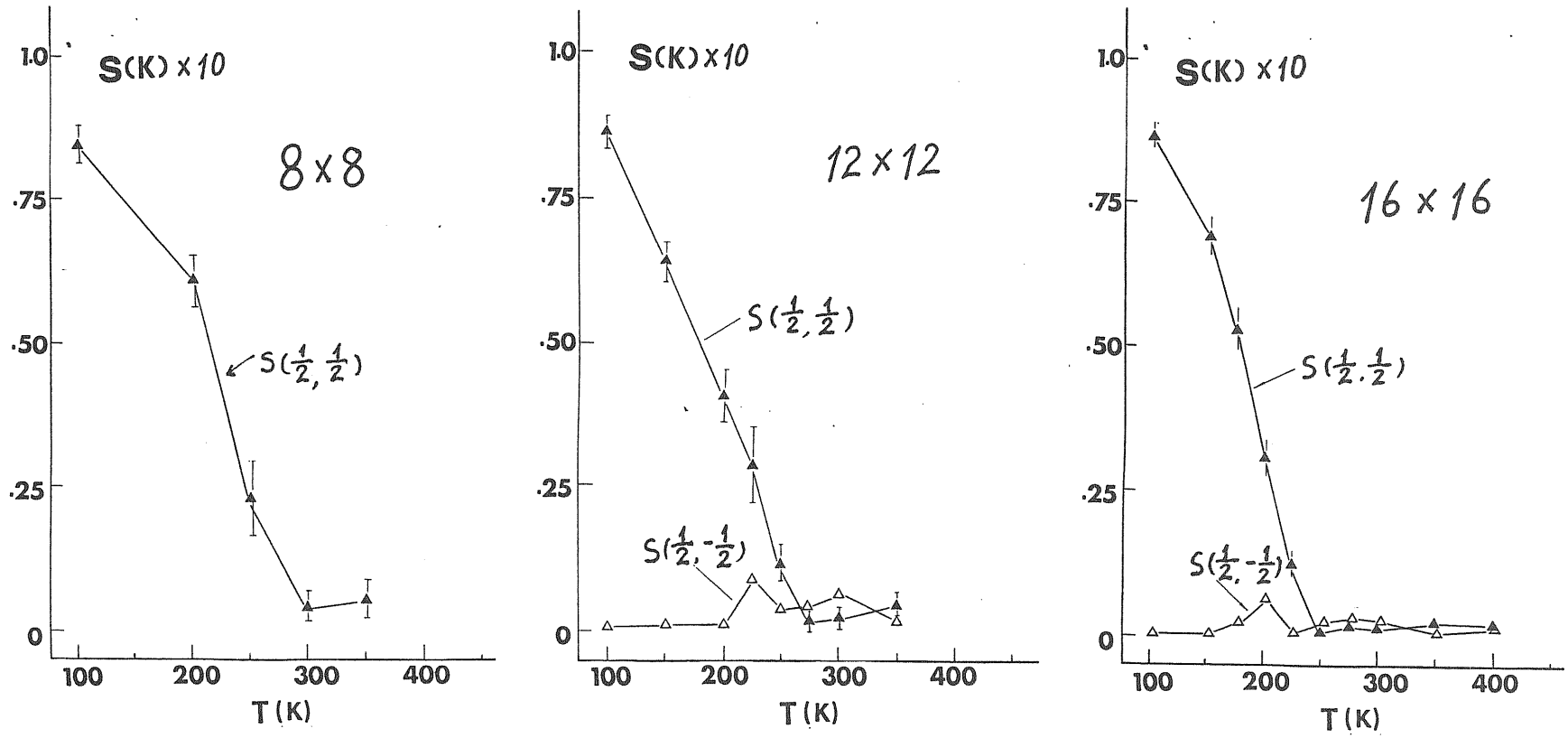

Fig.6.11 Temperature behaviour of S(1/2, ±1/2) from three different size of 6-layer slabs with surface potential C. The size of the surface are (a). n=64 (8x8), (b). n=144 (12x12) and (c). n=256 (16x16). The MD box is oriented along <100>.

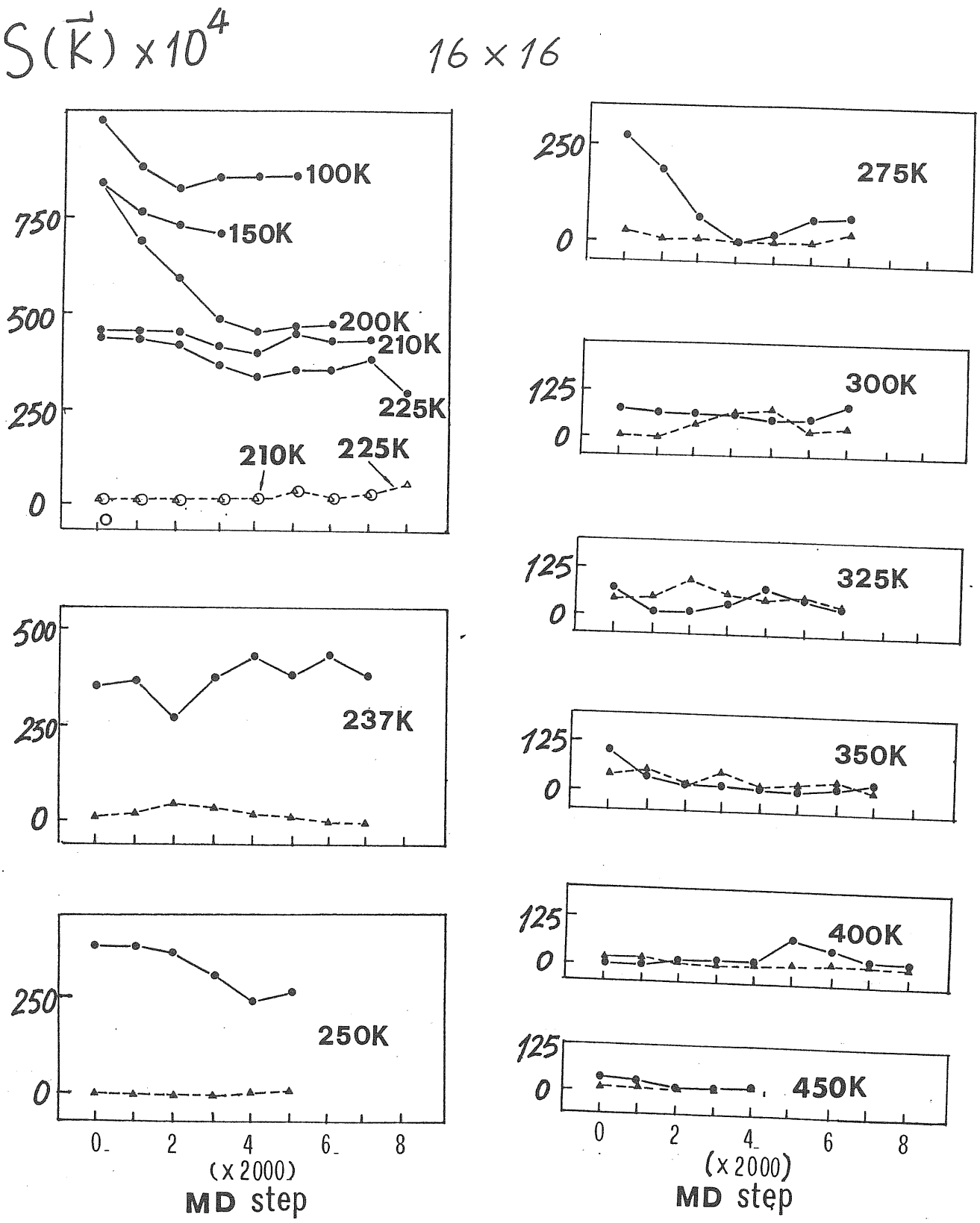

Fig.6.12 S(1/2,1/2) (solid line) and S(1/2,-1/2) (dash line) as a function of MD run at various temperatures. Each MD point consists of 2000 MD steps averaging. The surface size is 16x16.

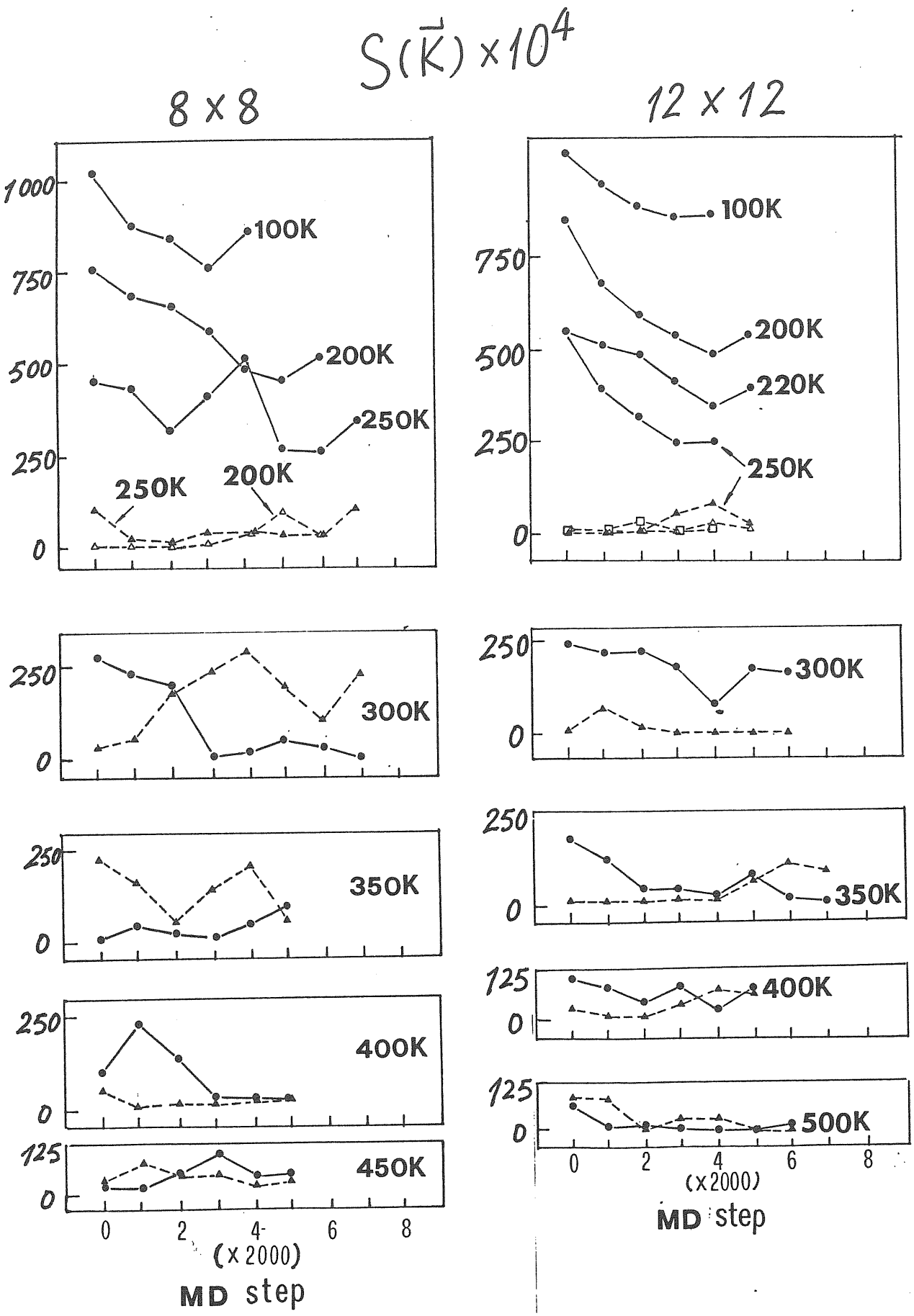

Fig.6.13 S(1/2,1/2) (solid line) and S(1/2,-1/2) (dash line) as a function of MD run at various temperatures. Each MD point consists of 2000 MD steps averaging. The surface sizes are 8x8 and 12x12 respectively.

$\langle\bar{1}\bar{1}0\rangle$) direction and along the $\langle 1\bar{1}0\rangle$ (or $\langle\bar{1}10\rangle$) direction respectively. At low temperature T=100K, for example, only one type of domains is present on the surface ($S(1/2,1/2)\neq 0$, $S(1/2,-1/2)\approx 0$) regardless of the size. When the temperature is increased, two types of domains show up, S(1/2,1/2) and S(1/2,-1/2) begin to cross each other. The appearance of domains is found to occur relatively earlyer in a smaller sample. For example, in a sample with n=64 and n=128 two type of domains begin to show up below T=200 K, while for a larger sample of n=288 the domain flipping is found to be near $T\sim 250K$, very close to the critical temperature.

C) Box orientation effects

As we have previously pointed out, the MD results for the W(001) surface reconstruction phase transition presented in the previous chapter was based on a particular choice of MD box with orientation along <110> direction and with surface atoms n=288. In fact, we have also carried out a simulation for a <100> box with n=256. Some MD results from those two different orientations of MD box are compared in Fig.6.14, Fig.6.15 and Fig.6.16. One sees that all phases obtained from the <110> box can also be identified from the results of the <100> box but one of the intermediate phases, i.e., the phase F_B. In particular, while three peaks in the

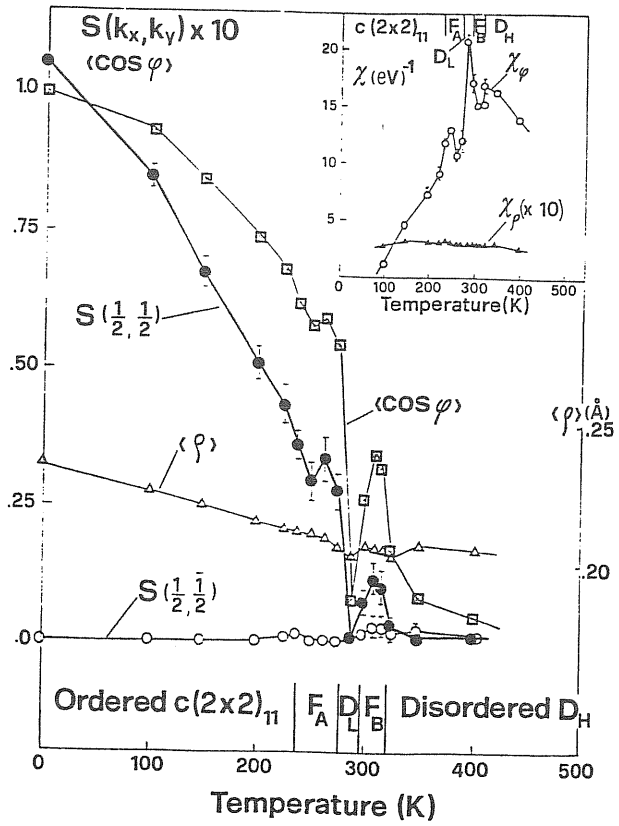

(a)

⟨110⟩ box

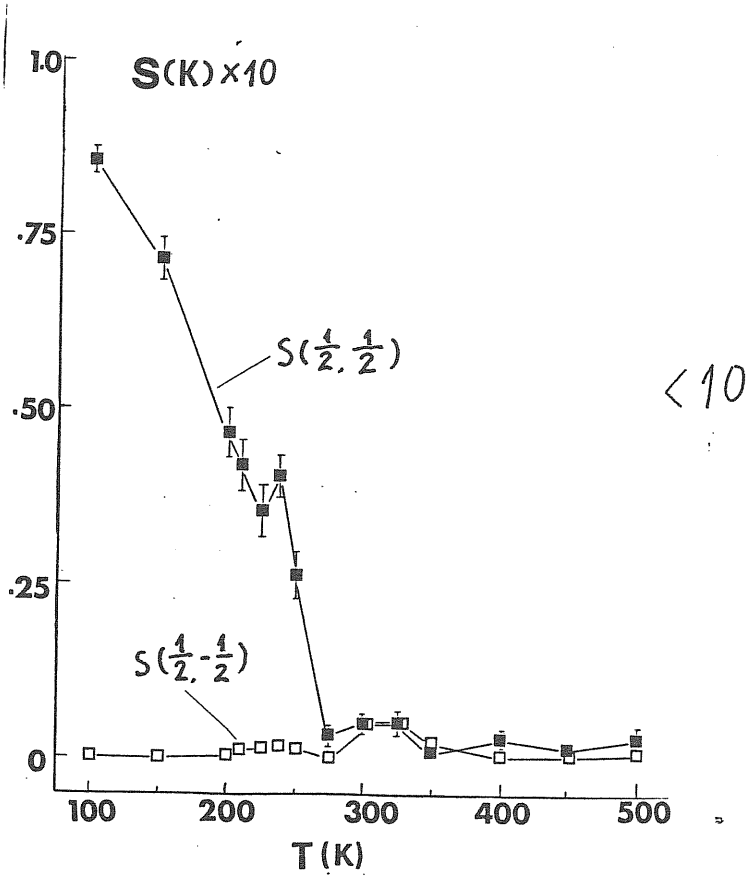

(b)

⟨100⟩ box

Fig.6.14 Comparison between temperature behaviour of S(1/2, ± 1/2) obtained with a ⟨110⟩ box and a ⟨100⟩ box. The surface potential B has been used.

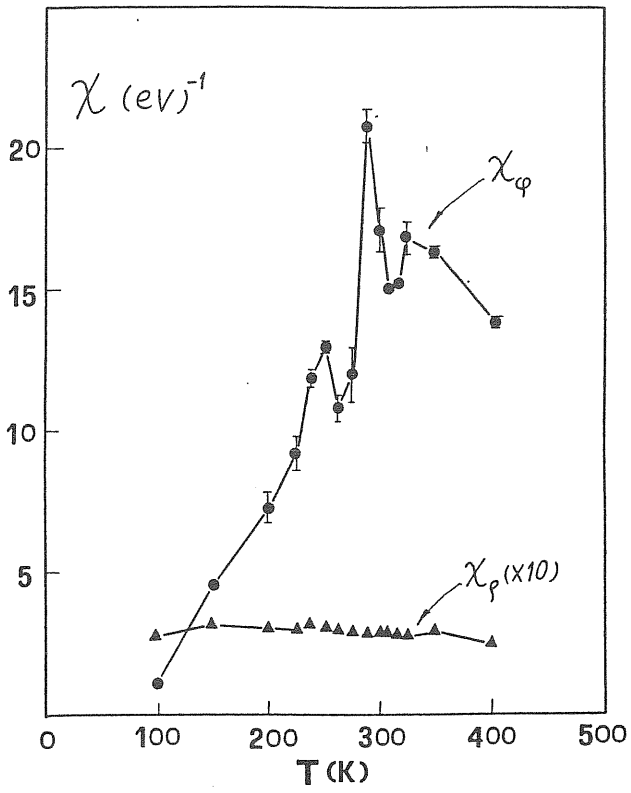

(a)

<110> box

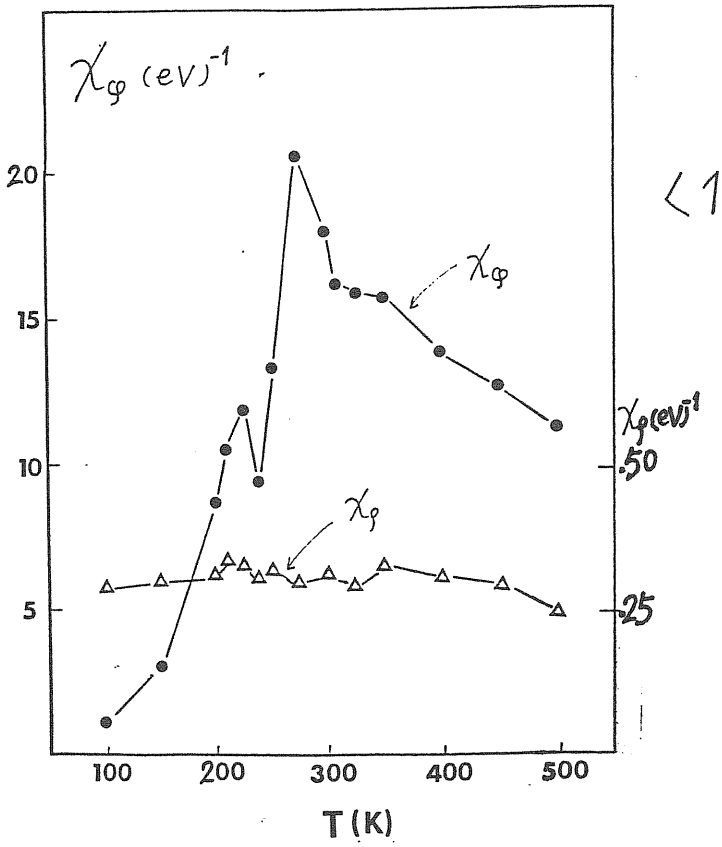

(b)

<100> box

Fig.6.15 Comparison between the susceptibilities obtained with a <110> box and a <100> box. The surface potential B has been used.

(a)

<110> box

(b)

<100> box

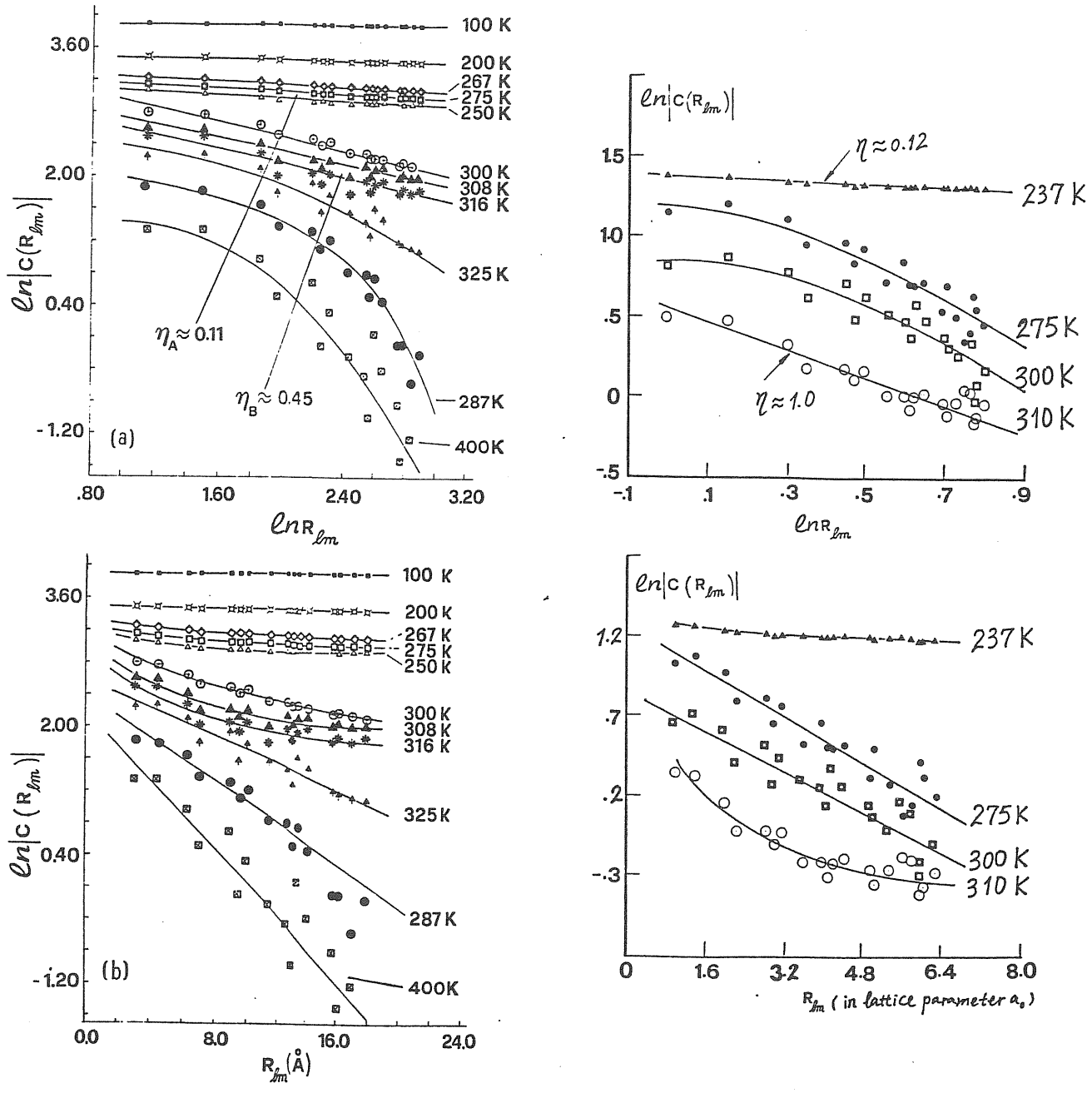

Fig.6.16 Comparison between the surface spatial correlations obtained with a <110> box and a <100> box. The surface potential B has been used.

phase susceptibility χ_φ clearly show up in the <110> box, the third peak at T$\sim$320K has been smeared to a shoulder in the <100> box (see Fig.6.15). At the same time, the surface spatial correlation $C(R_{\ell m})$ in that temperature range (T$\sim$310 K in Fig.6.16b) shows a power-law decay but with a larger exponents ($\eta \approx 1.0$ instead $\eta \approx 0.45$ in the case of <110> box). It seems that the phase F_B in the <100> box is a mixture between power-law and exponential decay behaviour. Another example of the box orientation effects is shown in Fig.6.17, in which we have compared the surface structure factor S(K) near K= $2\pi/a$ (1/2,1/2) for a <110> box with n=128 and for a <100> box with n=144 by using the surface potential C. It is clear that the incommensurate splitting of the half order spots is more evident in the <110> box than that in the <100> box.

In the present MD simulation, the periodic boundary conditions are applied along X ad Y directions. For a square MD box with a <100> orientation the periodic boundary conditions will generate an infinite slab along <100> and <010>. On the other hand, if the MD box has a <110> orientation, the infinite slab is generated along <110> and <1$\bar{1}$0> by the periodic boundary condition. It seems that the two type of 'box' orientations are equivalent if they are used to simulate the ordered or disordered structure. However, if there

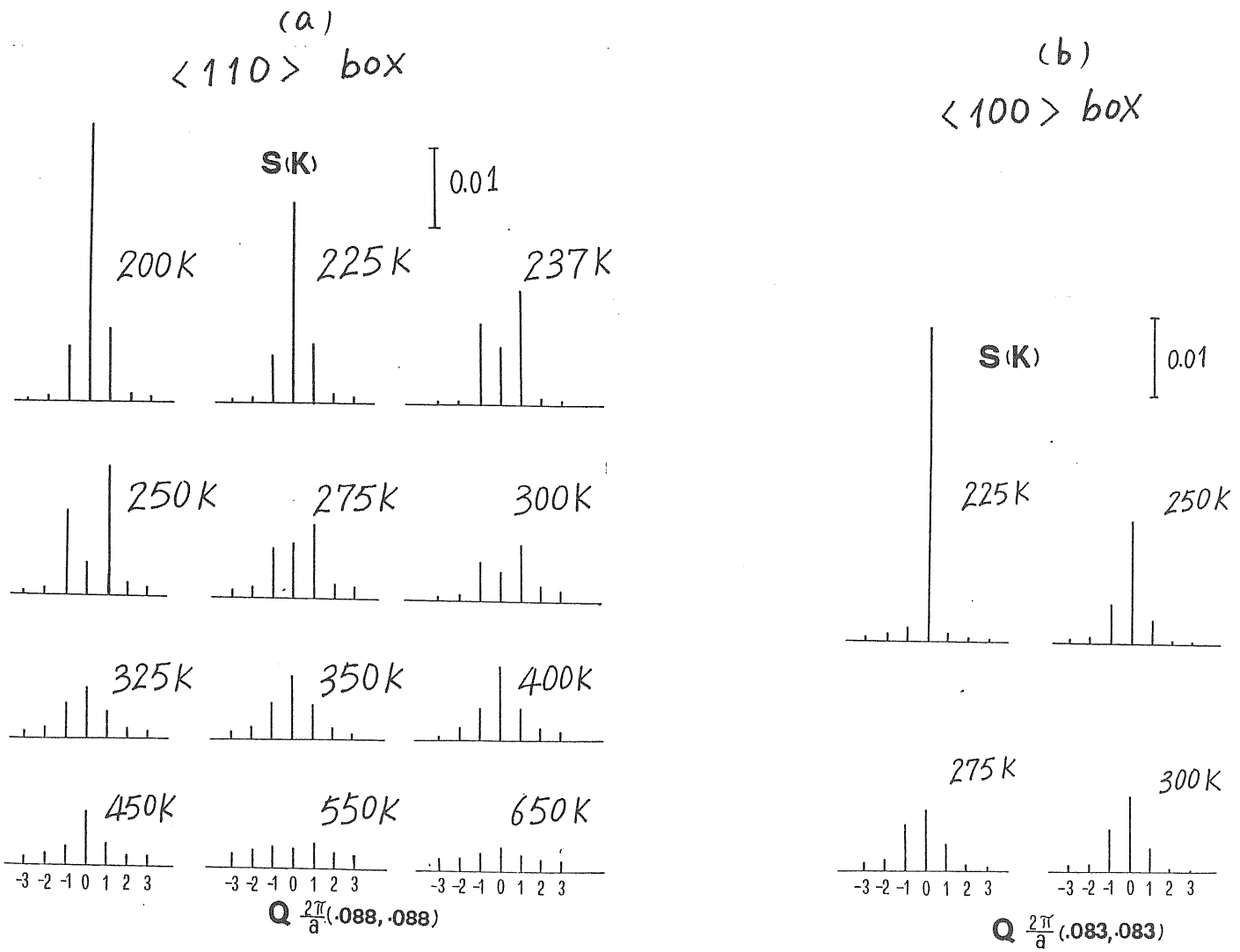

Fig.6.17 Comparison between the incommensurate splitting of S(Kx,Ky) obtained with a <110> box and a <100> box. The surface potential C has been used.

are diluted domains and walls with preferred orientation present in the system, the two different orientations of the MD box may exhibit very different effects. In particular, for a relatively small box, the domain walls will generally be locked into the box. Those domains with wall parallel to the edge of the box will be encouraged while the ones with walls inconsistent with the orientation of the box will be suppressed. We have checked this point as shown in Fig.6.18 and Fig.6.19. In Fig.6.18 we have compared the surface atomic displacement field from a <110> box with n=288 and a <100> box with n=256 respectively, using the surface potential with parameters α_S=-0.75 eV/A , β_S=-0.94 eV/A, γ_S=3.76 eV/A , and δ_S=150.0 eV/A . The domains with wall parallel to the edge of the box are detectable in Fig.6.18a for the <110> box, but in the <100> box such domain walls have been smeared out. However, if the domain walls are dense enough, the domains will be less affected by the boundary of the box. This feature is shown in Fig.6.19 in which the dense domain walls parallel to <110> direction can be seen in both orientations of the box.

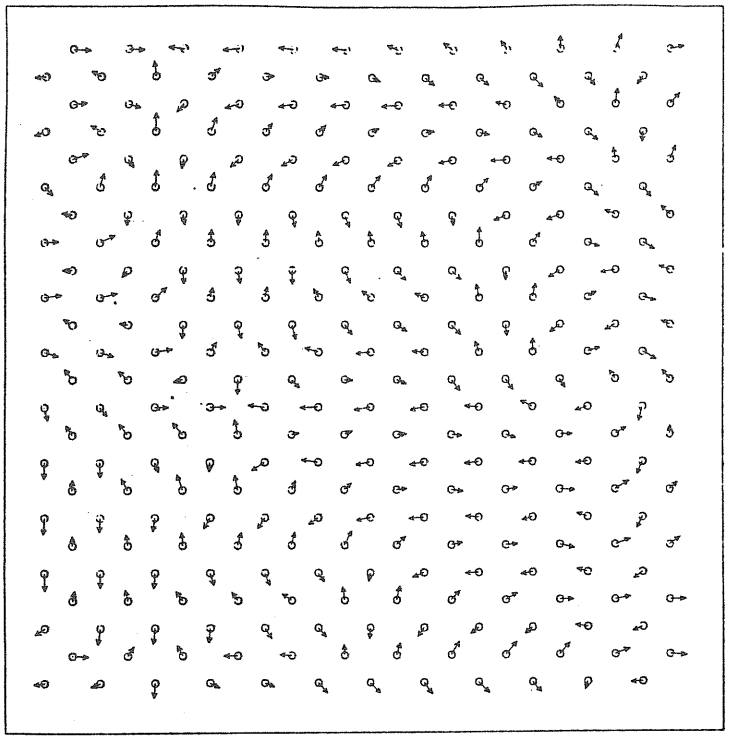

(a)

<110> box

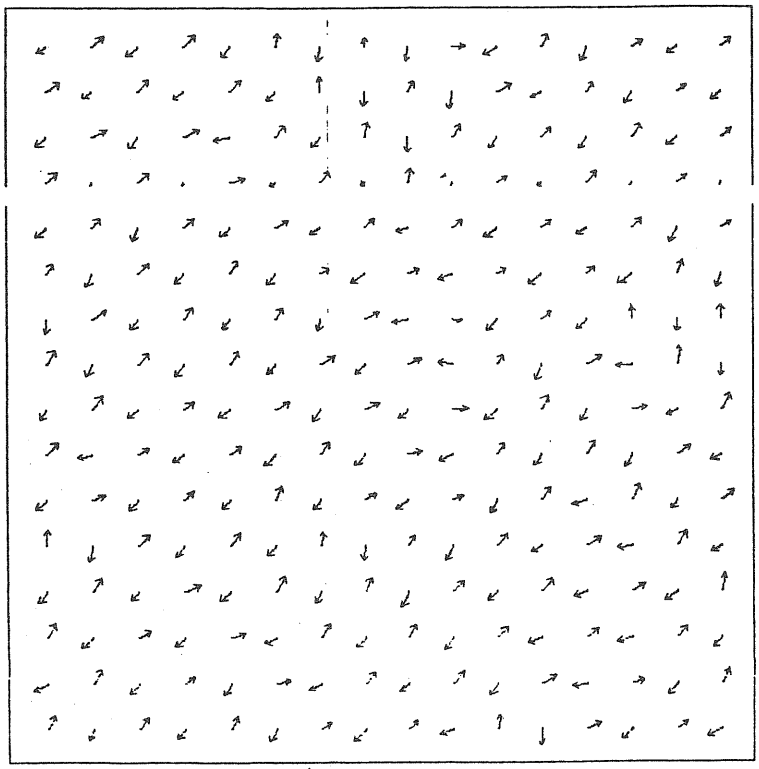

(b)

<100> box

Fig.6.18 Surface atomic displacement field obtained with a <110> box and a <100> box using surface potential parameters α_S=-0.75 eV/Å^2, β_S=-0.94 eV/Å^2, γ_S=3.76 ev/Å^2 and δ_S=150.0 eV/Å^2.

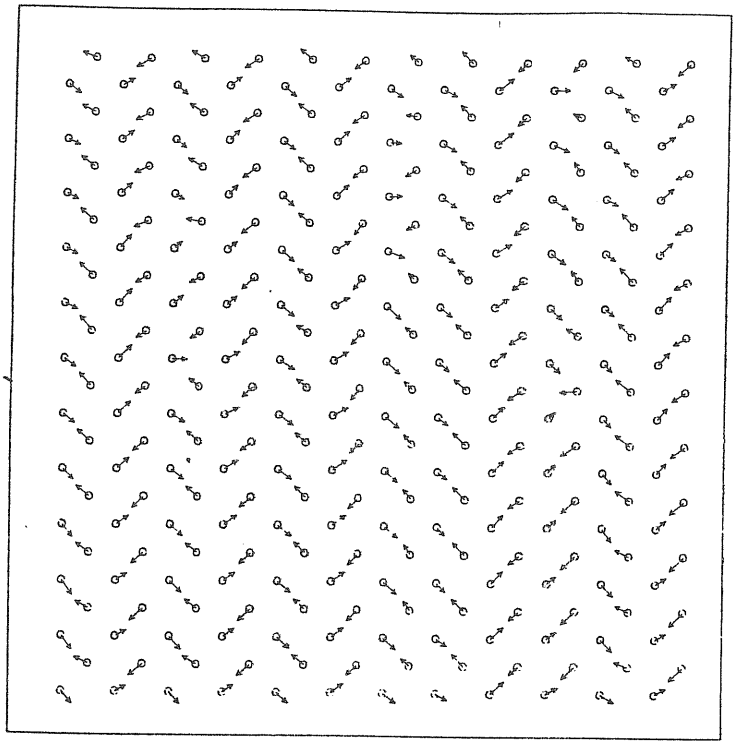

(a)

<110> box

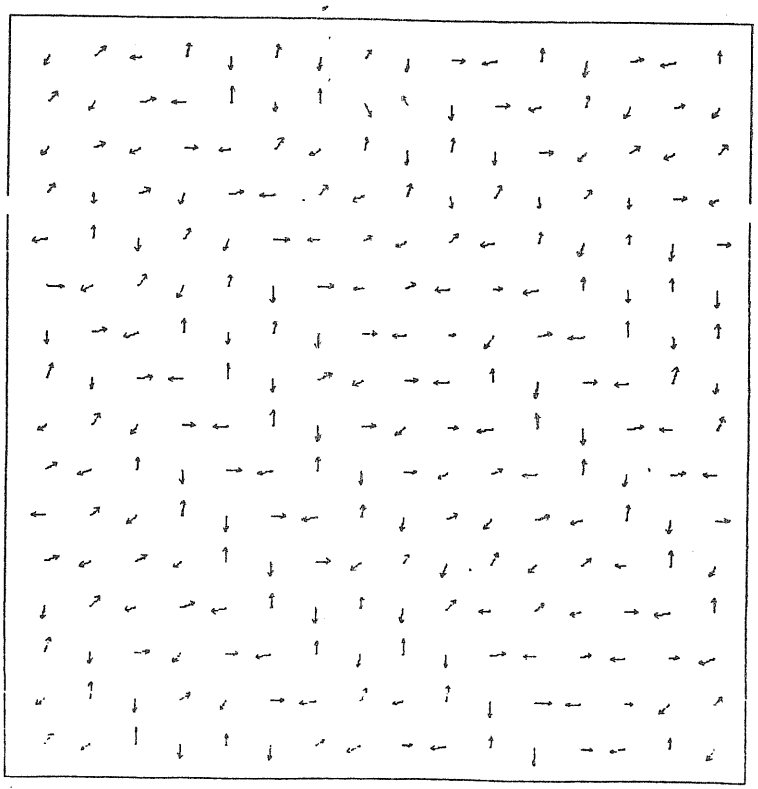

(b)

<100> box

Fig.6.19 Surface atomic displacement field obtained with a <110> box and a <100> box using surface potential parameters α_s=-0.75 eV/Å^2, β_s=-0.94 eV/Å^2, γ_s=6.0 eV/Å^2 and δ_s=135.0 eV/Å^2.

chapter 7

Anharmonic surface modes and W(001) surface reconstruction phase transition: Soft modes or not?

7.1 Introduction

One of the attractive and important aspect of displacive structural phase transitions is the study of phonons across the transition, particularly because of phonon softening, a concept introduced by Cochran and by Anderson on the basis of mean field theory /90,100/. According to the soft mode picture, the limit of stability of a crystal lattice is approached as the frequency of any one mode decreases and approaches zero, because once the atoms are displaced in the course of that particular vibration, there is no harmonic restoring force to return them to their original positions. Hence, they assume new equilibrium positions determined by the symmetry (eigenvector) of this soft mode, and by anharmonic restoring forces.

It has been clear for a long time, however, that below four dimensions large deviations from the mean field theory do occur, both in critical behaviour and in dynamics. Phonon softening remains well-defined only in some systems characterized by strongly displacive behaviour. In a majority of other systems there hardly is any softening, and the critical region is dominated by order-disorder behavior /60,65-

70,101/. In such cases large broadening occurs in the phonon density of states instead of softening.

In general, any given structural transition is expected to fall somewhere between the displacive and the order-disorder limits without any clear line to divide sharply between the two situations. Besides, even in a displacive system, the fluctuation will eventually develop an order-disorder character,i.e., clusters or domains, very close to the critical point. There, the conventional soft-mode picture becomes inadequate for describing the dynamics of the system /60,65-70,101/.

In this chapter we address this question for the surface reconstruction transition of clean W(001). In order to test the soft phonon picture, we have implicitly assumed here by describing the reconstructed W(001) surface with parameters that yield a soft M_5 phonon on the ideal (1x1) surface /43/. In the first place, it is expected that the fluctuations will of course be more crucial in two dimensional than in three-dimensional systems. Secondly, it is of interest to locate this phase transition between the two limits discussed above. Our results on the 'soft-modes' of the reconstructed W(001) surface in fact does show only a modest amount of softening. Their mean frequency dose not go all the way to zero at the transition. Instead, a large broaden-

ing of the phonon spectral peak occurs as the transition is approached, indicating strong order-disorder behavior setting in approximately at 0.5 Tc.

In the next section, we will describe the method used for the present calculation. The results will presented in Sec. 7.3 together with some brief discussion.

7.2 The method

We compute the temperature-dependent surface phonons of the reconstructed W(001) surface with an MD sample formed by arranging 1536 particles in 6-layer bcc(001) slab with 256 atoms per layer to fill a square box oriented along <100>. The periodic boundary conditions are used along the x and y directions, but not along z.

With the effective lattice hamiltonian and the pairwise potentials $V^B(R)$ and $V^S(R)$ developed in chapter 4 and used in chapter 5, a standard MD simulation was carried out. The N(=1536) coupled Newton's equations of motion were solved by a fifth-order predictor-corrector algorithm. Once the positions and velocities of all particles are known as a function of time, the phonon spectral intensity is evaluated through the velocity autocorrelation function <V(t),V(0)>

$$g(k,\omega) = \int_{-\infty}^{\infty} dt \sum_n e^{i\omega t} e^{i\vec{k}\cdot\vec{R}_n} \left[\frac{\langle V_n(t)\, V_n(0)\rangle}{\langle V_n(0)\, V_n(0)\rangle} \right] \quad (7.1)$$

with

$$\langle V_n(t) V_n(0) \rangle = \frac{1}{NM} \sum_{m=1}^{M} \sum_{n=1}^{N} V_n(t+\tau_m) V_n(\tau_m) \qquad (7.2)$$

where M is the number of MD steps and N is the number of particles respectively used in the average.

In principle, it would not be difficult to do a full surface phonon spectrum at all k-vectors through (7.1)-(7.2) in the course of MD simulation. However, the full computation is very time consuming. In the present work we have chosen to concentrate only on those particular modes that are believed to be relevant to the reconstruction phase transition. The T=0 surface phonon study of Fasolino and Tosatti(FT)/43/, clearly suggests that such modes are the zone centre optical surface modes. Hence our choice is for the present time to restrict ourselves to k=0. At k=0, three low-lying optical surface mode (or resonances) of the reconstructed (001) surface are expected. They derive from the zone folding of the twofold M5 (in-plane) and M1 (vertical) modes of the ideal (1x1) surface at the point $M=2\pi/a(1/2,1/2)$. Such modes have, as described in detail by FST/39/, FT/43/, eigenvectors corresponding to a longitudinal mainly in-plane 'amplitude' mode ω_L, a mainly vertical mode ω_Z and a transverse or more correctly a shear horizontal 'phase' mode ω_T. Higher frequency modes localized

mostly in the second layer, also found by FT/43/, will be studied separately, and not dealt with explicitly here.

Since the surface distortion decays exponentially into bulk like $e^{-Z/\lambda}$, with $\lambda \approx 1$ Å, the first layer amplitudes and velocities are completely representative of the 2D order parameters and of its dynamics. In order to extract the spectral intensities of each of the k=0 optical modes ω_L ω_T and ω_Z described above, we decomposed the velocity of each surface atom $\vec{v}_i$ into three components according to the approximate eigenvectors of the modes i.e.

$$\vec{v}_i = v_{iL}\,\hat{e}_L + v_{iT}\,\hat{e}_T + v_{iZ}\,\hat{e}_Z \qquad i=1,\ldots Ns \qquad (7.3)$$

where Ns is the number of surface atoms. The form used for the eigenvector are

$$\begin{aligned} \hat{e}_L &= 1/\sqrt{2}\,(1,1,0) \\ \hat{e}_T &= 1/\sqrt{2}\,(1,-1,0) \\ \hat{e}_Z &= (0,0,1) \end{aligned} \qquad (7.4)$$

This form is only approximate because in reality $\hat{e}_L$ has a small Z admixture and, vice versa, $\hat{e}_Z$ has a small L-admixture. This admixture is estimated to be small /43/ and can be neglected for our purposes.

According to (7.1)-(7.2), first we form the (staggered) first-layer averages (k=0)

$$\begin{aligned} V_L(\tau_m) &= \frac{1}{N_S}\sum_{i=1}^{N_S} v_{iL}(\tau_m)\cos(\vec{q}_0\cdot\vec{R}_i^0) \\ V_T(\tau_m) &= 1/N_S \sum_{i=1}^{N_S} v_{iT}(\tau_m)\cos(\vec{q}_0\cdot\vec{R}_i^0) \\ V_Z(\tau_m) &= 1/N_S \sum_{i=1}^{N_S} v_{iZ}(\tau_m)\cos(\vec{q}_0\cdot\vec{R}_i^0) \end{aligned} \qquad (7.5)$$

where $\vec{q}_o = 2\pi/a\,(1/2,1/2)$ and $\vec{R}_i^o$ denote the undistorted surface atom positions. Then the surface phonon spectral density $g(\omega)$ and the corresponding velocity autocorrelation function $f(t)=\langle v(t)v(0)\rangle/\langle v(0)v(0)\rangle$ are evaluated using the fast Fourier transform technique.

For each temperature, after a long period of equilibration (typically about 8000 MD steps with $\Delta t = 3\times10^{-15}$ sec.) a large number ($16384 = 2^{14}$) of MD steps, corresponding to a time of 6×10^{-11} sec. are used for the evaluation of V(t) and hence $g(\omega)$ and f(t). The results of this analysis will be presented in the next section together with some discussions.

7.3 Results and discussion

The k=0 surface phonon spectral density $g(\omega)$ of the reconstruction- related modes ω_L, ω_T and ω_Z and the corresponding velocity autocorrelations f(t) are presented in Fig.7.1 to Fig.7.6 respectively for the temperature ranging from T=100K to 350K.

Before proceeding to discuss the meaning of this dynamical results, we note that the temperature behaviour of the static reconstruction quantities such as order parameter and static structure factor S(kx,ky) previously studied by us in chapter 5, clearly indicate the reconstruction phase transition to take place around Tc=250K. As already commented in

detail in chapter 5 and chapter 6, the transition from the c(2x2) ordered phase to the high temperature disordered phase was found to be driven by phase fluctuations and to occur through a sequence of narrow but well-defined floating phases. In the present chapter we would like to bring the dynamical properties of the phase transitions in connection with the results of Fig.7.1 to Fig.7.6.

1). At low temperature, T=100 for example, the vibration modes described above are all well-defined, with the vibration frequencies given by ω_L=10 meV, ω_T=5 meV and ω_Z=9 meV respectively. These values are very close to that of T=0 slab phonon calculations by Fasolino and Tosatti /43/.

2) Well below the phase transition, the vertical mode ω_Z and the longitudinal mode ω_L are rather harmonic (especially the vertical mode) whereas the shear horizontal (or 'phase') mode ω_T is already very anharmonic,(i.e., damped and noisy as a function of time, which implies a broad ω-spectrum).

3) As the transition temperature is approached, the longitudinal mode becomes anharmonic as well. In contrast, the vertical mode remains harmonic all the way across the phase transition. This behaviour of the modes implies that: a) the surface reconstruction of W(001) involves mainly in-plane distortions, which is consistent with the LEED studies

/5-8/ and our extensive MD simulation (see chapter 5). b) the phase transition is dominated by the instability of the 'phase' mode (as already pointed out by us in chapter 5).

4) The driving 'soft mode' (the 'phase' mode ω_T and (or) the 'amplitude' mode ω_L in the present case) however does not go all the way to zero at the transition temperature (Tc=250K). Instead a dramatic broadening occurs in its spectrum as the transition is approached. This broadening strongly underlines the order-disorder character of the critical region, beginning already at about 100-150K, i.e., close to 0.5 Tc.

5) The k=0 phonon spectrum of the in-plane modes ω_L and ω_T is and remains very broad also above Tc. From this, one can again argue that the surface of W(001) is in a disordered state at higher temperature, rather than in an ordered (1x1) state. This confirms our previous conclusions based on equilibrium properties (see chapter 5). On the other hand the two modes ω_L and ω_T become very similar at $T \gtrsim Tc$ as it would be expected for the ideal 1x1 surface where the two become degenerate partners of M_5. Hence the disorder refers to the phase degree of freedom, i.e., to the direction of deviation of the surface atoms from its ideal position, and not to the magnitude of such distortion which remains finite.

6) The present result is also consistent with the phenomenological Landau picture developed for this phase transition, which assigns a sinusoidal effective potential for the phase degree of freedom /43/. At low temperatures, the system is trapped in one minimum of the sinusoid and a well defined propagating phase mode exists. At high temperatures, the system can slide freely over the potential, and only diffusive modes are possible, as indeed is observed.

In conclusion, we have shown that the conventional 'soft mode' picture is inadequate for describing the W(001) surface reconstruction phase transition near the critical point. In particular, the displacive order-disorder crossover occurs approximately at $T \sim 0.5$ Tc and indicates strong fluctuation effects, which cannot be neglected as done in mean field theory. Moreover, the crossover is found to be caused by the instability of the 'phase' mode ω_T. The disordered phase therefore refer to the phase degree of freedom.

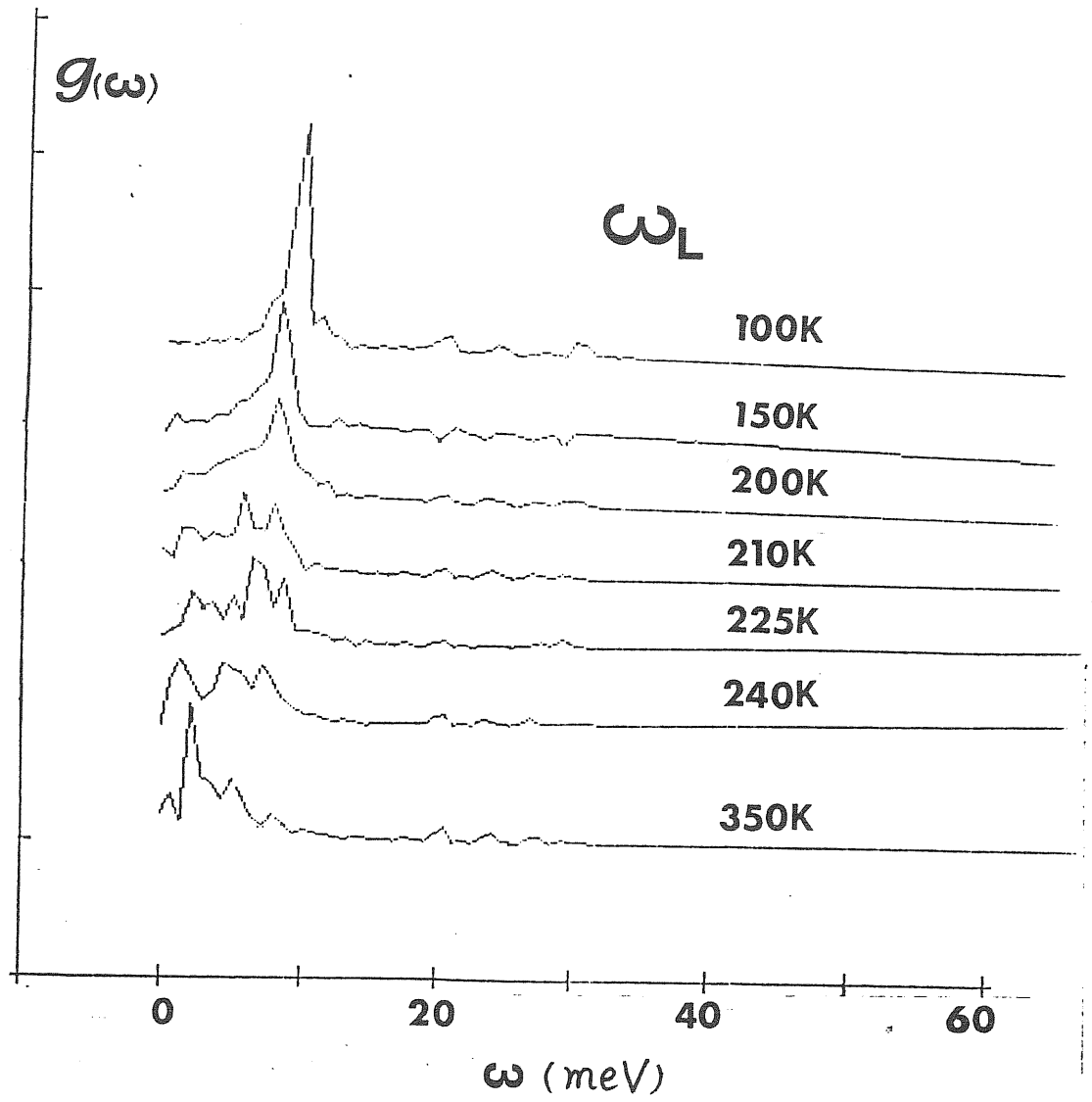

Fig.7.1 Temperature behaviour of the phonon spectral intensity of K=0 'amplitude' mode ω_L of the reconstructed W(001) surface.

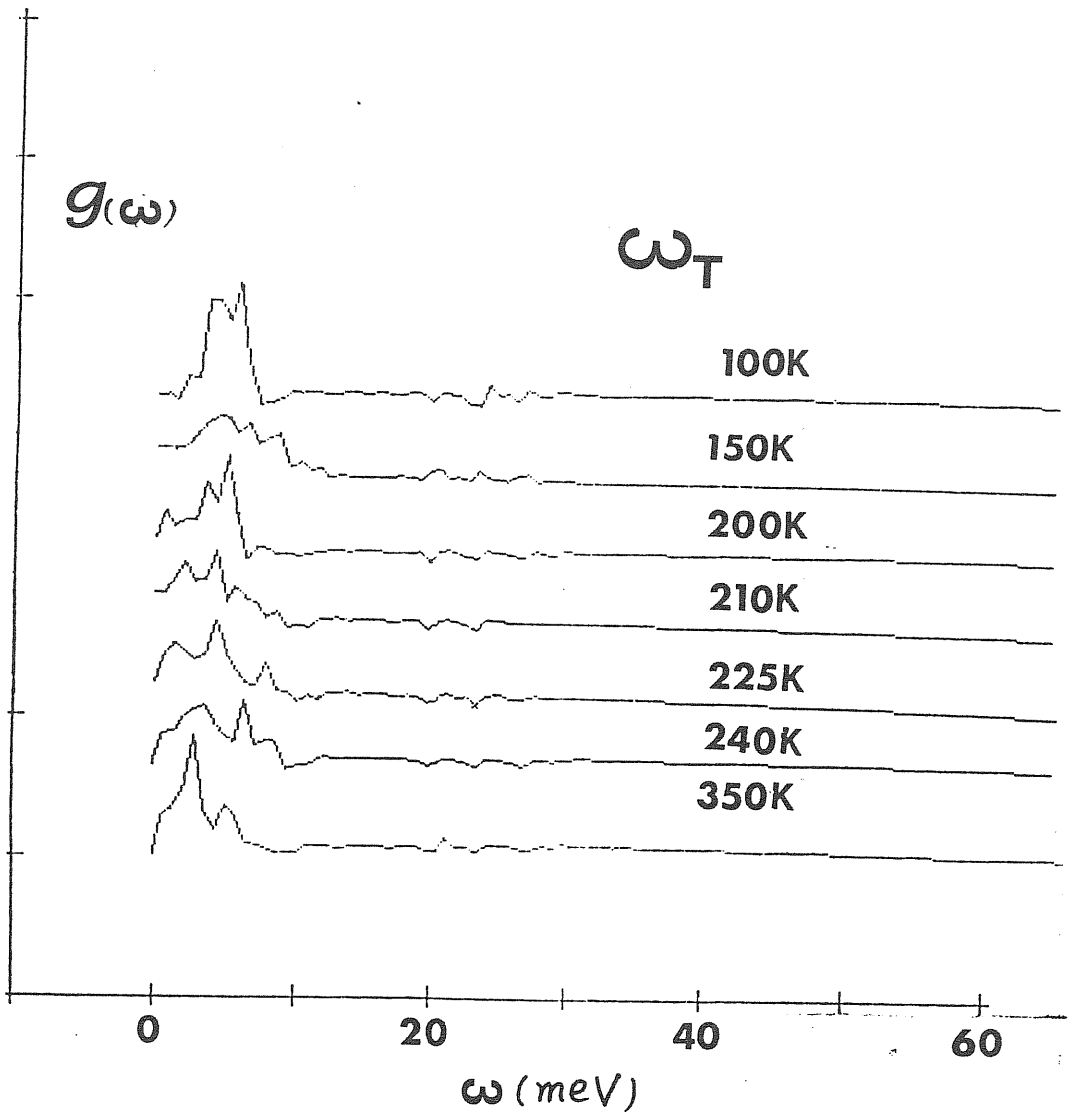

Fig.7.2 Temperature behaviour of the phonon spectral intensity of K=0 phase mode ω_T of the reconstructed W(001) surface.

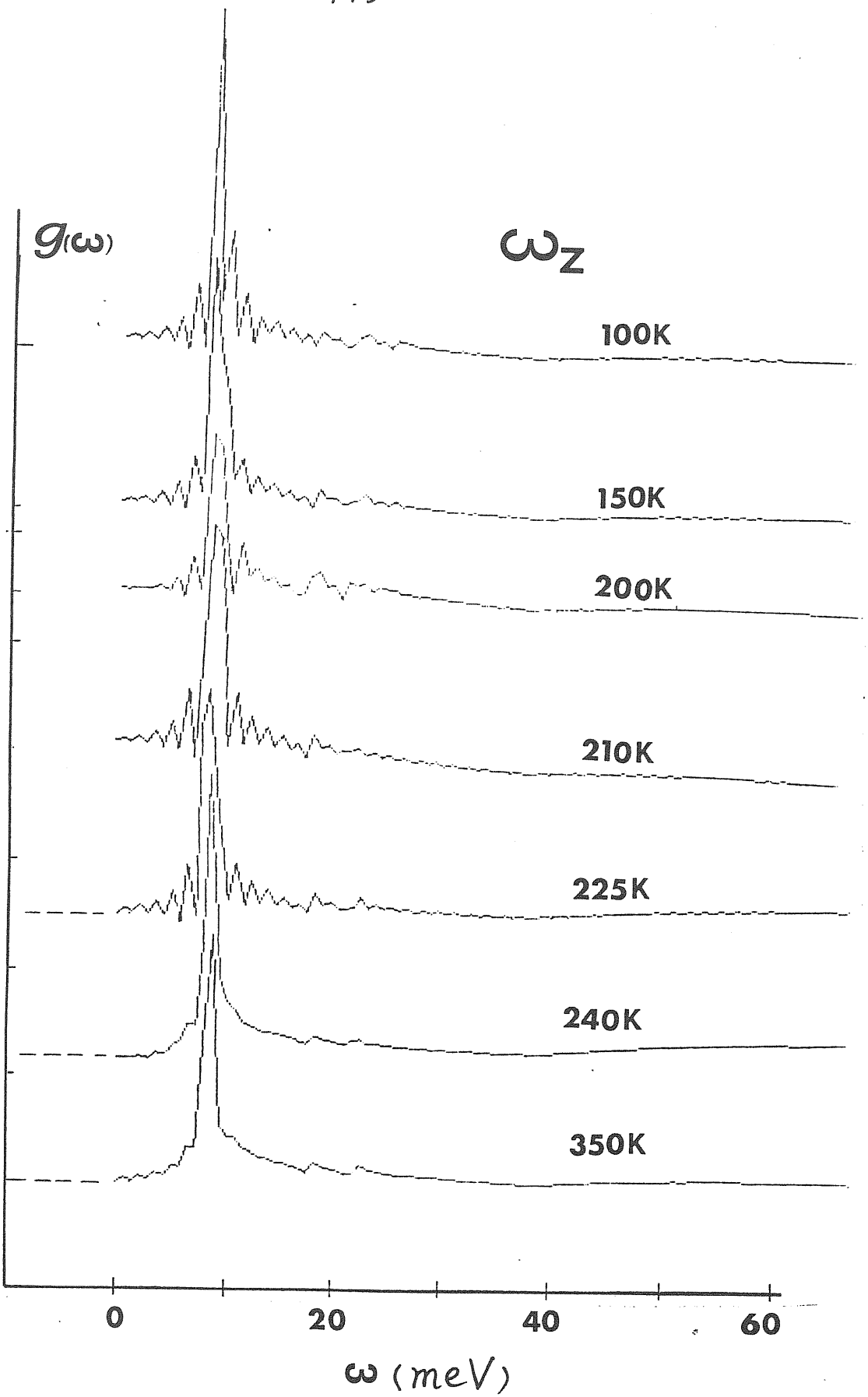

Fig.7.3 Temperature behaviour of the phonon spectral intensity of K=0 vertical mode ω_z of the reconstructed W(001) surface.

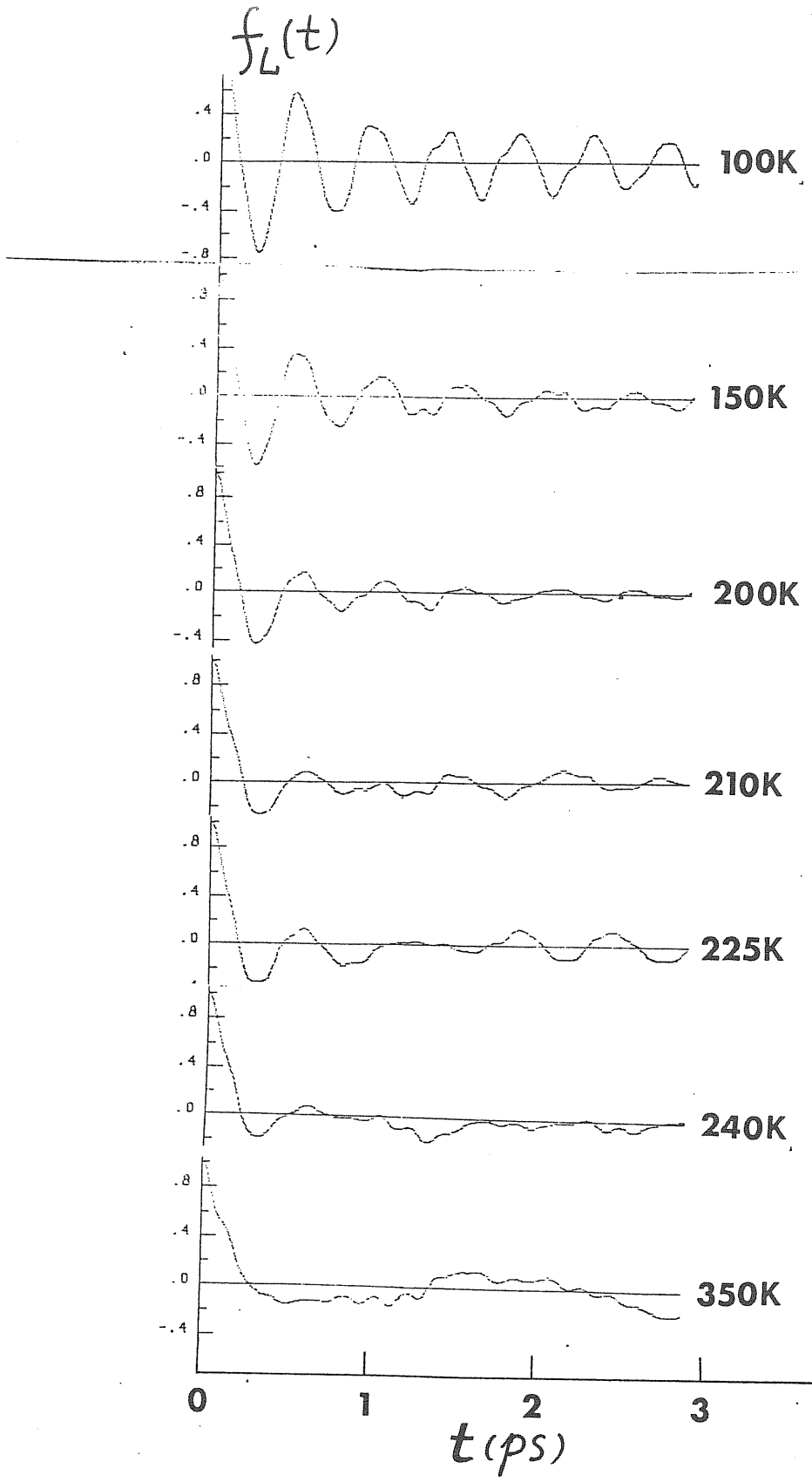

Fig.7.4 Temperature behaviour of ω_L-related velosity autocorrelation function $f_L(t)=\langle v_L(t)v_L(0)\rangle/\langle v_L(0)v_L(0)\rangle$.

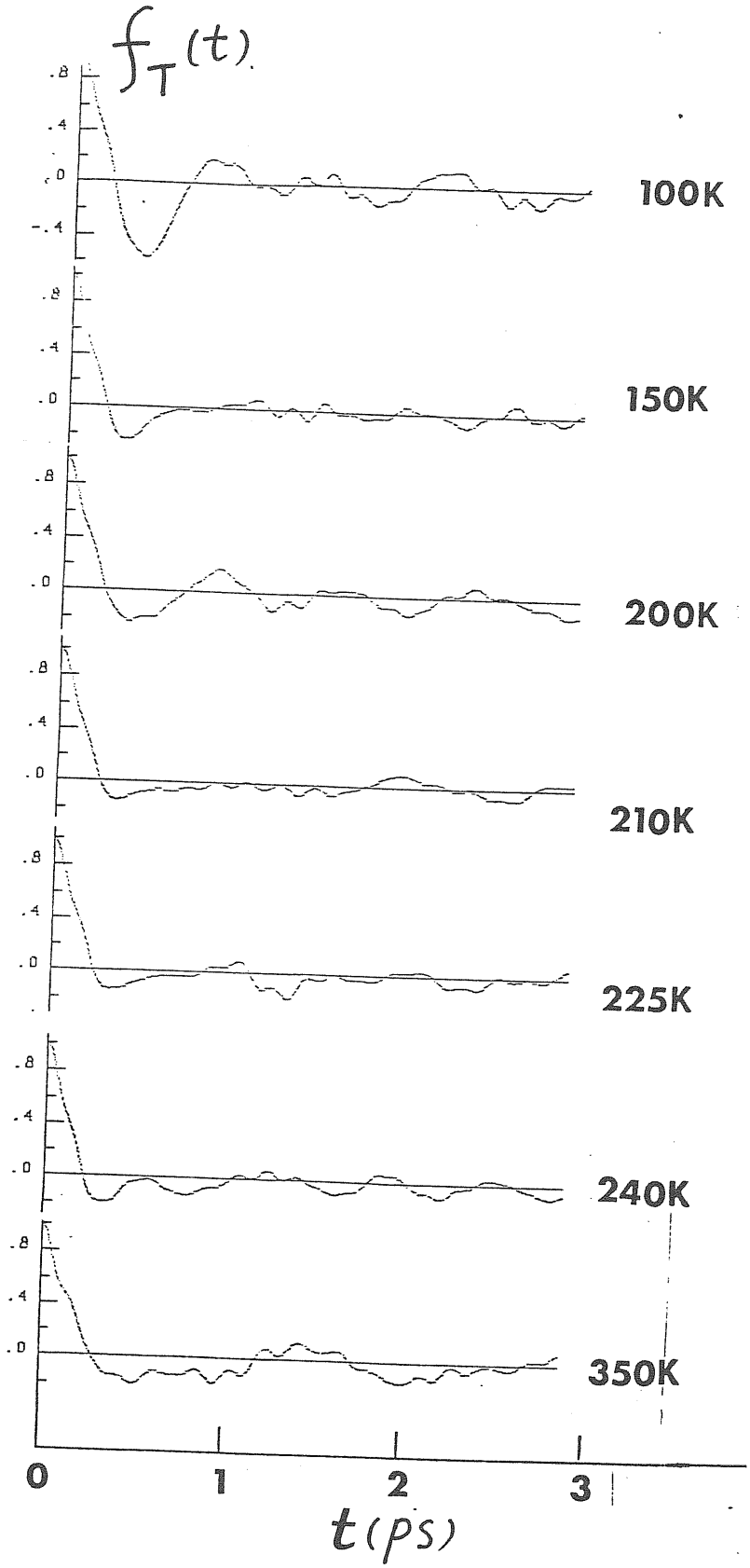

Fig.7.5 Temperature behaviour of ω_T-related velocity autocorrelation function $f_T(t)=\langle v_T(t)v_T(0)\rangle/\langle v_T(0)v_T(0)\rangle$.

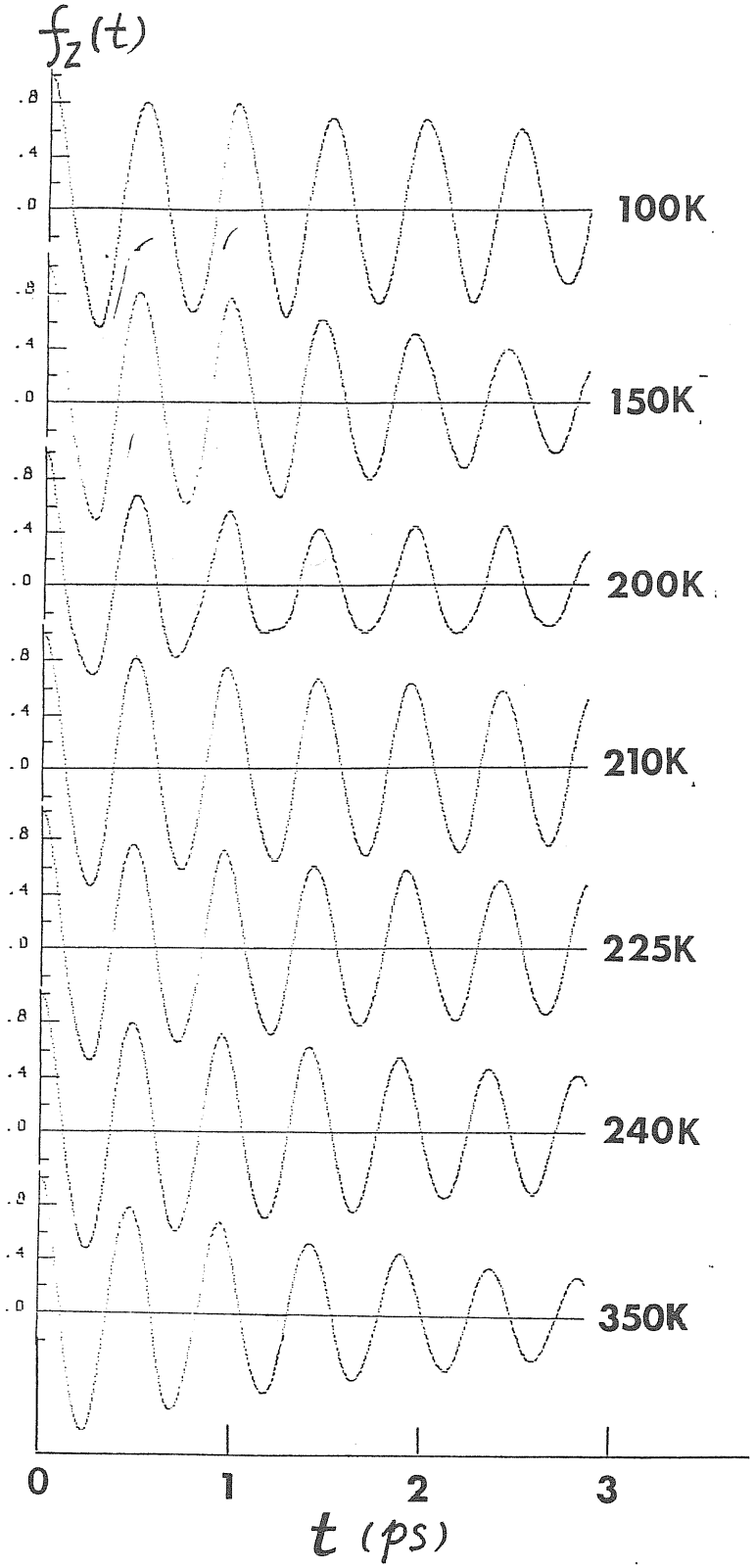

Fig.7.6 Temperature behaviour of ω_z-related velocity autocorrelation function $f_z(t)=\langle v_z(t)v_z(0)\rangle/\langle v_z(0)v_z(0)\rangle$.

Chapter 8

Incommensurate phase of Mo(001) surface reconstruction

8.1 Introduction

The surface reconstruction of Mo(001) surface has been reported /1,15/ to be incommensurate with wave vector $K=2\pi/a$ (0.44, 0.44). As it has been discussed in chapter 1 such an incommensurate phase generally arises from a long wavelength modulation of the commensurate structure and is characterized by domains and walls. The driving force for this reconstruction is expected to be short-ranged in nature similar to that of the W(001) surface, since the crystal and the electronic structure of Mo is very similar to W.

A physical mechanism for how such a long wavelength modulated structure can arise from short-ranged interactions has been discussed by Fasolino, Santoro and Tosatti /41/ based on phonon soft-modes coupling effects when two different soft modes of the ideal 1x1 surface- the planar M5 mode and the vertical M1 mode- are bot unstable and very close in (imaginary) frequency. If they would mix, one of the two mixed modes would end up being lowest. At the M point itself, M1 and M5 are orthogonal by symmetry. Away from M, however, the interaction between them produces a minimum in $\sum$ branch with an incommensurate wave vector

(see Fig.1.21). This mechanism is an excellent example of the more general interacting components mechanism proposed by Heine and Mcdonnel /102,103/ for incommensurate phase formation in bulk feroelectrics. In particular, the incommensurability on the Mo(001) surface can be reached by abandoning sinusoidal phonon-like distortions and going straight over to sharp boundaries as illustrated in Fig.8.1, where the M5 displacement u and M1 displacement v produce a 'square wave' system of antiphase domain walls. According to this mechanism, the incommensurate structure of Mo(001) should look like the one shown in Fig.8.2, whose symmetry is consistent with the LEED analysis /15,48/. But the detailed lattice distortion as well as the nature of the phase transition have not yet been clarified.

Our aim in this chapter is to make a quantitative approach for this commensurate- incommensurate phase transition by the molecular dynamics computer simulation. Since the driving force for the reconstruction is short-ranged and Mo(001) surface is very similar to the W(001) described in the previous chapters, a molecular dynamics simulation with the same lattice hamiltonian used for W(001) is expected to be useful for such a study as well. Although the MD results presented in this chapter are still preliminary, one can already see the most essential features of the lattice dis-

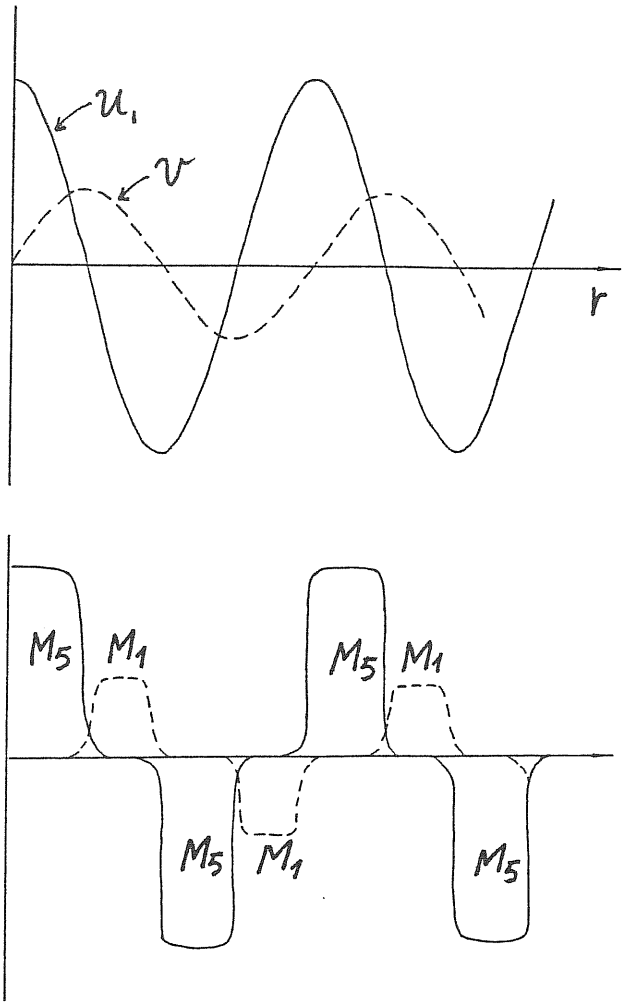

Fig.8.1 a) Spatial dependence of the two components v and u of the soft mode eigenvector at the onset of incommensurability.
b) Qualitative picture of the incommensurate phase ot Mo(001) at T=0. Almost commensurate region M5 are separated by soliton-antisoliton pairs, with an M1 (vertical) distorted phase in between.

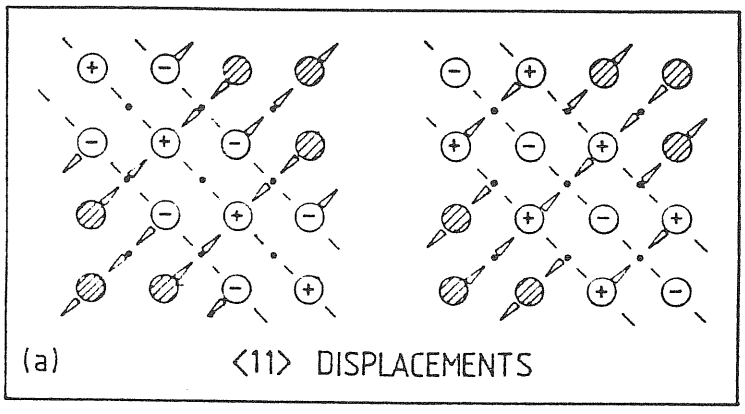

Fig.8.2 Illustration of atomic displacements at domain wall for Mo(001) incommensurate phase. The small dots denote the second layer atoms.

tortion and of the temperature behaviour of the Mo(001) surface reconstruction.

8.2 Choice of the potentials

In order to carry out the molecular dynamics simulation, first of all we need to determine the potentials for the bulk and surface Mo atoms. Following Fasolino, Santoro and Tosatti/39,41/, we have also expressed these potentials in the fourth order expansion form of e.q.(4.2) as for the case of Tungsten.

In principle, the bulk potential parameters can also be determined by the same procedure as we have done for the tungsten bulk potential, but such a procedure requires a lot of efforts, as we have already seen in chapter 4. Due to the similarity of the two materials, we found it possible to follow a simple scaling scheme to deduce the Mo bulk potential parameters from those of W bulk potential. To show this, we have collected some essential properties of the two materials and shown in Fig.8.3 and table 8.1. We found that there are some simple scaling relations between these quantities. In particular, the Debye temperatures and the two main lattice vibration frequencies between the two systems are related by a common factor α =1.24. Following a harmonic oscillator picture, the relation between the harmonic force constants of W and Mo can thus be roughly estimated as

$$\frac{\omega_W}{\omega_{Mo}} = \sqrt{\frac{C_W}{C_{Mo}} \cdot \frac{M_{Mo}}{M_W}} = \frac{1}{1.24} \qquad (8.1)$$

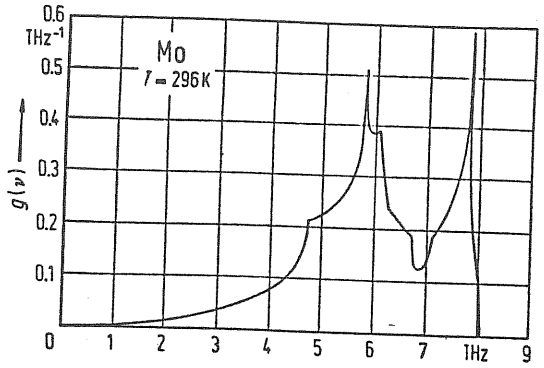

Mo. Phonon frequency spectrum at 296 K calculated from the Born-von Karman coupling parameters of Table 3 Mo [77Po1].

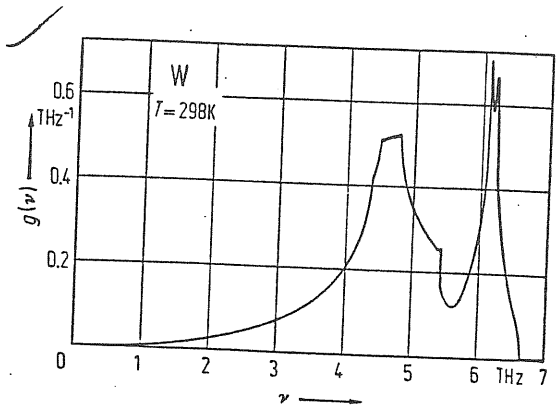

W. Frequency spectrum at 298 K calculated from the Born-von Karman parameters of Table 3 W.

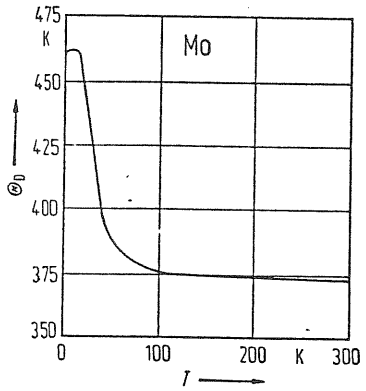

Mo. Debye temperature Θ_D calculated from the spectrum of Fig. 4. Mo [77Po1].

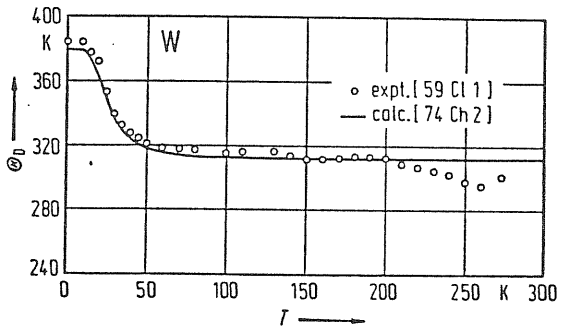

W. Debye temperatures Θ_D calculated from an eighth neighbour Born-von Karman model [74CH2]. The experimental points (o) have been corrected for the electronic contribution [59Cl1].

Fig.8.3 Some bulk properties of Mo and W (from Ref.104,105)

Table 8.1

The Properties of Bulk W and Mo (Ref. 105)

Property	Mo	W	Mo/W
Crystal Structure	bcc	bcc	
Lattice Parameter	3.15 A	3.16 A	
Melting Temperature	2890 K	3683 K	
Mass Number	95.94	183.85	
Cohesive Energy	6.82 eV/atom	8.66 eV/atom	0.79
Deby Temperature	460 K	380 K	1.22
Position of the First Peak in Phonon DOS	5.79 THz	4.67 THz	1.24
Position of the Second Peak in Phonon DOS	7.79 THz	6.17 THz	1.26

where ω is the main vibration frequency, C is the force constant and M is the mass; the subscripts denote the corresponding materials.

From (8.1) it is easy to find

$$C_{M_o} = 1.24^2 \times C_W \times \frac{M_{M_o}}{M_W} \approx 0.80\, C_W \qquad (8.2)$$

i.e. the harmonic force constants of Mo can be obtained from those of W by multiplying a factor 0.8. At the same time, the ratio of the cohesive energies $E_{M_o}/E_W \approx 0.79$ suggests the strength of the bulk potential V_{1o}, V_{2o} can also be scaled by the same factor from the corresponding values of W bulk potential. Finally, for simplicity, we have also scaled the third order anharmonic force constants γ_1, γ_2 by the same way and then the forth order anharmonic force constants δ_1, δ_2 are adjusted to fix the experimental thermal expansion data as we done in the case of W. In this way, all the parameters in the Mo bulk potential are determined as follows

V_{1o} =-1.0036 eV, α_1=-0.024 eV/Å^2, β_1=3.68 eV/Å^2,
γ_1 =-74.63 eV/Å^2, δ_1=2287.0 eV/Å^2;
V_{2o} =-0.9711 eV, α_2=0.024 eV/Å^2, β_2=2.63 eV/Å^2,
γ_2 = 63.19 eV/Å^2, δ_2=1083.3 eV/Å^2.

The corresponding potential curve is shown in Fig.8.4. This potential has been tested by a bulk MD simulation. The

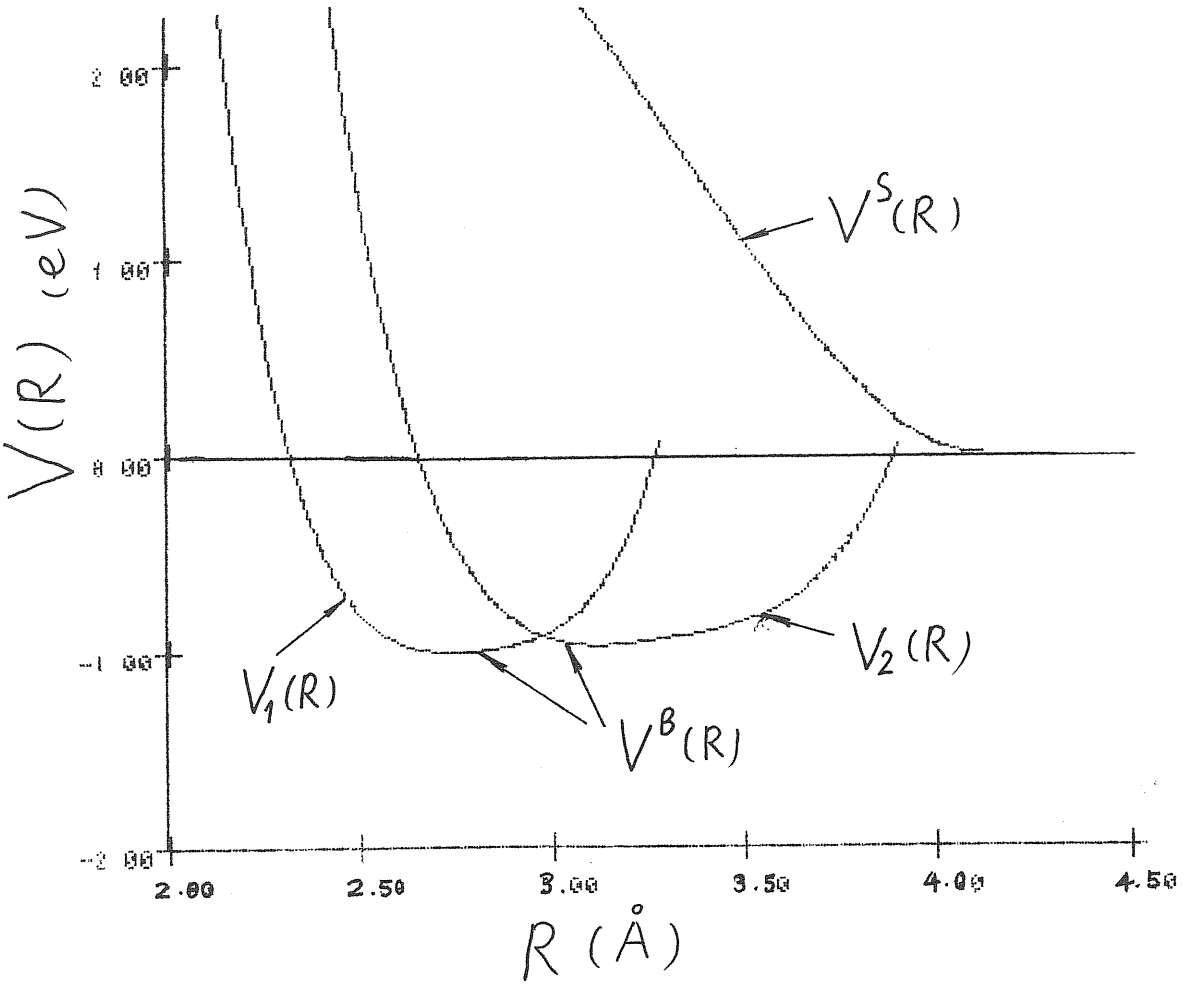

Fig.8.4 The effective pairwise potentials for bulk and surface Mo atoms.

result shows a very stable bcc structure with a correct lattice spacing (a =3.15Å) as well as an acceptable thermal expansion behaviour compared to experiment, as one can see from the bulk pair-correlation function g (r) of Fig.8.5 and thermal expansion behaviour of Fig.8.6. Therefore this bulk potential is adequate for our present study despite it was constructed in a very simple way.

The surface potential, on the other hand, has been constructed by the same way as we have done for the W(001) surface potential, because we don't know enough experimental data on the surface properties to ensure the scaling scheme. Moreover, being the details of the phase transition properties very sensitive to the surface potential parameters, they have to be determined by careful MD simulation tests. Since the incommensurate structure of Mo(001) surface is expected to arise from the coupling of soft M5 and M1 modes, our choice of the harmonic parameters α_s, β_s is therefore restricted to the region near the M_1 and M_5 boundary, i.e., the I_1 region of Fig.1.19. According to the lattice dynamical calculation /39,41,43/, such choice of α_s, β_s will end up a soft mode slight away from the M point corresponding to an incommensurate distortion. The anharmonic force constants γ_s, δ_s in the present study have been chosen arbitrarily since we don't know the detailed surface lattice distortion

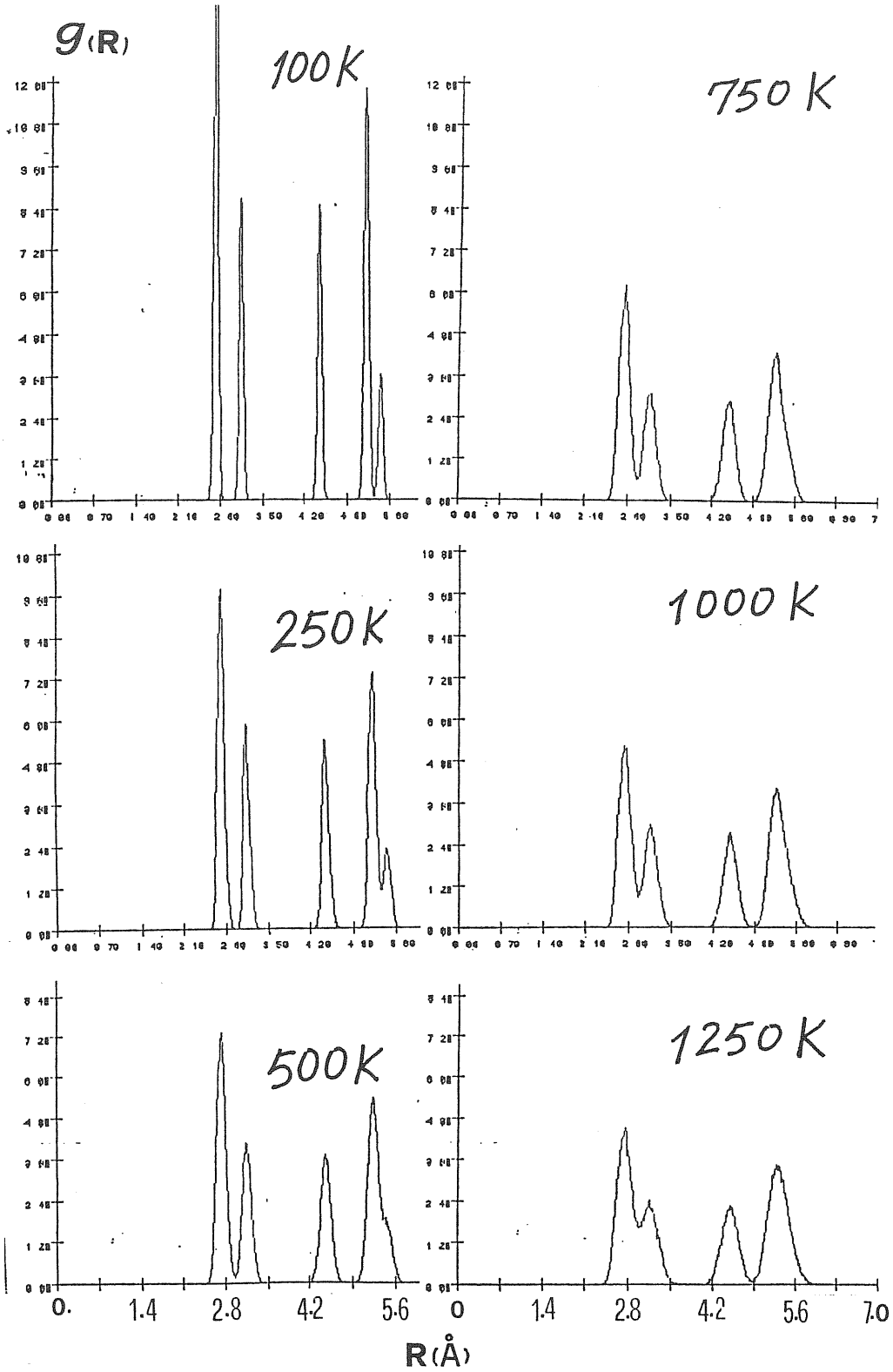

Fig.8.5 MD results of pair correlation function of bulk Mo by using the bulk potential of Fig.8.4.

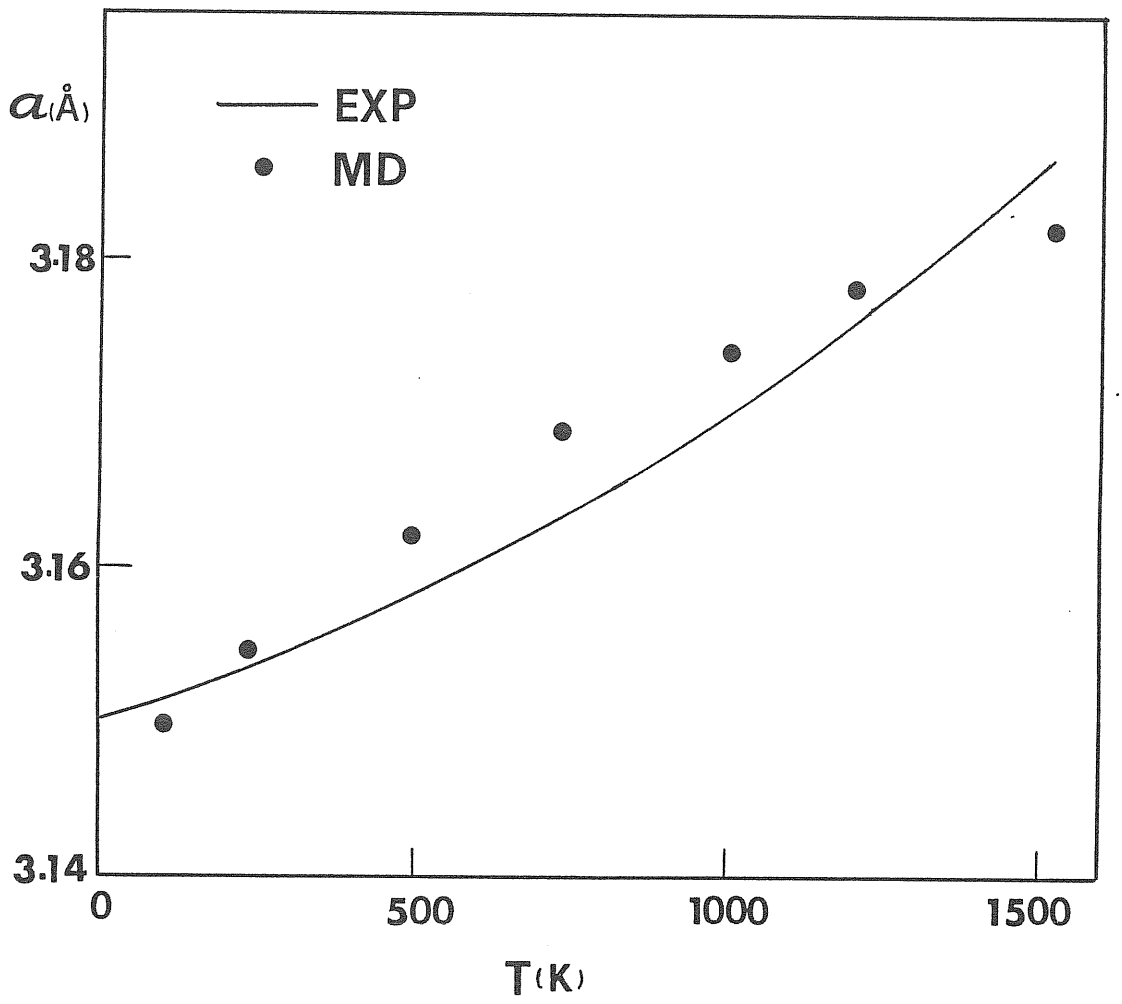

Fig.8.6 Comparison of experimental thermal expansion of the bulk Mo (Ref.104) with MD results obtained with the bulk potential of Fig.8.4.

pattern as well as the distortion amplitude. The overall parameters are then optimized through the slab MD simulation by comparing the temperature behaviour of surface structure factor S(Kx,Ky) with the LEED pattern and requiring the surface atom distortion amplitude of the same order as on W(001). The best surface potential parameters so far we have are V_{S0} =2.111eV, α_S =-0.90eV/Å^2, β_S=-0.36eV/Å^2, γ_S=3.01eV/Å^2, δ_S =180.55eV/Å^2 . The corresponding surface potential is also shown in Fig.8.4. This potential is of course still a preliminary choice. To obtain an optimized one, further tests will be needed.

8.3 Choice of MD box

Because of the presence of domains and walls in the incommensurate phase of Mo(001) surface , the MD box used for the simulation is required to be sufficiently large to allow for at least several walls to be present in the system. On the other hand, the total number of particles used for the simulation is limited due to the computation expenses. In order to have as large as possible a surface size for a given total number of particles, our choice of the MD sample has been restricted to a 3-layer slab with 512 atoms per layer to fill a(roughly) square <110> box as large as 71Ax71A. The reason of choosing <110> orientation for the

box is that the incommensurate splitting observed experimentally is along the <110> direction. For such a 3-layer slab with (x,y) periodic boundary conditions to be able to represent a surface of the semi-infinite crystal, we have chosen to fix the atoms on the lower surface of the slab to their bulk termination at a given temperature while let them act to provide the interaction forces as arising from a bulk layer. This approximation is of course very crude but it has been checked that the main features of the MD results are not altered by adding more layers. For the purpose of saving computer time, we believe the sample constructed in this way is a suitable choice.

8.4. MD results for the Mo(001) surface reconstruction

With the potentials of Fig.8.4 and time step $\Delta t=4\times10^{-15}$ sec., the constant volume, constant temperature MD simulation as used for the study of W(001) was carried out. We start with an ideal (1x1) surface - since we don't know the exact atomic distortion of the reconstructed surface - and a careful annealing has been performed to allow the system to reach the low temperature equilibrium configuration. Then we increased the temperature to study the temperature dependence of the transition. 10,000 MD steps have been used for the annealing. We believe the final configuration of the low temperature phase thus achieved is the

equilibrated one because the averaged surface structure factor has been found being converged. When we change the temperature, we allow 4000 MD steps for the system to establish new equilibrium, then the following by 4000 MD steps for useful averaging.

Fig.8.7 shows the surface structure factor S(Kx,Ky) near $K=2\pi/a(1/2,1/2)$ and $K=2\pi/a(1/2,-1/2)$ for various temperatures. The splitting of the (1/2,1/2) spot with $\vec{K}=2\pi/a(0.44, 0.44)$ show up clearly at low temperature ,T=50K for example. The satellite intensity decreases with increasing temperature, similar to LEED observations. The top view of the surface layer atomic positions is shown in Fig.8.8, where the corresponding surface atom coordinates belonging to the chains as labelled (each chain contains 16 atoms) have also been plotted respectively. The perspective view of the slab atomic positions at various temperature is shown in Fig.8.9. From these figures one can see that the low temperature incommensurate structure consists of anti-phase M5 type domains (in-plane distortion) separated by the M1 domains (vertical distortion) by very sharp domain boundaries. This result is consistent with the soft phonon coupling picture proposed by Fasolino, Santoro and Tosatti /41/, as we have discussed in section 1. As the temperature increases, both the in-plane and vertical distortions are

found to decrease, indicating a transition to a (1x1) commensurate phase. The temperature behaviour of the satellite intensity of S(Kx,Ky) is shown in Fig.8.10, in which the values of S(Kx,Ky) at each temperature are the average of two satellite spots intensities at that temperature. The transition temperature is roughly estimated to be $Tc \sim 150K$, as can also be seen from the surface energy plot of Fig.8.11. This value is still lower than the experimental estimations $Tc^{exp.}$ 300K /1/.

Finally, it should be pointed out that the MD results presented in this chapter are just preliminary ones. The detailed nature and the thermodynamics of the phase transition, as we have done for the W(001) surface, need to be further clarified. Such a study is now in progress.

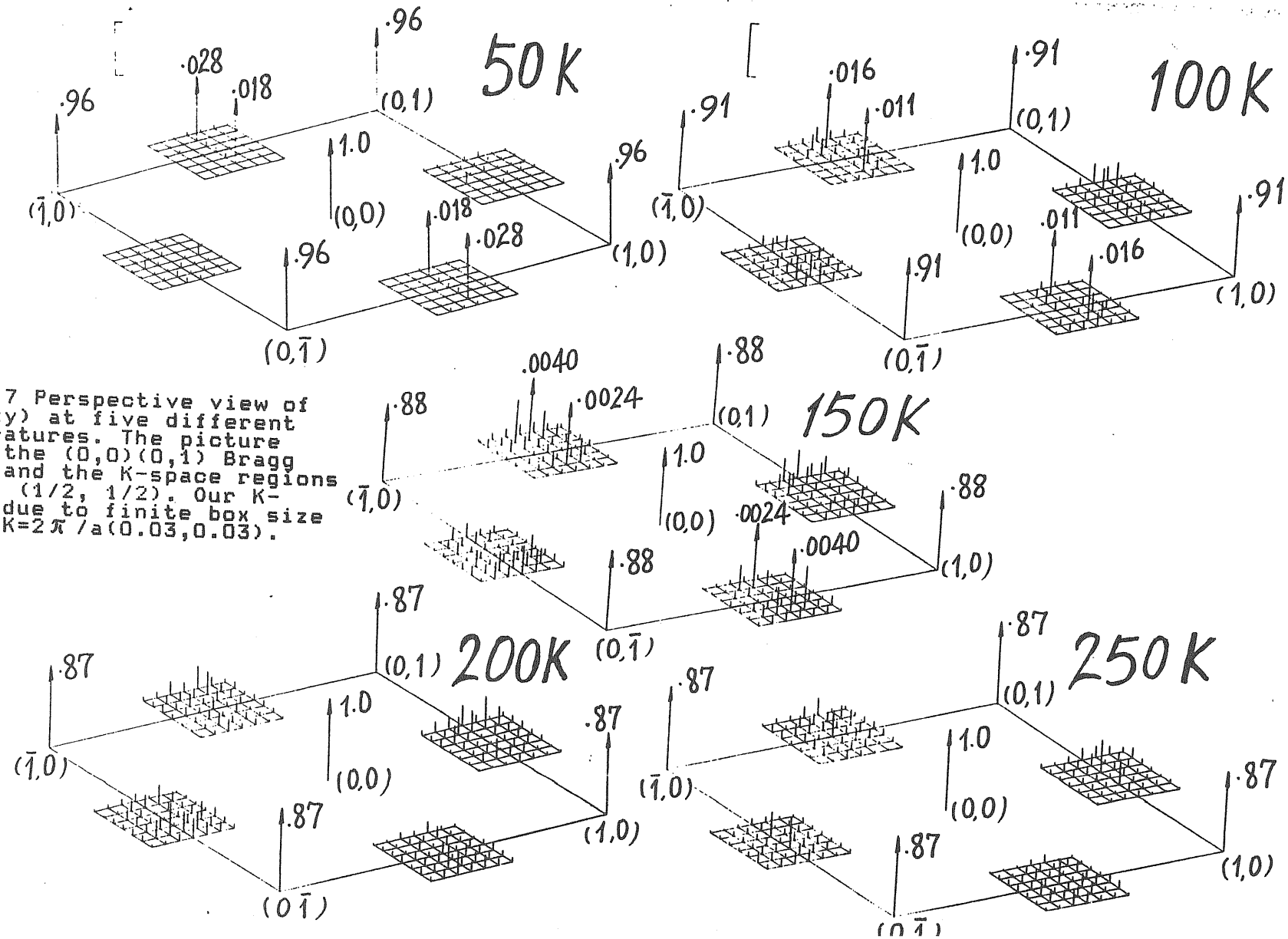

Fig.8.7 Perspective view of S(kx,ky) at five different temperatures. The picture shows the (0,0)(0,1) Bragg peaks and the K-space regions around (1/2, 1/2). Our K-grid, due to finite box size , is $\Delta K = 2\pi / a(0.03,0.03)$.

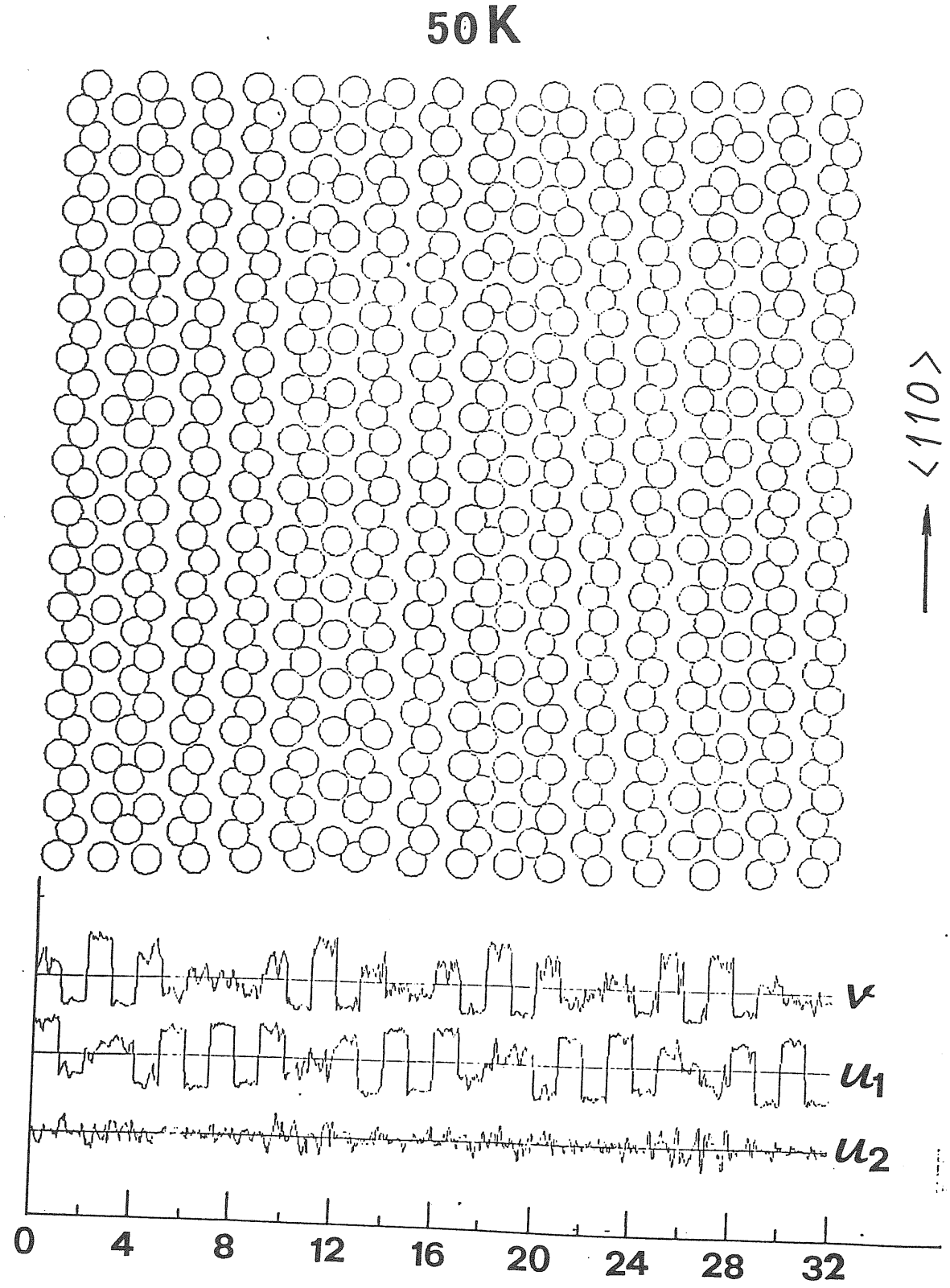

Fig.8.8 The top view of surface layer atomic positions. The radius of the circles used to represent the atoms has been arbitrarily chosen and the distortion amplitudes enhanced by a factor of three for better visualization. In the bottom of the figure, the surface atom coordinates are plotted for each chain with 32 chains in u direction as labeled. (See also the next 4 pages)

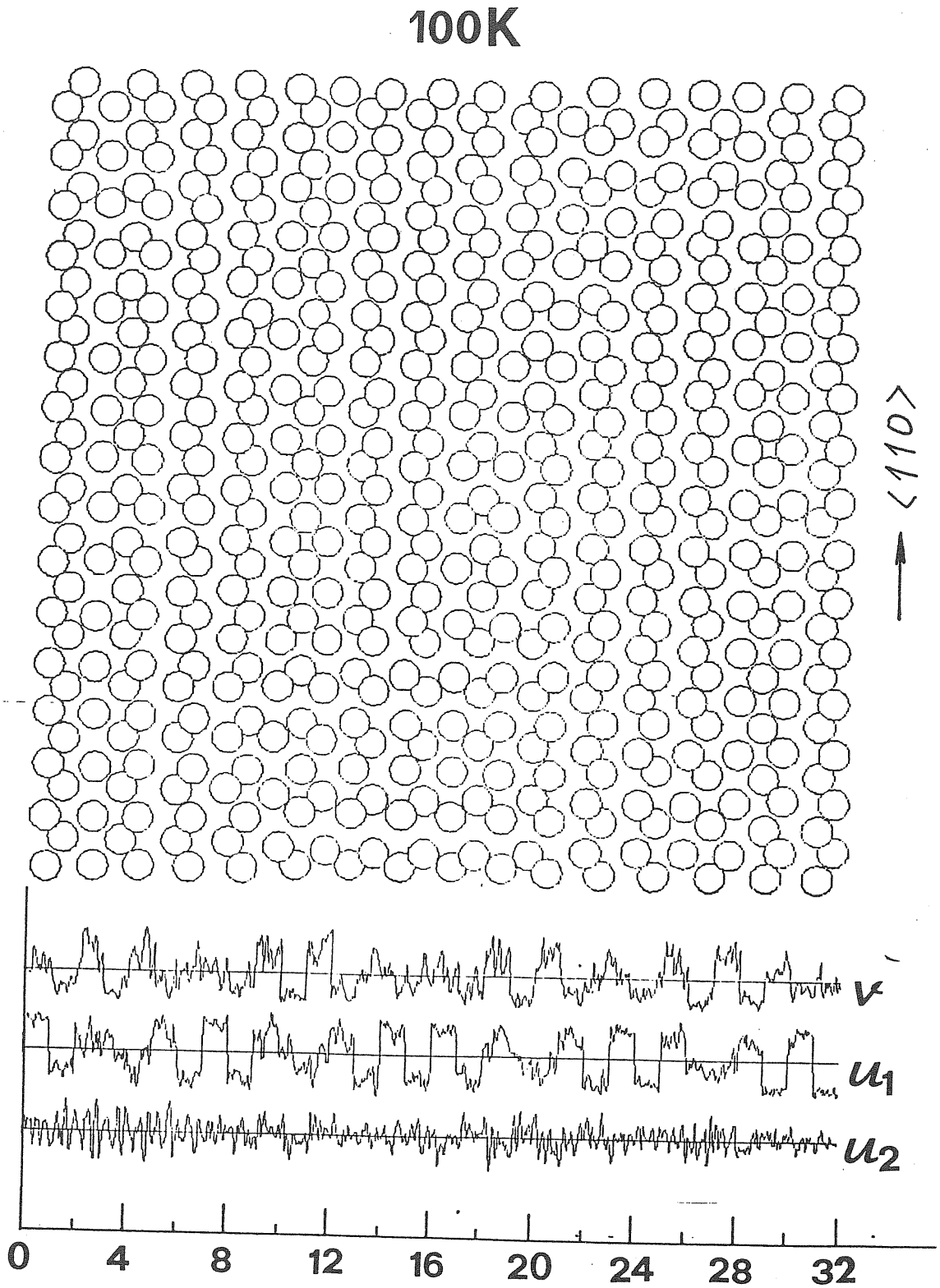

Fig 8-8 (b)

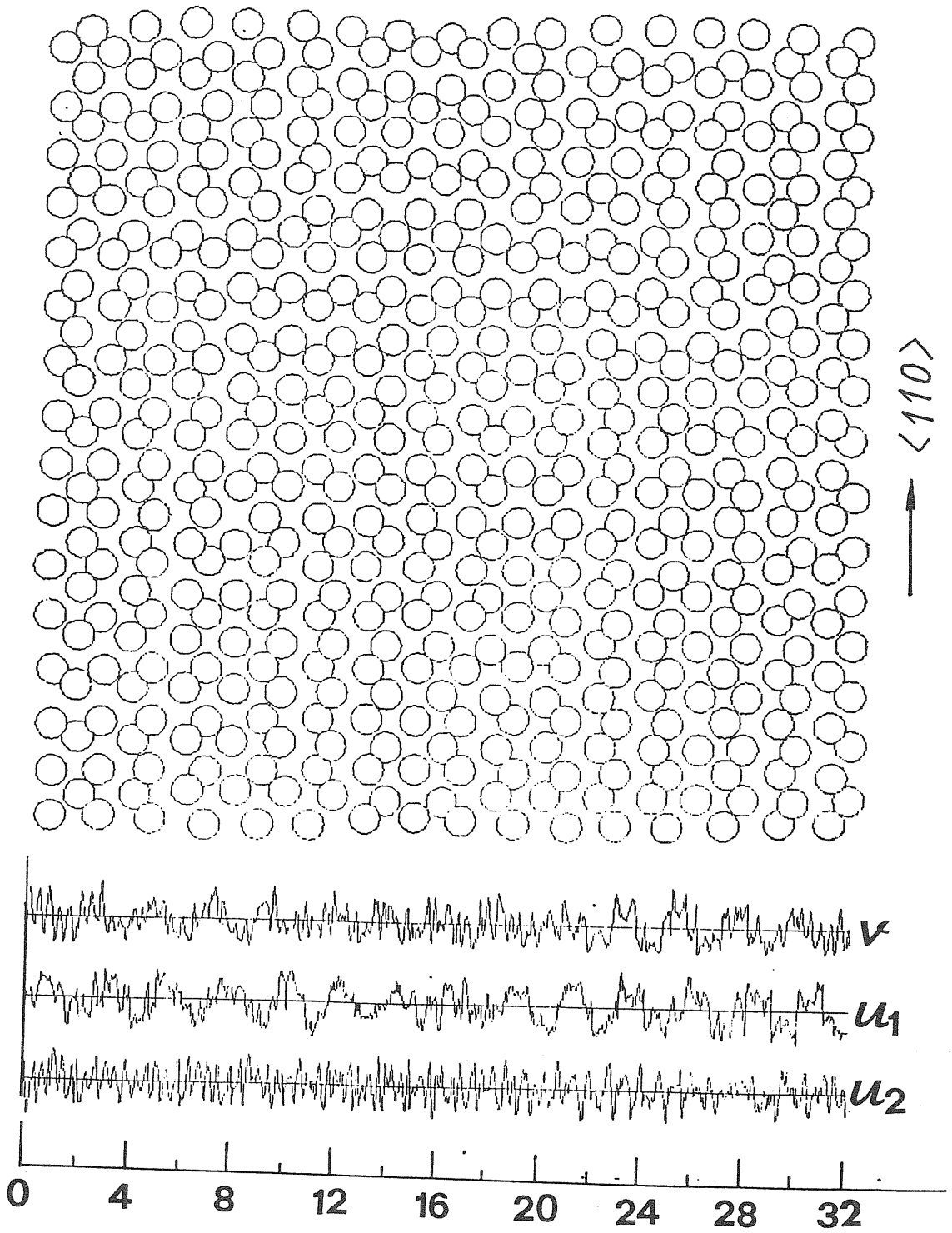

Fig. 8.8 (c)

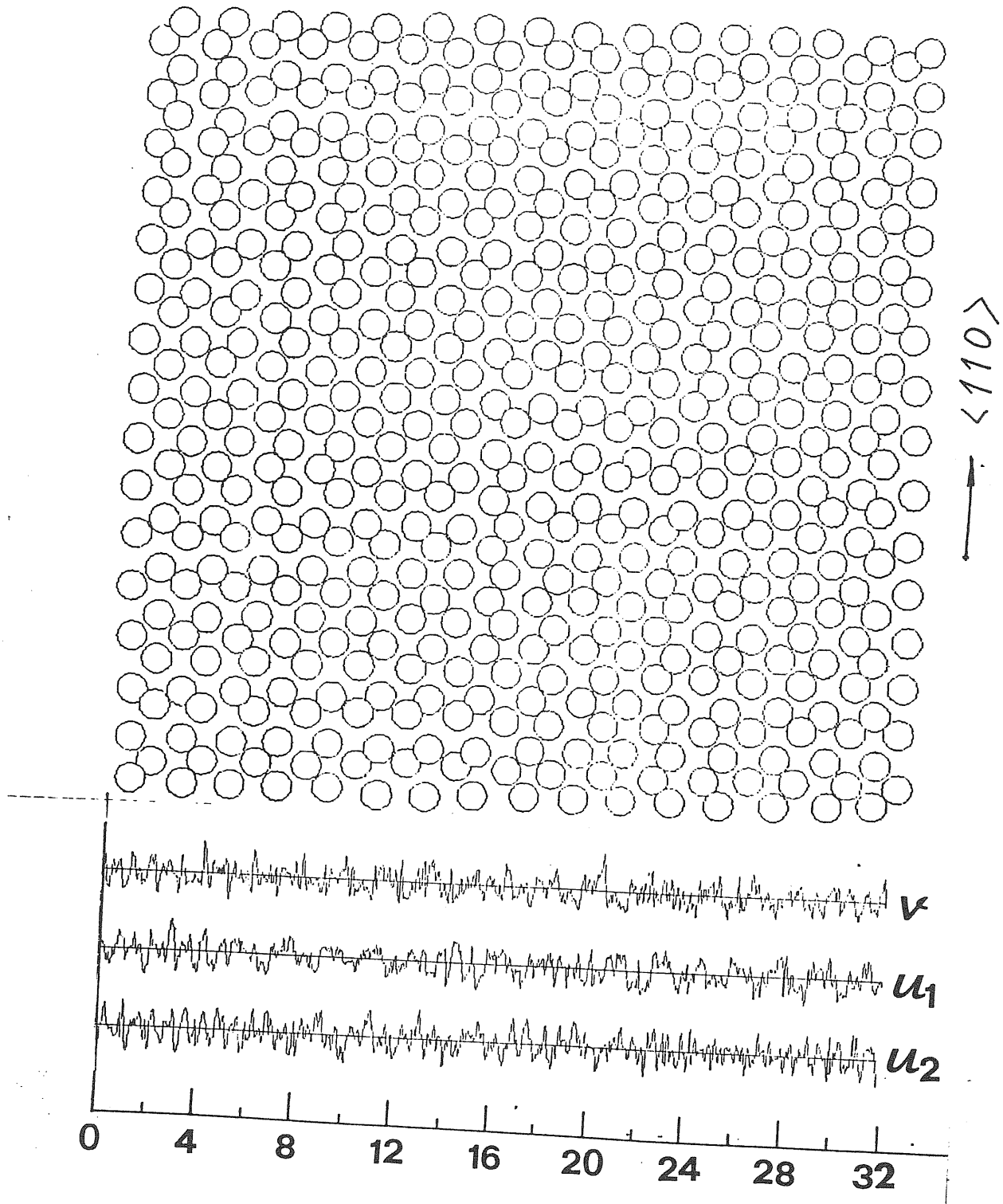

Fig. 8.8 (d)

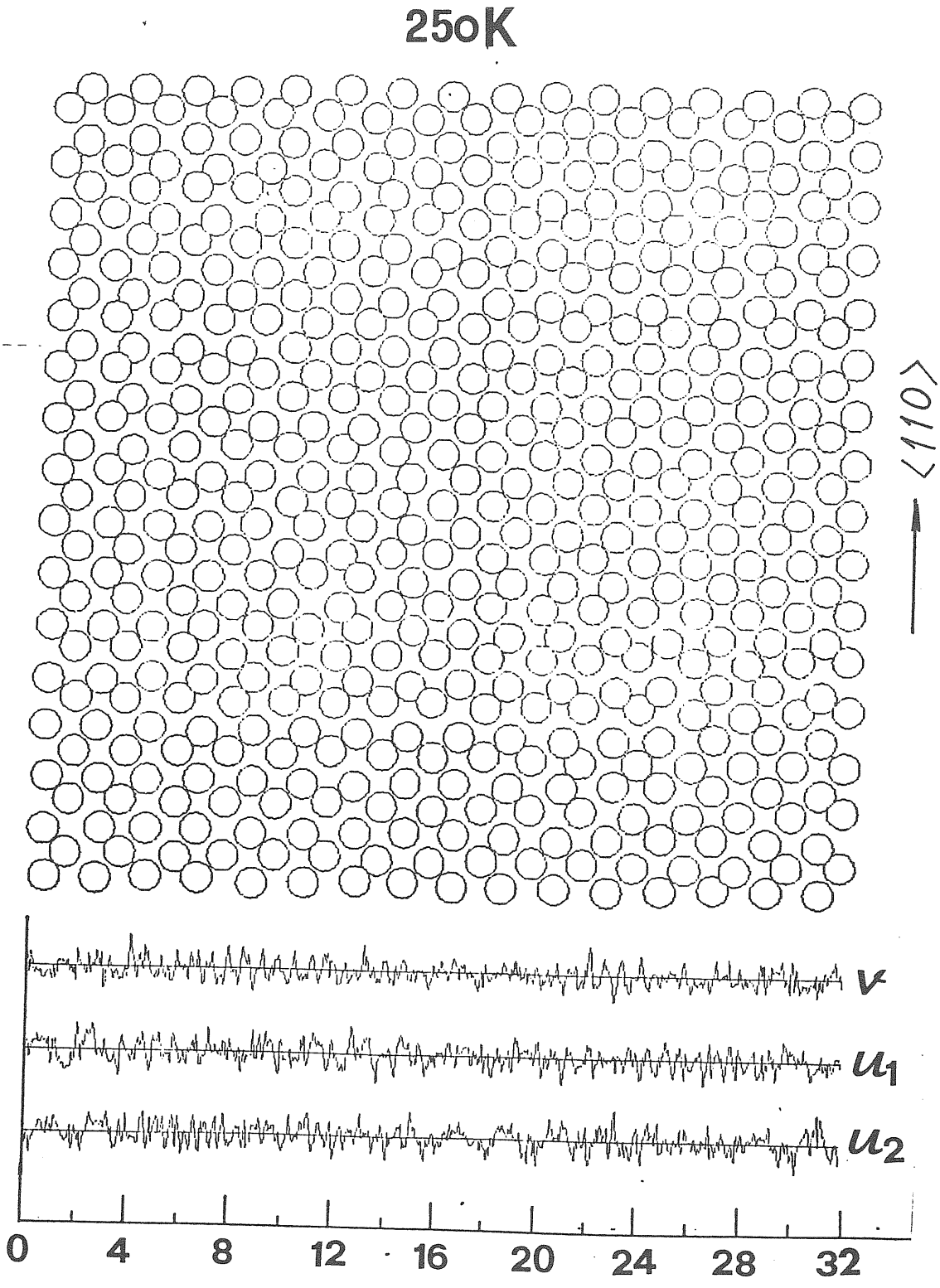

Fig. 8.8 (e)

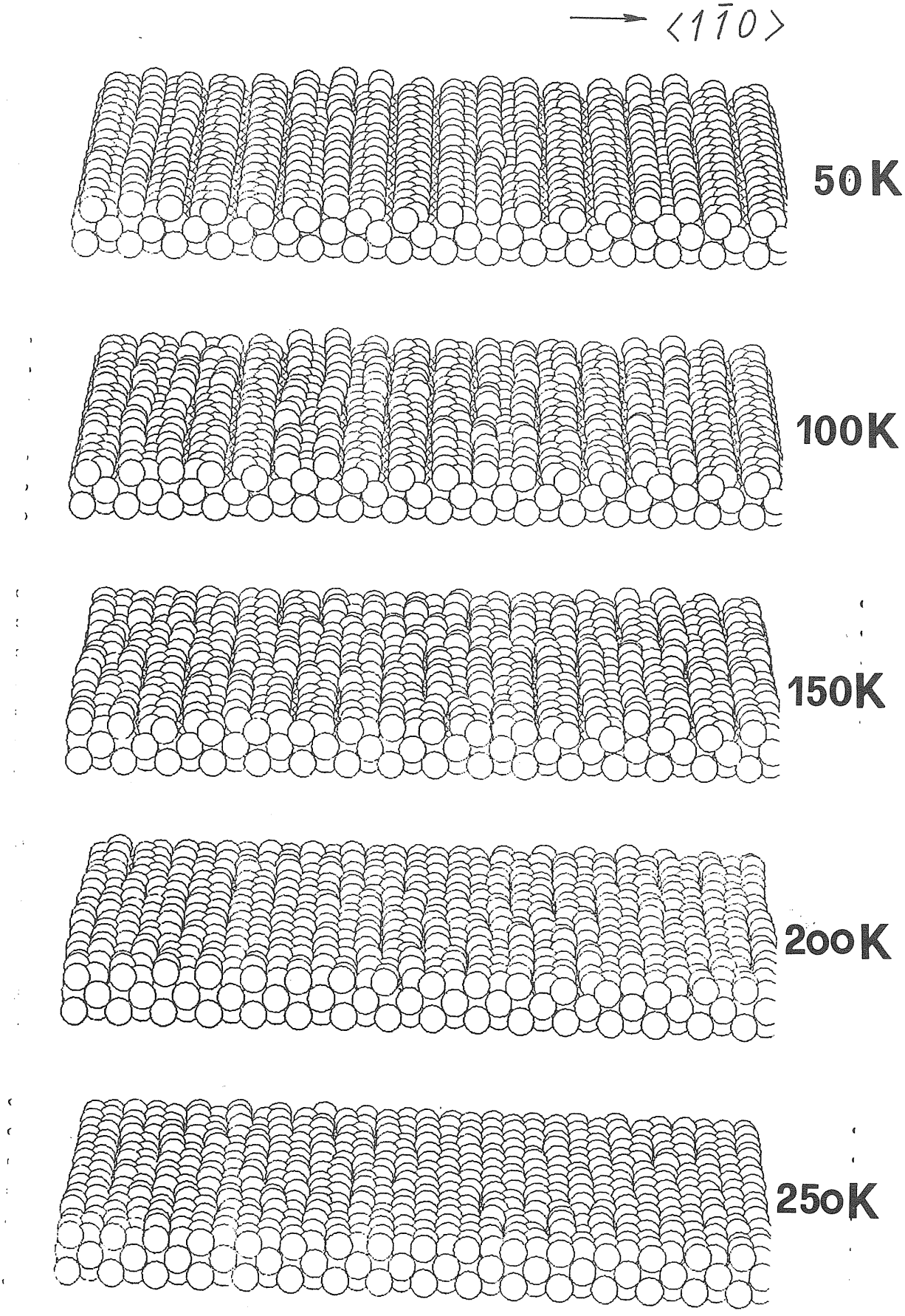

Fig.8.9 The perspective view of the surface atomic structure of Mo(001) at five temperatures.

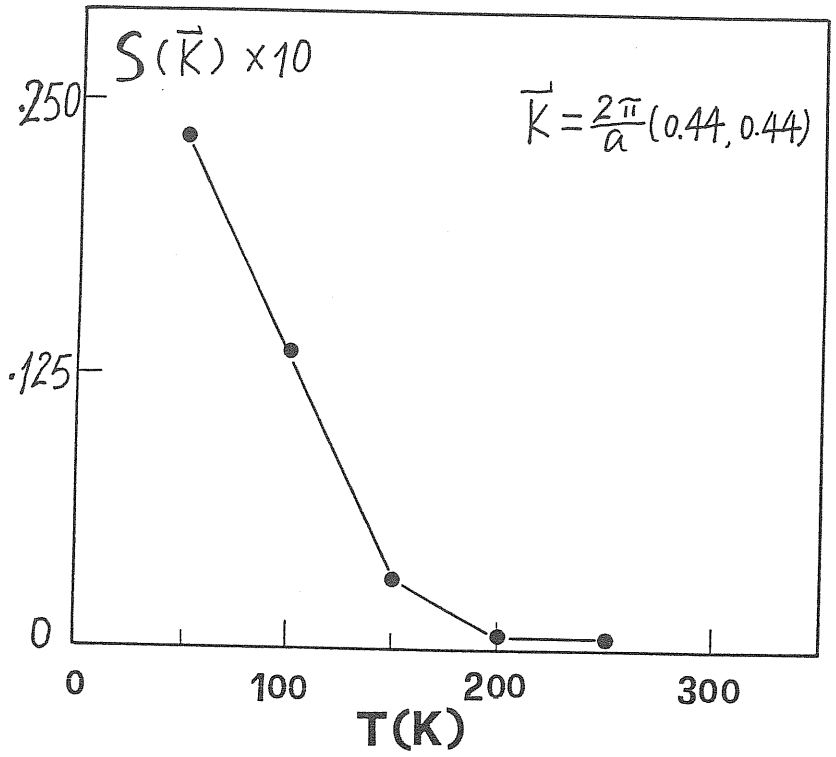

Fig.8.10 The satelite intensity of the incommensurate splitting as the function of temperature.

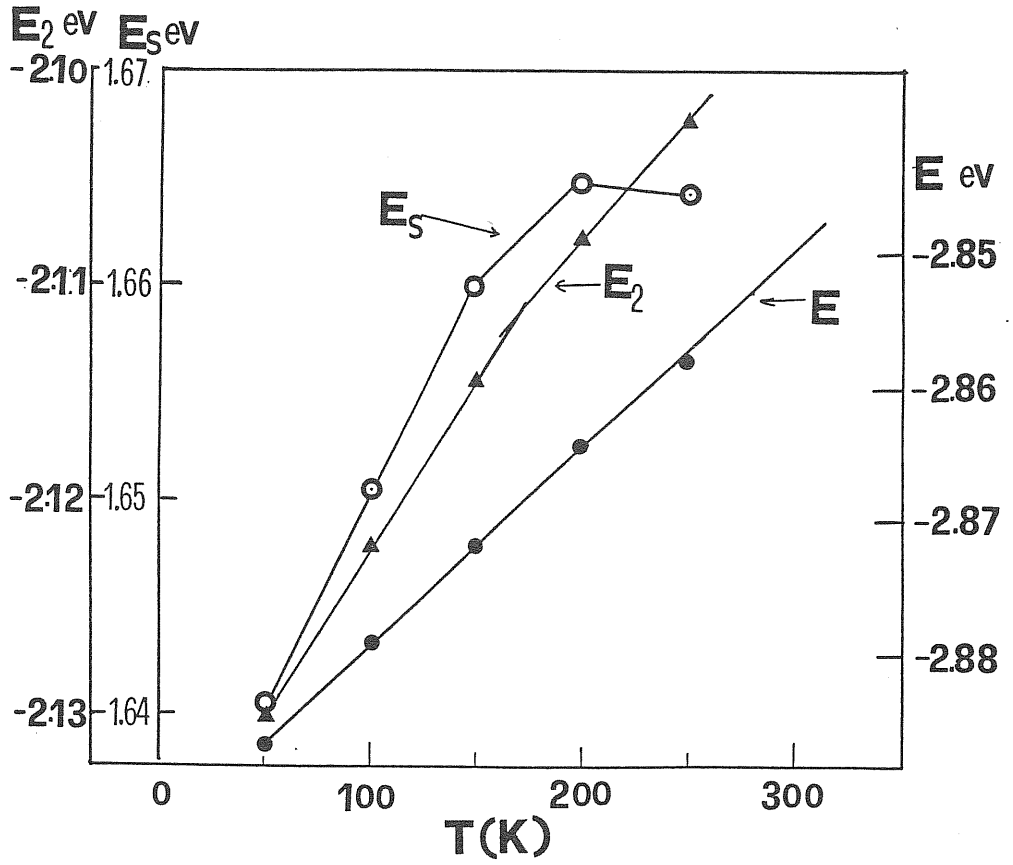

Fig.8.11 The energies as the function of temperature. Es-- the energy of the surface layer; E_2 -- the energy of the upper two atomic layers; E -- the total energy of the

References

1. T.E.Felter, R.A.Barker, and P.J.Estrup, Phys.Rev. Lett. 38, 1138 (1977)
2. M.K.Debe and D.A.King, J. Phys. C10, L303 (1977)
3. K.Yonehara and L.D.Schmidt, Surf. Sci. 25, 238 (1971)
4. J.F.Wendelken and G.C.Wang, Phys. Rev. B32 7542 (1985)
5. M.K.Debe and D.A.King, Phys. Rev. Lett. 39, 708 (1977)
6. M.K.Debe and D.A.King, Surf. Sci. 81, 193 (1979)
7. R.A.Barker, P.J.Estrup, F.Jona and P.M.Marcus, Solid State Commun. 25, 375 (1978)
8. J.A.Walker, M.K.Debe and D.A.King, Surf.Sci. 104, 405 (1981)
9. R.A.Barker and P.J.Estrup, J. Vacuum Sci. Technol. 18, 546(1981).
10. G.C.Wang and T.M.Lu, Surf. Sci. 122, L635 (1982)
11. R.T.Tung, W.R.Graham and A.J.Melmed, Surf. Sci. 115, 576 (1982); A.J.Melmed, R.T.Tung, W.R.Graham and G.D.W.Smith, Phys. Rev. Lett. 43, 1521(1979); Melmed A.J. and W.R.Graham, Appl. Surf. Sci. 11, 400(1982)
12. Tsong T.T. and Sweeney J., Solid State Commun. 30, 767 (1979)
13. I.Stensgaard, L.C.Feldman and P.J.Silverman, Phys.Rev. Letts. 42, 247 (1979) L.C.Feldman, P.J.Silverman and I.Stensgaard, Surf.Sci. 87, 410 (1979)
14. D.A.King, Physica Scripta, T4, 34 (1983)
15. R.A.Barker, S.Semancik and P.J.Estrup, Surf.Sci. 94, L162 (1980)
16. C.Guillot, C.Thaualt, Y.Jugnet, D.Chauvean, R.Hoogewijks, J.Lecante, Tran Minh Duc, G.Treglia, M.C.Desjonqueres and D.J.Spanjaard, J. Phys. C15, 4023 (1982)
17. J.C.Campuzano, J.E.Inglesfield, D.A.King and C.Somerfor, J. Phys. C14, 3099 (1981)
18. R.A.Barker and P.J.Estrup, J. Chem. Phys. 74, 1442 (1981)
19. L.D.Roelofs, G.Y.Hu and S.C.Ying, Phys. Rev. B28, 6369 (1983)

20. C.Y.Hu and S.C.Ying, Preprint.
21. L.D.Roelofs, to be published.
22. C.Y.Hu and S.C.Ying, Surf. Sci. 150, 47 (1985)
23. K H.Lau, S.C.Ying, Phys.Rev.Lett. 44, 1222(1980)
24. M.Posternak, H.Krakauer, A.J.Freeman and D.D.Koelling, Phys. Rev. B21, 5601 (1980)
25. L.F.Mattheis and D.R.Hamann, Phys. Rev. B29, 5372 (1984)
26. I.Terakura, K.Terakura and N.Hamada, Surf. Sci. 111, 479 (1981)
27. K.Terakura, I.Terakura and Y.Teraoka, Surf. Sci. 86, 535 (1979)
K.Terakura, I.Terakura and N.Hamada, Surf. Sci. 13, 103 (1981)
28. M.C.Desjonqueres and F.Cyrot-Lackmann, J.Phys. F6, 567 (1976)
29. J.E.Inglefield, J. Phys. C11, L69 (1978)
J. Phys. C12, 149 (1979)
30. J.E.Inglesfield, Rep. Prog. Phys. 45, 223 (1982)
31. S.Ohnishi, A.J.Fieeman and E.Wimmer, Phys.Rev. B29, 5267 (1984)
32. C.L.Fu, A.J.Freeman, E.Wimmer and M.Weinert, Phys. Rev. Lett. 54, 2261 (1985)
33. M.I.Holmes and T.Gustafsson, Phys. Rev. Lett. 47, 443 (1981)
34. H.Krakauer, M.Posternak and A.J.Freeman, Phys.Rev. Lett. 43, 1885 (1979)
35. P.C.Stephenson and D.W.Bullett, Surf. Sci. 139, 1 (1984)
36. G.Meister, P.Giesert and J.Holzl, Surf. Sci. 143, 547 (1984)
37. E.Tosatti, Solid State Commun. 25, 637 (1978) and in 'Modern Trends in the Theory of Condensed Matter', eds. A.Pekalski, J.Przystawa (Springer, Berlin 1980)
38. E.Tosatti and P.W.Anderson, Solid State Commun. 14, 773 (1974)
39. A.Fasolino, G.Santoro and E.Tosatti, Phys. Rev. Lett. 44, 1684 (1980); Surf. Sci. 125, 317 (1983)

40. L.D.Roelofs and S.C.Ying, Surf. Sci. 147, 203(1984)
41. A.Fasolino, G.Santoro and E.Tosatti, J. Phys. (Paris) Colloq. C6, 846 (1981)
42. P.Bak, Solid State Commun. 32, 581 (1979)
43. A.Fasolino and E.Tosatti, to be published.
44. S.C.Ying, in 'Dynamical phenomena at Surfaces, Interfaces and Superlattices', eds. F.Nizzoli, K.H.Rieder and R.F.Willis (Springer, Berlin 1985) P. 148
45. M.K.Debe and D.A.King, J. Phys. C15, 2257 (1982)
46. Guy Tregliat, Marie-Catherine Desjonqueres and Daniel Spanjaard, J. Phys. C16, 2407 (1983)
47. David A.King and Graham Thomas, Surf.Sci. 92, 201 (1980)
48. R.F.Willis in 'Many-Body Phenomena at Surfaces', eds. D.Langreth, H.Suhl (Academic New York, 1984) and in 'Dynamical Phenomena at Surfaces, Interfaces and Superlattices', eds. F.Nizzoli, K.H.Rieder and R.F.Willis (Springer, Berlin, 1985) P.126
49. B.Salanon and J.Lapujoulade, Surf. Sci. 173, L613(1986).
50. L.D.Roelofs and P.J.Estrup, Surf. Sci. 125, 51 (1983)
51. S.C.Ying and L.D.Roelofs, Surf. Sci. 125, 218 (1983)
52. T.Inaoka and A.Yoshimori, Surf. Sci. 149, 241 (1985)
53. D.P.Woodraff, Surf. Sci. 122 L653(1982).
54. P.J.Estrup, J. Vacuum Sci. Technol 16, 635(1979)
55. J.F.Wendelken and G.C.Wang, J. Vacuum Sci. Technol A2, 886(1984).
56. L.D.Roelofs and P.J.Estrup, Surf. Sci. 125, 51(1983).
57. P.Heilmann, K.Heinz and K.Muller, Surf.Sci. 89, 84(1979)
58. M.N.Barber, in 'Phase transition and critical phenomena' Eds. C.Domb and J.L.Lebowitz (Academic 1983) vol.8, P.146.
59. L.D.Landau, E.M.Lifshitz, 'Statistical Physics' (Pergammon, Oxiford, U.K., 1980)
60. See for example, A.D.Bruce and R.A.Cowley, 'Structural Phase Transitions' (Taylor and Francis, London, 1981)
61. See for example, K.Binder, 'Monte Carlo Methods in Statistical Physics' (Springer-Verlag, Berlin, 1979)

and 'Applications of the Monte Carlo Method in Statistical Physics' (Springer-Verlag, Berlin, 1984)

62. B.J.Alder and T.E.Wainwright, J. Chem. Phys. 27, 1208 (1957); 31, 459 (1959)
63. A.Rahman, Phys. Rev. A136, 405 (1964)
64. A.Rahman and P.Vashishta, in 'The physics of superionic conductors and electrode materials' Ed. J.P.Perram (NATO ASI Series 1980)
65. T.Schneider and E.Stoll, Phys. Rev. Lett. 35, 296 (1975)
66. T.Schneider and E.Stoll, Phys. Rev. Lett. 31, 1254 (1973)
67. T.Schneider and E.Stoll, Phys. Rev. B10, 4799(1974)
68. T.Schneider and E.Stoll, Phys. Rev. B13, 1216(1976)
69. T.Schneider and E.Stoll, Phys. Rev. B17, 1302(1978)
70. T.Schneider and E.Stoll, in 'Local Properties at Phase Transitions', eds. K.A.Muller and A.Rigamoni. (Academic, New York, 1977)
71. M.L.P.Bartolome and W.C.Kerr, Solid State Commun. 21, 253 (1977)
72. W.C.Kerr, Phys. Rev. B19, 5773 (1978)
73. See, for example, M.Parrinello and A.Rahman, J. Chem. Phys. 80, 860(1984) and references therein.
74. R.Car and M.Parrinello, Phys. Rev. Lett. 55, 2471 (1985)
75. H.C.Andersen, J. Chem. Phys. 72, 2384 (1980)
76. M.Parrinello and A.Rahman, Phys. Rev. Lett. 45, 1196 (1980)
77. M.Parrinello and A.Rahman, J. Appli. Phys. 52, 7182 (1981)
78. S.Nose, Molec. Phys. 52, 255 (1984)
79. S.Nose, J. Chem. Phys. 81, 511 (1984)
80. D.M.Heyes, Chem. Phys. 82, 285 (1983)
81. W.G.Hoover, D.J.Evans, R.B.Hichman, A.J.C.Ladd, W.T.Ashurst and B.Moran, Phys. Rev. A22, 1690 (1980)
82. W.G.Hoover, A.J.C.Ladd and B.Moran, Phys.Rev.Lett. 48, 1818 (1982)
83. A.J.C.Ladd and W.G.Hoover, Phys. Rev. B28, 1756 (1983)

84. D.L.Evans, J. Chem. Phys. 78, 3297 (1983)
85. D.J.Evans, W.G.Hoover, B.H.Failor, B.Moran, and A.J.C.Ladd, Phys. Rev. A28, 1016 (1983)
86. D.J.Evans and G.P.Morriss, Chem. Phys. 77, 63 (1983); Phys. Lett. A98, 433 (1983)
87. L.Verlet, Phys. Rev. 159, 98 (1967)
88. C.W.Gear, ANL Report #7126, Argonne National Laboratory (1966); and in 'Numerical initial value problems in ordinary differential equations' (Pretice Hall, Englewood Cliffs, N.J. 1971).
89. A.Rahman and F.H.Stillinger, J. Chem. Phys. 55, 3336(1971).
90. D.Castiel, L.Dobrzynski and D.Spanjaard, Surf. Sci. 59, 252(1976).
91. Handbook of Chemistry and Physics, 56 Edition, P. E-230; M.Lowrie and M.Gonas, J. Applied Phys. 38, 11(1967).
92. This point has been checked by A.Franchini, unpublished.
93. see, for example, Per Bak, Rep. Prog. Phys. 45, 587(1982).
94. H.J.Schulz, Phys. Rev. B22, 5274(1980); Phys. Rev. B28, 2746(1983).
95. A.Saxena, E.T.Gawlinski and J.D.Gunton, Surf. Sci. 160, 618(1985).
96. J.M.Kosterlitz and D.J.Thouless, J. Phys C6 1181(1973).
97. A.Fasolino and E.Tosatti, to be appear on Surf. Sci.
98. J.F.Scott, Rev. Modern Phys. 46, 83(1974).
99. W.Cochran, Phys. Rev. Lett. 3, 412(1959); Adv. Phys. 19, 387(1960); 20,401(1961).
100. P.W.Anderson, Fizika dielektrikov, Ed. G.I.Skanavi, Acad. Nauk. SSSR, Moscow(1960) P. 290.
101. A.D.Bruce, in 'Soliton and Condensed Matter Physics' Eds. A.R.Bishop, T.Schneider (Springer, Berlin 1979)
102. V.Heine, J.D.C.McConnell, Phys. Rev. Lett. 46 1092(1981). J. Phys C17, 1199(1984).
103. V.Heine in 'Statics and dynamics of non-linear system' eds. H.Bitz, G.Benedek, R.Zeyher (Springer Berlin 1984)
104. American Institute of Physics, Handbook (third edition) McCRAW-HILL (1982) 4-127
105. Landolt-Bornstein in 'Numerical Data and Function Relationships in Science and Technology' eds. K.-H.Hellwege, (Springer-Verlag Berlin, 1981) V.13